

# Spin injection in MnGa/ GaN heterostructures

Dissertation  
zur Erlangung des  
mathematisch-naturwissenschaftlichen Doktorgrades

"Doctor rerum naturalium"

der Georg-August-Universität Göttingen

im Promotionsprogramm ProPhys  
der Georg-August University School of Science  
(GAUSS)

vorgelegt von  
Christian Zube  
aus Kassel

Göttingen, 2015

Betreuungsausschuss:

Prof. Dr. Angela Rizzi, IV. Physikalisches Institut, Georg-August Universität Göttingen

Dr. Jörg Malindretos, IV. Physikalisches Institut, Georg-August Universität Göttingen

Prof. Dr. Markus Münzenberg, Institut für Physik, Ernst-Moritz-Arndt Universität Greifswald

Mitglieder der Prüfungskommission:

Referent:

Prof. Dr. Angela Rizzi, IV. Physikalisches Institut, Georg-August Universität Göttingen

Korreferent:

Prof. Dr. Markus Münzenberg, Institut für Physik, Ernst-Moritz-Arndt Universität Greifswald

Weitere Mitglieder der Prüfungskommission:

Prof. Dr. Konrad Samwer, I. Physikalisches Institut, Georg-August Universität Göttingen

Prof. Dr. Peter Blöchl, Institut für Materialphysik, Georg-August Universität Göttingen

Prof. Dr. Hans Hofsäss, II. Physikalisches Institut, Georg-August Universität Göttingen

Prof. Dr. Hans-Ulrich Krebs, Institut für Materialphysik, Georg-August Universität Göttingen

Tag der mündlichen Prüfung:

# Preface

## Following Moore's Law

A state of the art CPU has over two billion transistors on one chip. To keep track with Moore's law, which states that the amount of transistors doubles every second year, the size of one transistor has to be reduced down to 5-7 nm in 2016-2017.

Shrinking the size of a transistor to sub 10 nm structures probes fundamental concepts of physics. First of all, quantum mechanical tunneling occurs, which can lead to device failure because adjacent transistors 'crosstalk' with each other. Secondly, due to this crosstalk, the transistors become 'leaky' which means that most of the current is converted into heat and not into logic operation. This power dissipation will sooner or later challenge Moore's Law of miniaturization.

Switching in a typical device is done by moving charges from one reservoir to another with the control of a gate. By taking advantage of the spin property of an electron, a new and dissipation-less information manipulation method, previously unimaginable, now seems possible. Semiconductor spintronic tries to include the spin property into a logic device for data processing; it could be the key for the next generation information technology.

The following thesis explores the feasibility of the MnGa/GaN material system in terms of its possible use for semiconductor spintronic applications.





# Table of Contents

<b>Introduction &amp; outline</b>	<b>1</b>
<b>1 Molecular beam epitaxy of GaN and MnGa</b>	<b>5</b>
1.1 Substrate choice . . . . .	5
1.2 The GenII apparatus . . . . .	10
1.2.1 Sample loading and cleaning . . . . .	10
1.2.2 Growth chamber . . . . .	11
1.2.3 Growth monitoring with RHEED . . . . .	13
1.3 GaN growth . . . . .	14
1.3.1 Surface kinetics . . . . .	14
1.3.2 Growth process . . . . .	15
1.3.3 Temperature control . . . . .	16
1.4 MnGa growth . . . . .	19
<b>2 Spintronics</b>	<b>21</b>
2.1 Physical background . . . . .	23
2.2 Experimental detection of spin injection . . . . .	27
2.2.1 Electrical detection with a 3-terminal and 4-terminal setup . . . . .	27
2.2.2 Optical detection with a LED structure . . . . .	29
2.3 State of the art . . . . .	32
2.4 MnGa as a possible spin injector for GaN . . . . .	34
<b>3 MnGa/ GaN heterostructures</b>	<b>37</b>
3.1 MnGa bulk properties . . . . .	37
3.1.1 Structure . . . . .	37
3.1.2 Magnetic properties . . . . .	41
3.2 MnGa/ GaN Interface . . . . .	42
3.2.1 RHEED . . . . .	42
3.2.2 Transmission electron microscopy (TEM) . . . . .	46

3.3	Electrical properties of the MnGa/ GaN interface . . . . .	52
3.3.1	Schottky's standard model . . . . .	52
3.3.2	Schottky diode in thermal equilibrium . . . . .	53
3.3.3	Forward and reverse biased Schottky diode . . . . .	54
3.3.4	Surface and interface states . . . . .	56
3.4	Transport processes through the MnGa/ GaN interface . . . . .	61
3.5	Barrier transport characteristics . . . . .	67
3.5.1	Sample preparation . . . . .	67
3.5.2	Analysis . . . . .	70
<b>4</b>	<b>Optical detection of spin injection</b>	<b>73</b>
4.1	Experimental setup . . . . .	73
4.2	GaAs reference sample . . . . .	78
4.3	MnGa/GaN LED structure and sample preparation . . . . .	86
4.4	Spin injection from MnGa into GaN . . . . .	90
4.4.1	Side view . . . . .	90
4.4.2	Top view . . . . .	91
4.5	Magnetoabsorption effects in MnGa . . . . .	95
<b>5</b>	<b>Electrical detection of spin injection</b>	<b>99</b>
5.1	Detection setup . . . . .	99
5.2	3-terminal measurements . . . . .	102
5.3	4-terminal measurements . . . . .	102
	<b>Discussion &amp; summary</b>	<b>107</b>
	<b>Appendix A Process parameters</b>	<b>113</b>
	<b>Appendix B Hints, tips &amp; tricks</b>	<b>117</b>
	<b>Acknowledgments</b>	<b>122</b>
	<b>Publications worth reading to get into the topic</b>	<b>123</b>
	<b>Bibliography</b>	<b>125</b>

# Introduction & outline

Spintronic devices based on the Giant Magnetio Resistance (GMR) and later on Tunnel Magneto Resistance (TMR) effect are well established since their discovery in 1988 and 1995, respectively [1] [2] [3].

The time-line of semiconductor spintronics starts in 1990 with a proposal of a new class of semiconductor devices: the Spin FET (*Datta-Das transistor*)[4]. In this FET, the electric field applied to the gate changes the spin orientation of injected spin polarized electrons inside the channel (typically a two-dimensional electron gas) through Spin-Orbit interaction. Depending on the exact alignment of spins relative to the magnetization of the ferromagnetic drain electrode, the resistance is high (antiparallel) or low (parallel). Experiments in the mid 1990s showed a very long spin coherence time in semiconductor structures in comparison to metals [5]. Later on, Awschalom *et al.* successfully demonstrated the electrical injection of a spin polarized current into a III-V semiconductor (GaAs based spin LED) [6].

Awschalom *et al.* doped the host semiconductor (GaAs) with a magnetic impurity (Mn) to create a dilute ferromagnetic semiconductor GaAs:Mn (*Diluted Magnetic Semiconductor* (DMS)). The Curie temperature of (Ga,Mn)As is of the order of 170 K (depending on the Mn doping), which makes the material unusable for room temperature operation.

For the wide band gap semiconductor GaN a long spin life time of 20 ns at 5 K for a doping level of  $1 \cdot 10^{17} \text{cm}^{-3}$  has been measured [7]. This makes GaN an ideal candidate for spintronic applications.

In the following years, the idea of a GaN based DMS has been pursued as well. According to a theoretical work by Dietl *et al.* for a variety of magnetic impurities GaN should exhibit intrinsic ferromagnetic ordering [8]. Experimentally, Mn doped GaN layers showed ferromagnetism due to other magnetic phases inside the host matrix [9]. In other cases the origin of magnetism is not answered completely e.g. in Gd doped GaN [10]. The one and only GaN based DMS that shows a ferromagnetic ordering is GaN doped with Cr [11] [12]. There is a successful spin-injection based on GaN:Cr in a LED

structure at temperatures up to 200 K [13].

Due to the mentioned complications of DMS, in this thesis another approach will be pursued. A ferromagnet provides the spin polarization. Spin polarized electrons are injected into the non-magnetic semiconductor by applying a bias at the ferromagnet/semiconductor structure. This setup works well for almost all relevant semiconductors including Si, GaAs and GaN [14] [15] [16].

Due to the perfect epitaxial match of ferromagnetic MnGa on GaN and spin transport properties of GaN (long spin life time), the hybride MnGa/ GaN is a promising material for future spintronic devices to examine.

The samples are grown by Molecular Beam Epitaxy (MBE) on GaN templates or on a pre-grown LED structure. The growth process has been monitored in-situ with reflexion high energy electron diffraction (RHEED) to investigate the epitaxial match between ferromagnet and semiconductor. The deduced epitaxial relation has been verified by transmission electron microscopy (TEM). Furthermore, structural and magnetic properties of MnGa/ GaN hybrides has been assessed by x-ray diffraction (XRD), superconducting quantum interference device (SQUID) and vibrating sample magnetometry (VSM).

For the determination of the governing transport process across the MnGa/ GaN interface, transmission line features have been structured in a clean-room environment. The characterization has been done in a continuous flow cryostat with DC and AC measurement techniques. The best conditions for efficient spin injection have been found.

Two different spin detection mechanisms have been employed. An all electrical approach which includes the preparation of sub  $\mu\text{m}$  structures with electron beam lithography, and an optical setup based on the analysis of the emitted light of a LED with MnGa electrodes.

## Outline

After this small introduction, in the first chapter an overview of the MBE of GaN and MnGa will be presented. The physical background of spintronics as well as the description of the spin detection methods used in this work are discussed in chapter two.

The growth and characterization of MnGa on GaN is the main part of the third chapter. After the presentation of the bulk MnGa properties, the interface between ferromagnet and semiconductor is analyzed in more detail. This includes both, the structural and electrical aspects of the grown MnGa/ GaN heterostructures. The emphasis is put on the MnGa lattice arrangement on GaN(0001) and the Schottky barrier which is formed at the interface between metal and semiconductor.

Chapter four and five present the results of the spin injection experiments. In chapter four, a spin-LED will be analyzed whereas an all electrical approach towards spin detection will be pursued in chapter five.

The thesis closes with a discussion of the experimental results in terms of a possible use of MnGa/ GaN based spintronic devices.

According to the obtained data, MnGa grown under conditions used in this thesis is not an effective spin injector in GaN based devices. Only a low spin injection efficiency of 0.4% at 80K in remanence could be measured with a spin-LED despite the good epitaxial match between MnGa and GaN deduced by RHEED and TEM. No spin injection signal could be measured electrically. One possible source of error has been identified as well. The EELS analysis showed a possible Mn in-diffusion in the GaN layers which might depolarize the injected electrons.



# Chapter 1

## Molecular beam epitaxy of GaN and MnGa

Except for the pre-grown LED structure for the spin-LED, the layers in this thesis were grown in a molecular beam epitaxy (MBE) machine from *Veeco* (GENII). Therefore, the next section is dedicated to the MBE growth of GaN and  $\text{Mn}_x\text{Ga}_{1-x}$  with the GENII machine including a short overview of available GaN templates.

MBE benefits in applications where the precise control of the layer thickness is needed. One drawback of this technique is the low growth rate and the need for ultra high vacuum for a low contamination level in the layers. This makes the large scale production quite expensive and time-consuming. Within the compound semiconductor industry, other growth techniques like *metal organic chemical vapor deposition* (MOCVD) or *hydride vapor phase epitaxy* (HVPE) are used. They allow for higher growth rates and, in contrast to MBE, there is no need for ultra high vacuum, which speeds up the complete growth run.

Material properties of the group III nitride system can be found e.g. in the *Handbook of Nitride Semiconductors and Devices*, by Morkoç [17]. They will not be presented here.

### 1.1 Substrate choice

The samples produced in this thesis are typically grown *homoepitaxial* on GaN(0001) templates. A template consists of a thin GaN layer (approx. 3-10  $\mu\text{m}$  thick) which is grown on a substrate. The most frequently used

substrate is sapphire ( $\text{Al}_2\text{O}_3$ ) and secondly siliconcarbide (SiC). The smaller lattice mismatch of SiC (3.3%) in comparison to  $\text{Al}_2\text{O}_3$  (13%) makes SiC the right choice when crystal quality, especially a low defect density, is important. Despite the last advances in SiC template technology, the lowest achieved dislocation density on foreign substrates is still of the order of  $10^7 \text{ cm}^{-2}$ .

Usually, sapphire is used throughout the nitride industry. It is cheap, easy to handle (cleaning, pre-growth treatment) and it is available in large sizes up to eight inch diameter. In the last couple of years, GaN templates grown on Si (GaN-on-Si) and pure bulk GaN templates reached the market. Both follow two different approaches. GaN-on-Si addresses the low cost market. It is cheap in comparison to sapphire and there are 300 mm wafers available. The drawback is the crystal quality. Due to the large mismatch in lattice constant (17%) and thermal expansion coefficients with respect to GaN, the first wafers were not usable for applications. They cracked upon cooling and the dislocation density exceeded  $10^{10} \text{ cm}^{-2}$ . The insertion of a AlN buffer layer improved the quality significantly, but the GaN layers were still under tensile stress [18]. An up-to-date GaN-on-Si wafer is grown with up to 20 AlN/ GaN superlattices. At the typical growth temperature of MOCVD GaN ( $T_s=1000-1100^\circ\text{C}$ ), the superlattice growth introduces compressive strain which counteracts the tensile strain of the two different materials [19]. This effectively suppresses cracking of the layers upon cooling. Furthermore, the dislocation density can be reduced down to values for typical GaN/ sapphire substrates. The best solution for GaN growth would be a bulk or even native substrate. There are two 'bulk' substrates types available, *freestanding* and truly *bulk* GaN. A freestanding GaN template is a thick GaN layer (can be  $100\mu\text{m}$  thick) grown e.g. on SiC or sapphire usually by HVPE which allows high grows rates. After the process of growing is completed, the substrate is being removed, usually by a laser lift-off process. The *freestanding* GaN can then be used as a homoepitaxial substrate and this process can be repeated until the desired thickness and quality is achieved. Typical dislocation densities of this method are  $10^6-10^7 \text{ cm}^{-2}$ . A good overview of this technique can be found in the review of Miskys et al. [20].

But *freestanding* substrates are not *bulk* GaN. Why is it so complicated to grow GaN out of a melt as in the case of Si or GaAs?

There are a couple of physical restrictions. The biggest problem is the large vapor pressure of nitrogen together with the low solubility of N in the molten Ga metal. In the 1980s, polish researchers from the High Pressure Research Center *Unipress* in Warsaw successfully synthesized bulk GaN at temperatures up to  $1700^\circ\text{C}$  and pressures of 20 kbar. These high pressures are needed to dissolve the nitrogen in the liquid Ga [21]. At the moment, it is possible



to buy two inch bulk GaN wafers from a spin off company (*Ammono* GaN).

From the growers point of view, two things are important for epitaxy. First of all, the surface morphology and roughness, and secondly, the overall structural quality of the GaN template layer.

The surface roughness can easily be measured with Atomic Force Microscopy (AFM) on a cleaned sample. Figure 1.1 shows typical AFM scans of the templates I used during my time. It includes GaN/  $\text{Al}_2\text{O}_3$  grown by MOCVD (*Lumilog*), GaN-on-Si (MOCVD, *Azzurro*) and bulk GaN (*Ammono*). The orientation is in all cases the Ga polar c-plane (0001). The smallest rough-

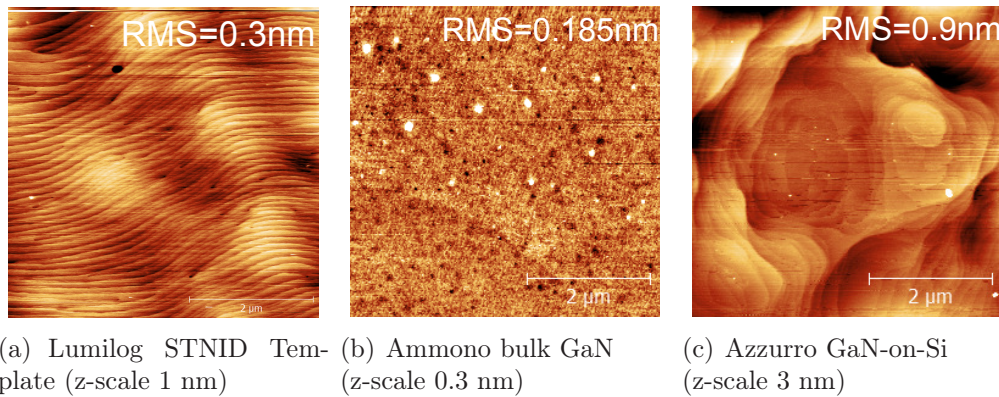


Figure 1.1: AFM scans of typical GaN templates. Scansize is  $5 \times 5 \mu\text{m}^2$  in all cases.

ness with an RMS value of 0.19 nm (scan area  $25 \mu\text{m}^2$ ) has the bulk GaN, Subfigure 1.1(b), as expected. There are no visible atomic steps. By taking a closer look, scratches from the polishing step and small dirt particles can be seen. The MOCVD grown template on  $\text{Al}_2\text{O}_3$ , Subfigure 1.1(a), shows typical monolayer steps with a step height of 0.259 nm ( $\cong 1$  monolayer = lattice constant/2). The dark spots are dislocations. They stem from the GaN/ $\text{Al}_2\text{O}_3$  interface and are typical for the growth on foreign substrates. Azzurro GaN-on-Si template shows the worst surface in this comparison, Subfigure 1.1(c). The surface shows no atomic steps and the RMS value amounts to 0.9 nm. It is worth mentioning that the wafers provided by Azzurro were *Raider* grade which means that they are just for testing the process with these wafers and are not meant for growing. They are delivered without meeting the specifications concerning quality. In their specification sheet they claim to have the same dislocation densities as GaN grown on sapphire. Usually, they do not grow on two inch substrates. Typical sizes which are available are 150 mm

and 300 mm wafers which shows the easy scalability of the GaN-on-Si process.

The second important key parameter, crystal quality, can be easily quantified by X-ray diffraction experiments, especially by *rocking curves/Omega scans*. In this measurement geometry, the position of the source and the detector is fixed, and the sample surface is tilted (see Figure 1.2). With this geometry, one can measure the grain size, mosaic spread of a layer and the dislocation density [22] [23]. In the experiment a diffraction plane, e.g. a *symmetrical* (002) or *asymmetrical*(104) plane is chosen. The corresponding angle  $2\theta$ , which is the angle between detector and incident beam, is set according to the bragg condition  $2d_{hkl} \sin(\theta) = n\lambda$ , where  $d_{hkl}$  is the lattice spacing and  $\lambda$  is the wavelength used. In this case the Cu- $k_\alpha$ -line with  $\lambda=1.54 \text{ \AA}$ . The maximum intensity is at  $\omega = 2\theta/2$ . A small rocking curve indicates a large crystalite size, whereas a broad rocking curve is a sign for mosaic type layers or structures (e.g. the rocking curves of nanowires have a broad rocking curve despite a rather sharp peak in the typical  $\theta - 2\theta$  scan).

In both orientations, (002) and (104), the *bulk* GaN has the smallest rocking curve, which shows the good quality of the wafer. The Azzuro template shows comparable widths to the sapphire template in the (002) direction, but in the asymmetrical scan direction the difference is far more pronounced. As mentioned by Heying *et al.*, the asymmetric scan direction is a more reliable indicator for the structural quality than the (002) reflex [23]. The threading dislocations lie parallel to the [001] direction of GaN and are not visible in a (002) scan.

A point which has not been discussed yet is the price. A two inch wafer of bulk GaN wafer costs approximately €1500, whereas the GaN-on-Si costs €50 (scaled down from a 150 mm wafer). The price of the 2" test wafer was €150. With €350 the GaN/Al<sub>2</sub>O<sub>3</sub> templates seem to be a good compromise between quality on the one hand, and price on the other. Unfortunately, no data is available for larger sizes, e.g. 4" or 6". Out of a 2" wafer one can cut twelve 10x10 mm pieces. The rest of the wafer cannot be used for growing because the pieces are too small. A change to a large wafer size and thus more usable pieces is therefore the next step.

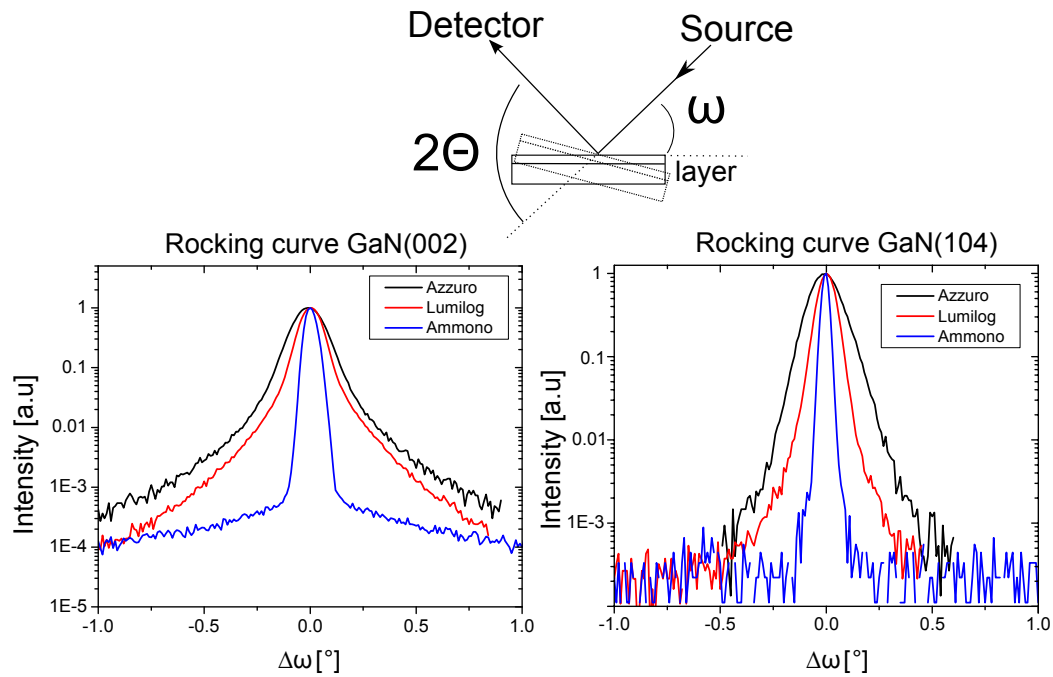


Figure 1.2: Overview of the XRD rocking curve measurement including data of three different GaN templates. The sketch shows the setup. The sample is tilted and the angle  $2\theta$ , which corresponds to the lattice spacing, is kept fixed. The bottom figures show the measured data of three different template types in symmetric(002) and asymmetric(104) plane orientations. The difference in crystal quality is better seen in asymmetric scan direction.

## 1.2 The GenII apparatus

The GenII is, according to the company Veeco, one of the most frequently sold MBE systems all over the world. Depending on the layout and configuration of the system, various compound semiconductors, e.g. InP, GaAs, ZnO, CdZn and of course (In,Al,Ga)N, can be grown. The system consists of three different chambers. These chambers are, in ascending vacuum quality (background base pressure  $P_x$ ), intro chamber ( $P_I=1 \cdot 10^{-8}$  mbar), buffer chamber ( $P_{Buffer}=1 \cdot 10^{-10}$  mbar) and the growth/reactor chamber ( $P_R < 5 \cdot 10^{-11}$  mbar).

### 1.2.1 Sample loading and cleaning

The substrates are loaded into the intro chamber after a wet chemical cleaning in a ultrasonic bath with first acetone, second methanol and third DI-water. At the beginning of my thesis, isopropyl alcohol (IPA) was used instead of

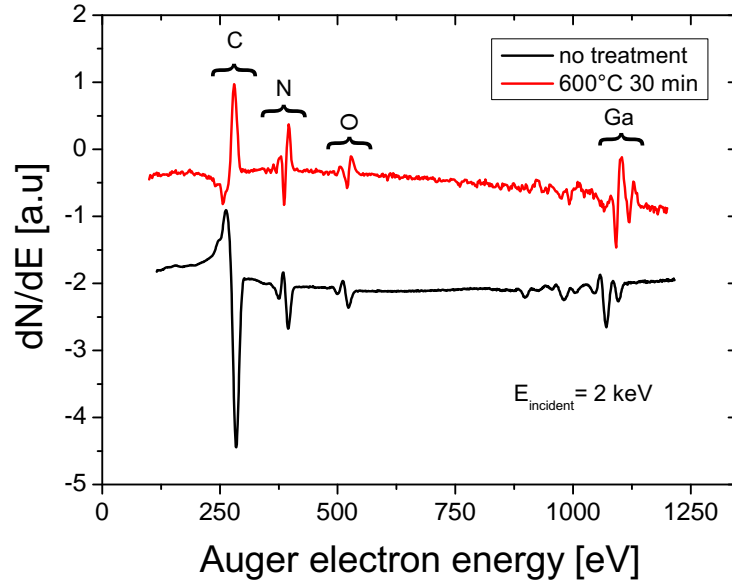


Figure 1.3: Auger spectra recorded in the other MBE machine (ELSA). Even after a bake out at 600°C, the oxygen peak is still visible, indicating that an oxide, probably  $\text{Ga}_2\text{O}_3$ , is present at the surface which cannot be removed that easily.

methanol. No difference between these two cleaning recipes has been noticed. The intro chamber is equipped with an oil-free scroll pump as a backing pump and a turbo pump as main pump. After loading the wafer into the intro chamber, the surface of the samples are not completely clean. Traces of residues of solvents, water and the native oxide of GaN can be seen in an Auger electron spectra (Figure 1.3) recorded in another MBE machine (ELSA) directly after loading without any further treatment.

In order to remove surface contaminations, a couple of cleaning steps are performed. First, the sample is heated to 200°C in the intro chamber to desorb the water. Secondly, the sample is transferred into the buffer chamber where a second heating step to 600°C should remove most of the (carbon based) solvents. A closer look at the Auger spectra, recorded after the 600°C heating step, shows that indeed the carbon peak reduced but the oxygen peak is still visible.

The pumping inside the buffer chamber is provided by an ion getter and titanium sublimation pump.

## 1.2.2 Growth chamber

After this procedure, the sample is ready for the growth chamber. Here, the last and, in my opinion, best cleaning step is performed. At growth temperature, roughly  $T_{\text{Growth}} = 650^\circ\text{C}$ , the sample is exposed to an activated nitrogen plasma for 15 minutes. With the help of Reflexion High Energy Electron Diffraction (RHEED, subsection 1.2.3) one can observe a change in the reflexion spot appearance. The nitrogen plasma effectively removes the surface oxide [24].

Inside the growth chamber, the sources are set up on a ring pointing towards the substrate. Solid and liquid materials are supplied by effusion cells, e.g. gallium, indium, aluminum, manganese and silicon. Nitrogen is introduced by a gas valve in a radio frequency plasma source. Inside the nitrogen source, the radio frequency generates a plasma. Not all nitrogen atoms are ionized. The optical emission of the plasma is recorded with a spectrometer connected to the plasma source (*Nitroscan*, very useful). It shows emission from ionized nitrogen atoms ( $\text{N}^*$ ) and molecular nitrogen. Both species are directed through an aperture plate towards the sample region. After approx. 500-750 growth runs, this aperture plate should be replaced in order to maintain plasma stability especially at high powers and fluxes.

On the back of the sample holder arm an ion gauge is mounted. It can be used to calibrate the effusion cells. The sample holder arm has to be

turned around by  $180^\circ$  until the ion gauge points towards the effusion cells. When the cells are hot they evaporate material according to the Knudsen cell equation. These atoms are ionized by the electrons emitted from the hot filament of the gauge. The ionized atoms are accelerated towards the central ion collector and an ion current can be measured. The pressure reading is called *beam equivalent pressure*  $P_{\text{BEP}}$ . Its value can be used to calibrate the cell in subsequent growth runs. The pressure depends on the type of atoms, usually the gauge is calibrated for  $\text{N}_2$  gas. A  $P_{\text{BEP}}$  of e.g.  $5 \cdot 10^{-7}$  mbar has a different physical flux (Atoms/cm<sup>2</sup>/s) for Ga atoms than e.g. In atoms due to different ionization energies.

During stand-by operation, a helium cryo pump and an ion getter pump are maintaining a vacuum of roughly  $5 \cdot 10^{-11}$  mbar. During growth the valve to the ion getter pump is closed because the incoming nitrogen increases the pressure up to  $1 \cdot 10^{-5}$  mbar which is too much for the ion getter pump. The complete growth chamber is surrounded by a shield that can be filled with liquid nitrogen during growth to reduce the background pressure by half an order of magnitude (cryo pump). During the last years, the titanium sublimation pump inside the growth chamber was not installed due to a vacuum leak.

The effusion cells are arranged in a circle on a large flange. They point towards the sample holder under an angle of approx.  $60^\circ$ . In growth position, the sample holder points horizontally towards the middle of this flange. The drawback of this design is that it is not possible to use the top four ports with materials which are liquid at evaporation temperatures (gallium, aluminum and indium). Therefore, the two most upper ports are for gases, nitrogen and hydrogen, and the two others are used for silicon and manganese. Silicon can be fused to the crucible with a special technique and can be mounted up-side down.

Unfortunately, this procedure does not work with manganese, which is a brittle material and forms flakes. Two different methods have been tried. First, a PBN aperture plate which fits seamlessly to the crucible top and secondly, a molybdenum mesh around the top of the crucible, Figure 1.4.

In both cases, the metal flux is very low. All the manganese flakes are located at the top of the crucible, where the heat of the cell filaments is drastically reduced. Around the opening of the crucible, a lot of manganese can be seen on the cryo shield. This means the manganese beam is not well directed which is obvious because the material is not at the very bottom of the crucible.

Furthermore, due to the small hole opening of the PBN part, the flux is reduced again by a factor of five. Therefore, the growth rate is very low,



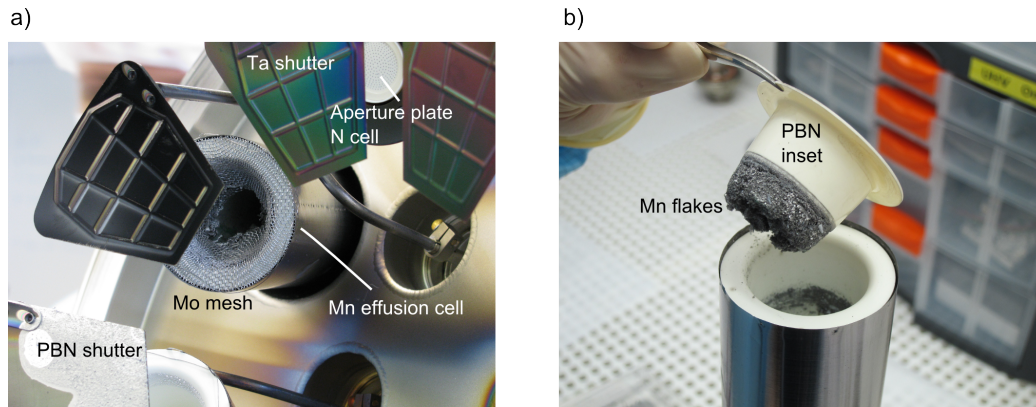


Figure 1.4: View of the manganese cell. a) Shows an overview of the flange including nitrogen plasma source (top), manganese cell (middle) and Ga cell (bottom left). For the Ga cell a PBN shutter has to be used because Ga attacks tantalum. b) Removal of the PBN inset of the Mn cell.

smaller than 0.5 nm/ min for  $\text{Mn}_{50}\text{Ga}_{50}$  at a Mn cell temperature of  $1050^\circ\text{C}$ . The background pressure increased simultaneously to the same order of magnitude as the beam flux itself. A mass spectrometer analysis revealed out-gassing nitrogen as the source for the increased pressure.

In terms of metal flux, the molybdenum mesh works better, but the background pressure is still very high. With the mesh another problem occurred. The manganese corroded the molybdenum mesh. In Figure 1.4 a) one can clearly see a hole in the middle of the mesh after approximately three years of usage. Therefore, long-term stability cannot be guaranteed. Furthermore, a contamination with molybdenum is possible.

A change to one of the ports pointing upwards would be beneficial, especially in terms of metal flux, but a contamination of another port with manganese has to be avoided on the other side. Another option would be a thorough clean of the complete port, including the cryo shield around the cell.

### 1.2.3 Growth monitoring with RHEED

The MBE machine is equipped with a couple of useful tools, which makes life much easier. The most used growth analysis tool during the thesis was RHEED (Reflexion High Energy Electron Diffraction). Here, a high energetic electron beam, 14.5 keV, is focused on the sample under a very small angle, approx.  $1\text{-}3^\circ$ . The electron beam is diffracted at the very surface of the layer and detected on a phosphor screen. Due to the small angle, the penetration

depth is only a couple of monolayers. The advantage in contrast to other diffraction experiments, e.g. LEED (Low Energy Electron Diffraction), lies in the possibility to use this technique during growth. It can be used to monitor the growth process itself, e.g. 2D vs. 3D growth and growth rate calculation and furthermore, one gains insight into the exact arrangement of the grown layer (and adatoms) with respect to the layers beneath. Especially the last point is important when the growth of ferromagnetic MnGa on GaN is discussed in chapter 3.

## 1.3 GaN growth

This section offers insight into the MBE growth of GaN(0001) with the GenII machine. Most of the concepts discussed here can be found in detail in the mentioned literature. The focus lies on the experimental realization with *our* GenII machine.

### 1.3.1 Surface kinetics

In general, on the crystal surface the following processes happen:

- Adsorption
- Desorption
- Surface diffusion
- Incorporation into the lattice
- Decomposition

All these processes have to be balanced in order to get a smooth 2D layer. Sometimes they compete, e.g. decomposition and incorporation or adsorption and desorption. Generally, a long diffusion length of the adatoms, Ga and N, is needed in order to find the site with the lowest energy for incorporation, usually a step, vacancy (missing atom) or a dangling bond.

Zywietz *et al.* studied the diffusion length of Ga and N adatoms on the Ga-polar (0001) and N-polar (000 $\bar{1}$ ) surface with density functional theory [25]. They calculated a high mobility for Ga, whereas the diffusivity of N was two orders of magnitudes lower for both surfaces. According to the authors, a high coverage of N on the surface further increases the diffusion barrier for



Ga, thus, reducing the diffusion length for Ga.

This means, a Ga rich surface is assumed to lead to a smooth surface with a 2D growth mode. Based on this work, Nothrup *et al.* showed that a liquid Ga film is stabilized on the GaN(0001) surface up to two mono layer thickness, Figure 1.5 [26]. This 'bi-layer' can be seen in RHEED experiments and can be used in the determination of the surface coverage with Ga.

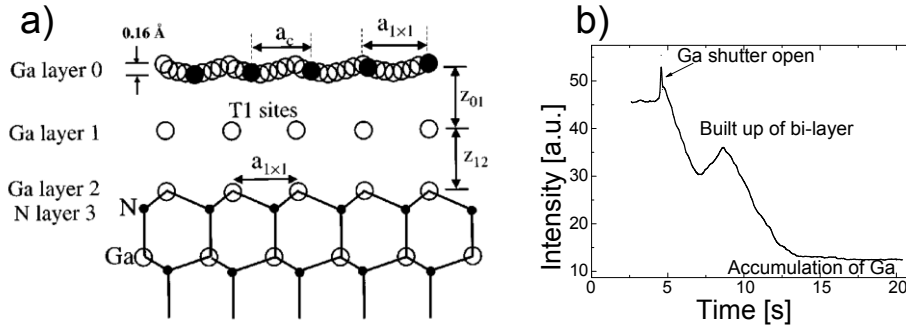


Figure 1.5: a) Side view of the laterally contracted bi-layer model by Northrup *et al.*. The first layer, layer 0, is laterally contracted with respect to the underlying Gallium adlayer, layer 1. In RHEED experiments, this bi-layer can be seen when it builds up, Figure b). Reprinted Figure a) with permission from [26]. Copyright (2000) by the American Physical Society.

### 1.3.2 Growth process

The GaN layers in this thesis are grown according the modulated growth method. Details can be found in the thesis of the former group member Daniel Broxtermann and the published paper which gives an overview of the optimization process concerning AlGaIn/ GaN heterostructures [27] [28].

In this technique, GaN is grown at the crossover from bi-layer to Ga droplet formation. The gallium flux is approx. 1.4 times higher than the stoichiometric flux. The excess gallium has to be desorbed from time to time to avoid metal accumulation on the surface. This is done by stopping the growth (closing both Ga and N shutter) after a couple of growth minutes and wait until the accumulated metal desorbs (approx. 30s). The desorption process can be recorded with RHEED.

In more detail, first, for 20s the Gallium shutter is opened to form the Ga bi-layer. Secondly, the N shutter is opened and the growth process begins. The intensity continues to fall due to the accumulation of metal on top of the GaN surface which scatters the electrons diffusely. After a certain amount

of time (5- 7.5 min) the growth is interrupted and the excess Ga is desorbed. Here it is important that not all Ga is removed from the surface. The bi-layer should still be on top. After the desorption time of 30s the intensity should begin to start rising. An increase in intensity indicates the last couple of liquid Ga layers are beginning to evaporate. This is the point when the Ga and N shutters are opened again to continue the growth. If the intensity is not rising after the desorption time, too much Ga is on top. A reduction in metal flux or an increase in substrate temperature usually help. Finally, at the end of the growth the complete bi-layer desorption can be observed. The Si doped GaN is grown with the same method just the Si shutter is opened, too. No (Al,Ga,In)N heterostructures have been grown within the scope of this thesis, see again D. Broxtermann's thesis for details on the growth of heterostructures.

### 1.3.3 Temperature control

According to my experience, adjusting the substrate temperature to the best value is the most difficult task. Determination of the exact surface temperature is difficult. GaN is transparent for infrared pyrometers except GaN is grown on silicon or other infrared absorbing material. That means if one uses a pyrometer with a typical GaN on sapphire template, the temperature of the heater behind the sample is measured.

The MBE machine is equipped with a thermocouple, which is located in the middle of the heater in a small hole. It collects all the heat from the back of the sample holder. Therefore, the thermocouple has a large offset with respect to the actual surface temperature, in the range of 100-150°C depending on the sample holder and exact mounting of the sample. It can only give a rough estimation of the exact substrate temperature. This is nothing to worry about since the sample holder and substrate is usually the same in subsequent growth runs, therefore, the offset should not change dramatically from sample to sample. It is worth keeping in mind that all heat sources can change the surface temperature. I measured an additional temperature increase when the Si cell was hot (1150°C) and the shutter is open.

Another interesting possibility of an indirect temperature measurement has recently been tested in the MBE system. It is called band edge absorption. Here, the change of band gap energy is measured in an absorption experiment with a bright UV light source [29]. The band gap energy itself is dependent on the temperature. This method is still under construction and is, in my opinion, at the moment not usable.

To the best of my knowledge the most preferable methods for temperature measurements are the following:

- **Evaporation of 500 nm of titanium on the back of the sample** and the use of a pyrometer which can be adjusted to the emissivity of Ti (or one uses the value for Si if only reproducibility for every run is needed).
- Monitoring of the desorption time of the Ga bi-layer with **RHEED**.

The first method is quite straightforward. A thick titanium layer is evaporated on the back of the sample. The titanium absorbs the infrared light from the heater completely. With the pyrometer a measurement of the titanium temperature is then possible. The titanium is approx. 330  $\mu\text{m}$  (sapphire thickness) from the MOCVD grown GaN away. On this short distance the temperature difference can be neglected. Even if the exact temperature of GaN is not known, the reproducibility increases dramatically. This technique was used e.g. during the growth of high quality InGaN/ GaN two dimensional electron gases in the group. InGaN alloys are very sensitive to the substrate temperature, therefore, a reproducible temperature is needed.

The second method is only applicable when a clean GaN(0001) surface is accessible with RHEED. The desorption time of the bi-layer depends only on the substrate temperature and the used nitrogen conditions. Under typical growth conditions, nitrogen plasma on, a gallium bi-layer is deposited on the surface and with RHEED the intensity of the direct reflected beam is monitored. After deposition of the bi-layer, the gallium shutter is closed and the desorption process is recorded. The time for the desorption of one ML of liquid gallium can serve as an indicator for the substrate temperature. A calibration curve measured on a GaN-on-Silicon template with a pyrometer as a temperature control is shown in Figure 1.6.

In the last couple of years a new growth technique for GaN layers came up especially for AlGaN/ GaN heterostructures. The growth is done under fluxes ranging from  $0.75 < \text{Ga}/\text{N} < 1.1$  and at temperatures above the decomposition temperature of GaN ( $T > 750^\circ\text{C}$ ). Koblmüller *et al.* found that samples grown under such conditions had slightly lower Ga vacancy concentrations  $V_{\text{Ga}}$ , lower unintentional oxygen incorporation, and improved electron mobilities [30] [31].

This growth technique has not been used in this thesis.

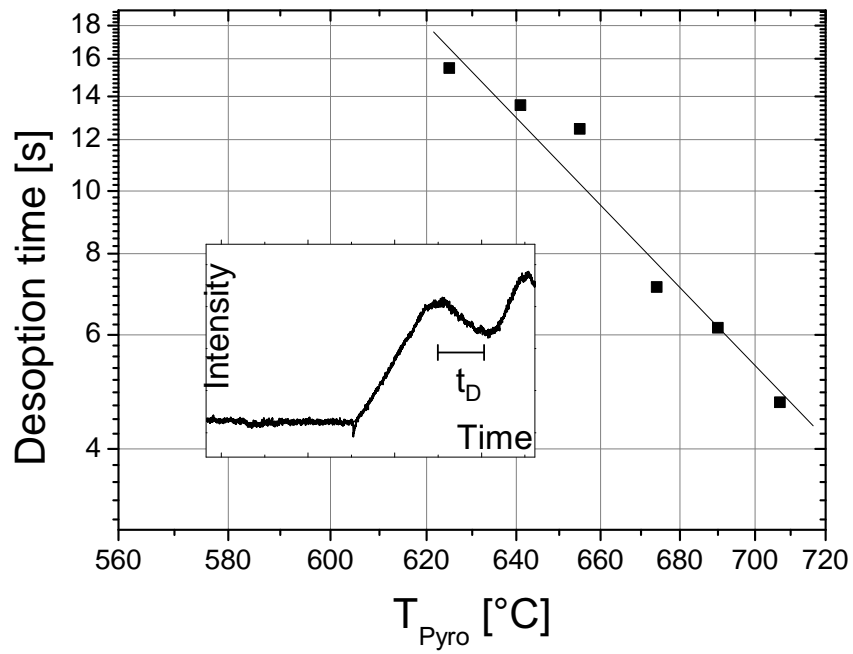


Figure 1.6: Change of the Desorption time with the substrate temperature measured with RHEED on a GaN/ Si template using the pyrometer. The inset shows one typical desorption transient. Emissivity of the pyrometer:  $\epsilon=0.639$ . Plasma condition 300W, 0.5sccm.

## 1.4 MnGa growth

In order to get a crystalline  $\text{Mn}_x\text{Ga}_{1-x}$  layer, a clean and smooth GaN(0001) surface is needed. If no nitrogen plasma cleaning step or *fresh* GaN is grown on the template, no  $\text{Mn}_x\text{Ga}_{1-x}$  diffraction spots are visible in RHEED.

The growth of  $\text{Mn}_x\text{Ga}_{1-x}$  alloys on GaN(0001) depends on the Mn:Ga flux ratio and the substrate temperature. The applied growth temperature is rather low, typically 250-400°C. Usually,  $\text{Mn}_x\text{Ga}_{1-x}$  is grown directly after GaN, which means that the substrate has to cool down from 650°C. This takes a lot of time.

The growth process is simple, the Mn and Ga shutters are opened simultaneously. It is useful to monitor the process with RHEED at the very beginning to get the epitaxial relationship between GaN and  $\text{Mn}_x\text{Ga}_{1-x}$ . This issue will be discussed in more detail in chapter 3.

At the end of the growth, it is important to add an Al cap on top.  $\text{Mn}_x\text{Ga}_{1-x}$  oxidizes rapidly and for thin layers smaller than 20 nm it can happen that all  $\text{Mn}_x\text{Ga}_{1-x}$  is oxidized (in subsection 3.2.2 a TEM picture of a not capped  $\text{Mn}_x\text{Ga}_{1-x}$  layer is shown). To add an Al cap, the substrate temperature has to be lowered to < 50°C. This can be achieved by filling the liquid nitrogen shield and turning the sample holder away from the effusion cells (they have a stand-by temperature of 300°C). It takes a long time until the thermocouple is colder than 50°C. When the temperature is attained, the Al shutter is opened for 3 min with an Al flux of 0.5nm/ min (approx.  $T_{Al}=1050^\circ\text{C}$ ).



# Chapter 2

## Spintronics

The first spintronic application were magneto resistance devices in hard disks in the 1990s. For the discovery of the giant-magneto resistance (GMR), Peter Grünberg and Albert Fert received the Nobelprice in Physics in 2007 [1] [2]. Originally, the idea dates back to Julliere who discovered a smaller effect in Ferromagnet (FM)/Non magnetic/FM structures [32]. Later on, the tunnel magneto resistance (TMR) discovered by Miyazaki *et al.* opened the door to smaller devices and increased storage density [3]. All devices have in common that the resistance can be changed when the magnetization of one FM electrode is reversed (*spin valve*).

The time from the lab to the first devices was really short. The team of Stuart Parkin from the IBM research center saw the potential of GMR and TMR devices for storage applications in the beginning 1990s and in 1997 IBM had the mass market debut with a 16.8 gigabyte hard disk based on the GMR effect (IBM Deskstar 16GP *Titan*).

The semiconductor based spintronic does not have such a story of success. The field is rather new and a practical application is still missing. Maybe the most cited work in this context is the *Datta-Das* transistor [4].

In this type of transistor, the source and drain are ferromagnetic contacts. A spin polarized current is injected at the source into a two-dimensional electron gas (2DEG) and the spin information is detected at the drain, Figure 2.1 a).

The spin orientation in the channel can be changed by an electric field, the gate voltage. The coupling between spins and the electric field is due to a spin orbit interaction, this effect is known as *Bychkov-Rashba* effect[33].

The advantage of a pure spin transistor lies in the heat dissipation-less operation. When transistors get smaller and smaller, power dissipation in terms

of leakage current plays a major role in device operation. In a pure spin FET, no current has to be sent through the device (at least in theory) which means that no ohmic resistance can cause heating. Another advantage of a spin FET is the additional degree of freedom. With the spin state of an electron a new information storage is available (no electrical current is needed for storage, similar to magnetic random access memories (MRAM)).

In 2009 Koo *et al.* demonstrated a working spin transistor at liquid helium temperatures based on NiFe ferromagnetic contacts and an InAs 2DEG [34]. In a *non-local* geometry, they were able to change the orientation of the injected spins with an applied gate voltage, Figure 2.1 b).

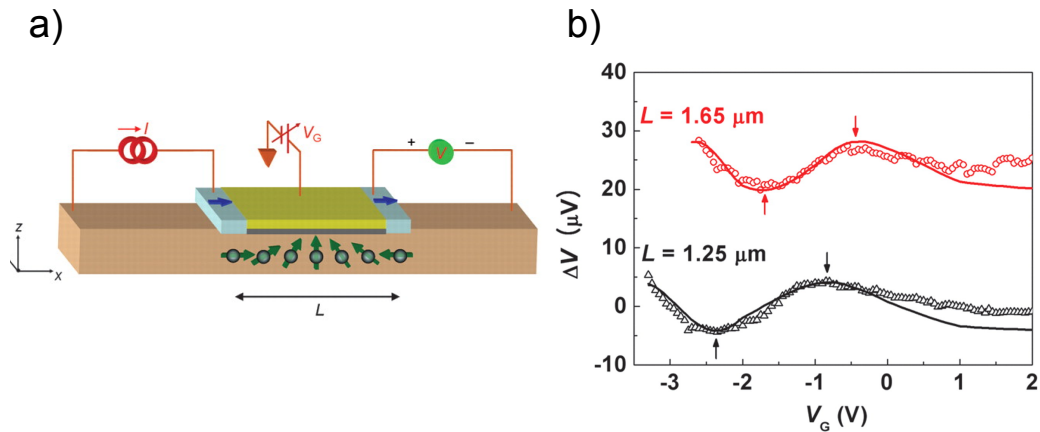


Figure 2.1: Experimental realization of a *Datta-Das* transistor in an InAs 2DEG. a) shows the setup used in the experiment. To separate the electrical current from the spin current, a *non-local* geometry is used. The detection circuit is sensitive to the orientation of the spins that arrive at the right FM electrode. In b) the measured voltage signal  $\Delta V$  is shown in dependence of the applied gate voltage. The solid line is a fit according to the theory of Datta and Das. From [34]. Reprinted with permission from AAAS.

To get familiar with the concept of semiconductor spintronics, the following chapter addresses the theoretical aspects of spin injection in semiconductors and it presents detection methods used in literature and in this thesis. Furthermore, a state of the art review of spin experiments related to GaN and MnGa is presented. At the end, the question why MnGa is a suitable ferromagnet for GaN based spintronic will be discussed.



## 2.1 Physical background

Spin injection is the creation of an imbalance of spin-up and spin-down electrons. It can be achieved both in metals and semiconductors. For semiconductors, the source of the spin polarization can be a spin polarized current from a ferromagnet into a semiconductor (FM/SC), an intrinsic magnetic semiconductor (DMS) or an optically generated spin population. The concept of spin injection dates back to the first experiments conducted by Julliere on Fe/Ge/Co sandwich structures in 1975 [32].

The polarization  $p$  of carriers is defined as:

$$p = \frac{n_{\uparrow} - n_{\downarrow}}{n_{\uparrow} + n_{\downarrow}} \quad (2.1)$$

$n_{\uparrow(\downarrow)}$  denote the number of spin-up (spin-down) electrons.

Spin injection in a non-magnetic material is a non equilibrium state. Therefore, no fermi level  $E_F$  can be defined for the system. To make this clear, in the following, the notation  $\mu_0$  will be used for the equilibrium chemical potential (which is defined as  $\mu_0 = \left(\frac{\partial U}{\partial n}\right)_{\text{neutral}}$  with  $U$  being the inner energy of the system).

The two chemical potentials of spin up,  $\mu_{\uparrow}$  and spin down  $\mu_{\downarrow}$  electrons have to be treated separately. In the Boltzmann approximation,  $n_{\uparrow(\downarrow)}$  is simply [35]:

$$n_{\uparrow(\downarrow)} = \frac{n_0}{2} \left[ \exp\left(\frac{\mu_{\uparrow(\downarrow)} - \mu_0}{k_B T}\right) - 1 \right] \quad (2.2)$$

with the boundary condition  $n_0 = n_{\uparrow} + n_{\downarrow}$ . The spin splitting for a non-degenerate, spin polarized, n-type semiconductor is shown in Figure 2.2. The spin resolved occupation spectrum for majority spin electrons is larger than for minority spin electrons due to a higher chemical potential.

Calculation of  $\mu_{\uparrow} - \mu_{\downarrow}$  gives after some algebra [35]:

$$\Delta\mu = \mu_{\uparrow} - \mu_{\downarrow} = k_B T \ln\left(\frac{1+p}{1-p}\right) \quad (2.3)$$

$\Delta\mu$  is a quantity which can be measured in an experiment. A non-magnetic voltage probe measures the average chemical potential, whereas a ferromagnetic voltage probe can sense  $\mu_{\uparrow} - \mu_{\downarrow}$ .

$$\mu_N = \frac{1}{2}(\mu_{\uparrow} + \mu_{\downarrow}) \quad \text{Non magnetic} \quad (2.4)$$

$$\mu_{\pm FM} = \mu_N \pm \frac{1}{2}(\mu_{\uparrow} - \mu_{\downarrow})\eta\alpha \quad \text{magnetic} \quad (2.5)$$

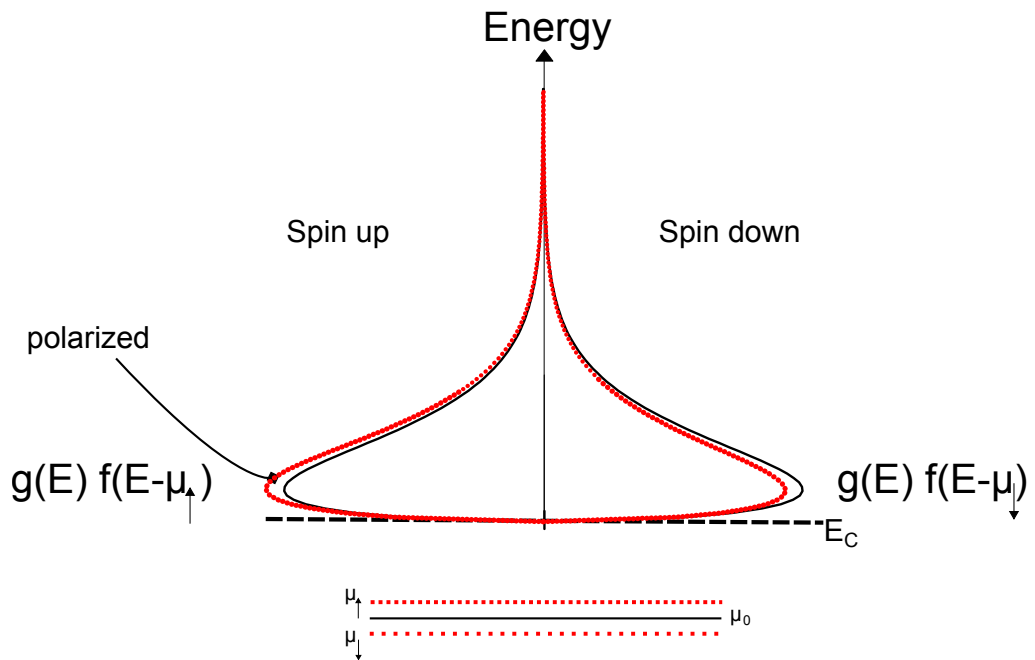


Figure 2.2: Spin resolved occupation spectrum for a non-degenerate, n-type semiconductor. The two chemical potentials for spin-up and spin-down electrons are different leading to a higher occupation for majority (spin-up) electrons. In black the unpolarized spectrum is shown.

$\eta$  is the spin polarization of the detecting ferromagnet. The value  $\alpha$  accounts for a possible spin filter effect of the interface. The  $\pm$  sign reflects the magnetization axis relative to an arbitrary reference system, usually an external magnetic field.

This expression can be understood by considering two extreme cases. First of all, if the spin accumulation is zero,  $\Delta\mu = \mu_{\uparrow} - \mu_{\downarrow} = 0$ , the ferromagnetic voltage probe is a normal paramagnetic probe  $\mu_N$ .

The second case is a half metallic ferromagnet with a perfect interface (only one spin channel at the fermi level, spin polarization  $\eta\alpha=1$ ). Depending on the magnetization of the ferromagnet, e.g. up ( $\uparrow$ ) and down ( $\downarrow$ ), the probe measures directly  $\mu_{\uparrow}$  and  $\mu_{\downarrow}$  of the semiconductor, respectively. If both channels are present inside the ferromagnet, the mean absolute difference between the chemical potentials is sensed. In the studied MnGa/ GaN samples, the spin accumulation is measured with ferromagnetic voltage probes that are not 100% spin polarized. The factors  $\eta$  and  $\alpha$  account for these non idealities.

The measured voltage  $V_{\text{Spin}}$  is then the difference of spin resolved chemical potentials between the two magnetization configurations (*spin-valve*):

$$eV_{\text{Spin}} = \mu_{\text{FM}(\uparrow)} - \mu_{\text{FM}(\downarrow)} = \pm\Delta\mu \eta \alpha \quad (2.6)$$

which is the formula derived by Crowell and Crooker in their contribution to the *Handbook of Spin Transport and Magnetism* by Tsymbal *et al.* [36, Chapter 23]. With this formula, the spin polarization can be calculated with Equation 2.3. In the case of one of the most studied FM/ SC systems, Fe/ GaAs, the values of  $\eta$  and  $\alpha$  are known. Soulen *et al.* measured  $\eta_{\text{Fe}}=0.42$  with a superconducting point contact (Andreev reflection) [37]. According to Adelman *et al.*, the spin injection efficiency of the Fe/ GaAs contact is  $\alpha(\text{Fe/ GaAs})=0.5$  [38].

Together with Equation 2.3 the theoretical spin signal  $V_{\text{Spin}}$  can be calculated for GaAs in dependence of the polarization of the SC. Taking a look at Figure 2.3, it can be seen that for typical polarization values ranging from 1-10% the spin related voltage is approx. 5-50 $\mu\text{V}$ .

## Conductivity mismatch

In 2000 Schmidt *et al.* modeled a FM/ SC/ FM structure using a spin dependent version of Ohm's law and the diffusion equation for the spin splitting  $\mu_{\uparrow} - \mu_{\downarrow}$  [39].

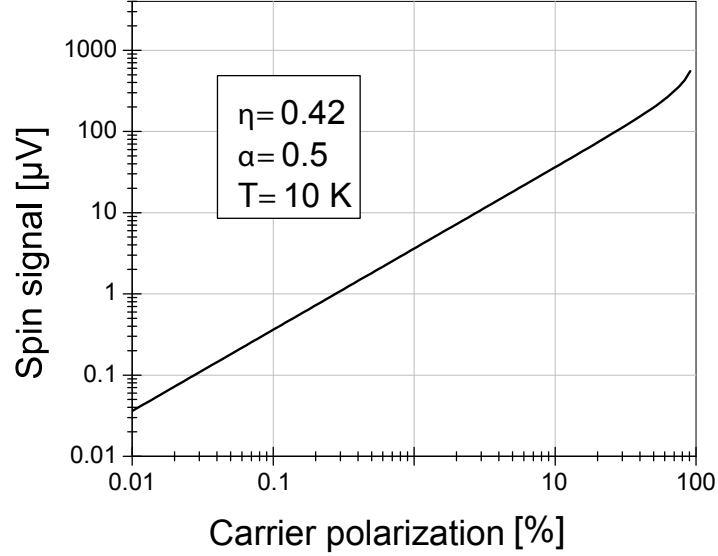


Figure 2.3: Calculated spin signal amplitude in dependence of the current polarization  $p$  using a FM voltage probe with  $\eta=0.42$  and  $\alpha=0.5$  according to Equation 2.6.

They showed that due to the different conductivities of FM and SC, the voltage drop in an FM/SC system is mostly across the semiconductor. The spin information of the FM can not be measured with a metal contact alone.

One solution to this problem is a high resistive contact between FM and SC or a fully spin polarized FM (*half-metal*).

Fortunately, at most of metal/SC interfaces a resistive interface layer forms automatically, the Schottky barrier. Depending on the exact form of the Schottky barrier, electrons from the FM have to tunnel through this barrier. A wider barrier width increases the resistance, whereas a very thin barrier is transparent (*ohmic*). The Schottky barrier is discussed in more detail in subsection 3.3.1.

Another option is an amorphous or crystalline tunnel barrier between FM and SC made of another material. This concept has been used e.g. in spin-injection experiments from Fe in Si with a MgO tunnel barrier or from CoFe in GaAs with an  $\text{Al}_2\text{O}_3$  barrier [40] [41].

## 2.2 Experimental detection of spin injection

In the following, two detection mechanisms for spin accumulation are presented which have been pursued in this thesis. The first one, an electrical measurement technique, has been used throughout the spintronics community successfully, including the following FM/SC systems: Fe/GaAs (Lou *et al.* [42]); Fe/Si (van t’Erve *et al.* [43], Dankert *et al.* [44]); MnAs/GaN (Jahangir *et al.* [16]).

The second approach takes into account optical selection rules of III-V semiconductors. This technique, known as *Spin LED*, has been used extensively in the GaAs system e.g. by Jonker *et al.* [45] and Ramsteiner *et al.* [46]. For the nitrides a couple of *Spin LEDs* have been measured, too. E.g. by Banerjee *et al.* [13] and Ham *et al.* [47].

### 2.2.1 Electrical detection with a 3-terminal and 4-terminal setup

The electrical measurement senses the spin signal  $V_{\text{Spin}}$  in a lateral geometry as depicted in Figure 2.4. Depending on the configuration, three or four electrodes are structured on the semiconductor. Between two adjacent outer contacts an electrical current is sent. One electrode (2) serves as an injector for spins, it has to be ferromagnetic. The outer current electrode (1) can be either non magnetic or ferromagnetic. In this thesis, all electrodes are ferromagnetic.

Two cases have to be distinguished. In the 3-terminal setup, the spin signal is measured between the injecting pad and a remote pad outside the current path ( $V_{3T}$ ). In the case of the 4-terminal setup, a 4th electrode, the ferromagnetic spin sensor (3) is needed, which has to be placed within the spin diffusion length to the injecting electrode (2).

In both cases, spin polarized electrons are injected and diffuse away from the injection point. The measured voltage  $V_{4T}/V_{3T}$ , probes the spin accumulation relative to the accumulation at the reference contact. At the reference electrode (4), the spin accumulation is zero, because it can be assumed that all spins are dephased after such a long distance,  $\Delta\mu = 0$ . Therefore, the measured voltages are:

$$eV_{V_{4T}/V_{3T}} = \pm\mu_{\text{FM}\uparrow/\downarrow} - (\pm\mu_{\text{FM}\uparrow/\downarrow}^0) = \frac{1}{2}\Delta\mu\eta\alpha \quad (2.7)$$

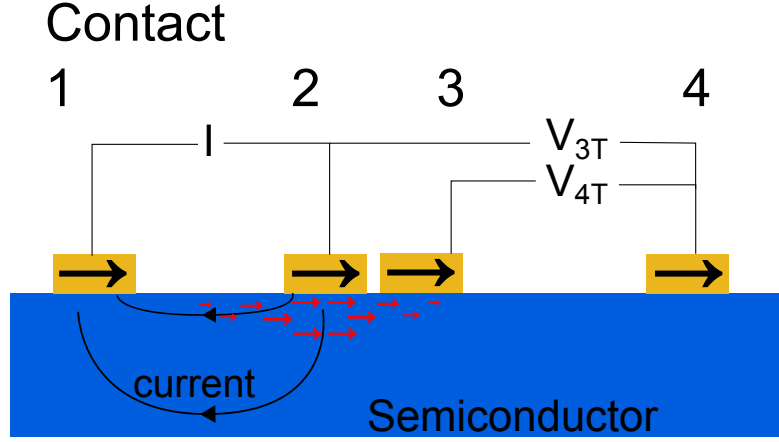


Figure 2.4: Setup for the all electrical spin injection experiments. An electrical current is sent from 2 to 1. The injected spins are measured directly at contact 2 (3-terminal) or sensed non-locally at contact 3. Contact 4 is the reference electrode with  $\Delta\mu=0$ .

In the 3-terminal geometry, the spin accumulation of the region directly under the injection contact is measured, whereas in the 4-terminal geometry, the spins have to reach the detection electrode. Here, the charge current is spatially separated from the spin current. Therefore, this geometry is also known as *non-local geometry*, a pure spin current is measured.

The disadvantage of the *non-local geometry* is the short distance needed between the injection and detection electrode, because spins have to reach the contact. Typical spin diffusion lengths for III-V semiconductors are of the order of 0.1 (GaN [16]) -  $6\mu\text{m}$  (GaAs [42]), in silicon the diffusion length can be microns or even hundreds of microns long [40] [48]. A short diffusion length makes the preparation far more complicated than the 3-terminal setup (electron beam lithography for sub  $\mu\text{m}$  structures).

The 3-terminal geometry has problems, too. According to Txoperena *et al.*, it is possible that in 3-terminal measurements a spin accumulation in the interface is measured and not in the bulk material [49]. To rule out this option, a scaling behavior of the spin life time with different dopings serves as a proof for a spin accumulation in the semiconductor [16]. Surprisingly, the extracted spin signals from 3-terminal measurements are larger than predicted by theory and measured in 4-terminal. Uemura *et al.* addressed this issue and came to the conclusion that 3-terminal measurements are not suitable for evaluation of the exact value of  $V_{\text{Spin}}$  and  $\Delta\mu$  [50]. According to their work, the origin of the enhanced spin signal is a modulation of the tunnel transmission  $\alpha$  in a magnetic field. The authors state that in 4-terminal

measurements, the measured values agree very well with theory.

To check for spin injection two setups are possible. First, a *spin-valve* setup in which the magnetization of the electrodes is changed subsequently by an external applied magnetic field. The change of magnetization alters the voltage signal  $V_{Spin}$  as the ferromagnetic voltage probe senses spin up or spin down electrons, respectively (*magneto resistance*, e.g. [43]).

Another concept dated back to the 1920s can be applied, too, the *Hanle effect*. In the original experiment, absorption and emission of excited states in gases under the influence of a magnetic field is investigated. In the experiment, the precession of atomic dipoles in a magnetic field lead to a dephasing of the total ensemble. From the obtained data, atomic lifetimes can be extracted [51].

This concept has been adopted to spin injection experiments, first in FM/metal structures, later on in FM/SC heterostructures.

### Hanle effect in semiconductors

Before the measurement, the injection (and detection) electrode/s of the 3- or 4-terminal setup has/have to be magnetized in one direction, e.g. in-plane. If a weak magnetic field  $B$  is applied perpendicular to the magnetization of the injection contact, the accumulated spins will start to precess around the magnetic field lines and start to dephase, leading to suppression of  $V_{Spin}$  for higher fields. In this context, it has to be verified that the contacts are not re-magnetized by the perpendicular field. A successful injection of spins can be demonstrated by measuring the voltage  $V_{3T/4T}$  versus the applied magnetic field, Figure 2.5. From the width of the curve, the spin lifetime can be extracted.

### 2.2.2 Optical detection with a LED structure

The basic idea behind an optical proof of spin injection is the analysis of the emitted light when spin polarized electrons recombine with unpolarized holes inside a quantum well (QW).

In the III-V semiconductors  $(\text{In,Al,Ga})\text{As}$  ( $\text{Al}_x\text{Ga}_{1-x}\text{As}$  for  $x < 0.4$ ) and  $(\text{In,Al,Ga})\text{N}$ , the probability of light absorption and emission at the  $\Gamma$  point is the highest. Transitions with the same wave vector are called *direct* transitions. Therefore, the above mentioned semiconductors are *direct band gap* semiconductors.

The conduction band in these semiconductors has a two-fold degeneracy with

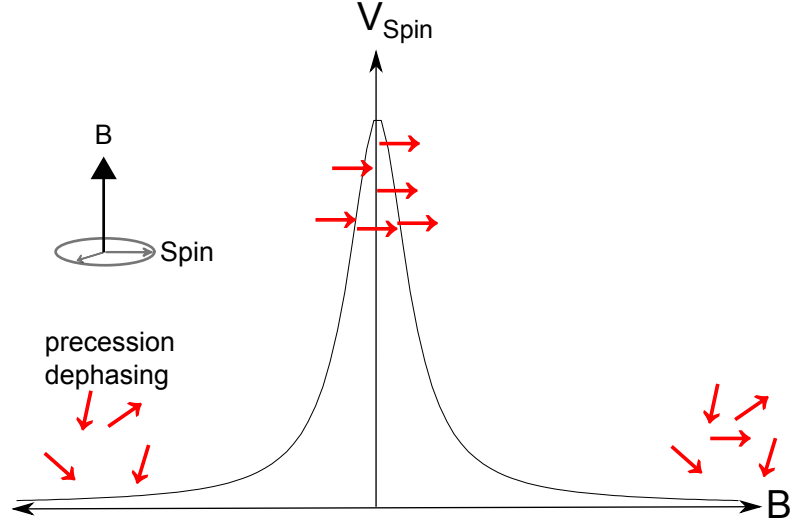


Figure 2.5: Sketch of the Hanle effect in semiconductors. When a small magnetic field is applied perpendicular to the magnetization of the electrode, the injected spins will start to dephase. From the width of the curve, the spin relaxation time can be extracted.

spin-up and spin-down electrons ( $m_j = \pm 1/2$ ).

In the zincblende crystal structure, the valence band splits into four-fold degenerate sub-bands plus a spin split-off band which is separated by an energy of  $\Delta_{SO}$  from the others. In the wurtzite crystal structure, the four-fold degeneracy of the sub-bands is lifted due to polarization fields along the  $c$ -axis. The highest energy bands in the valence band are called heavy hole (HH), ( $m_j = \pm 3/2$ ), and light hole (LH), ( $m_j = \pm 1/2$ ), Figure 2.6. Due to its lower energy, the spin split-off band does not play a role in electro luminescence transitions. In photo luminescence experiments with photon energies  $\hbar\omega \gg E_g + \Delta_{SO}$ , the spin split-off band has to be included explicitly in the transition probability for electron-hole recombinations (for this particular case, see [52]).

Optical transitions between electrons and holes obey optical selection rules as depicted in Figure 2.6 [53] [54].

The magnetic quantum number difference between electrons and holes has to be  $\Delta m_j = \pm 1$  (in units of  $\hbar$ ) in order to conserve the total angular momentum  $J$ . E.g. for spin down electrons, ( $m_j = -1/2$ ), transitions to ( $m_j = -3/2$ ) (HH) and ( $m_j = +1/2$ ) (LH) are allowed. These transitions emit circular polarized light  $\sigma^\pm$ .

For completeness, in quantum wells the quantum confinement allows transitions from  $m_j = \pm 1/2$  electrons to  $m_j = \pm 1/2$  holes ( $\Pi$  transition, transverse



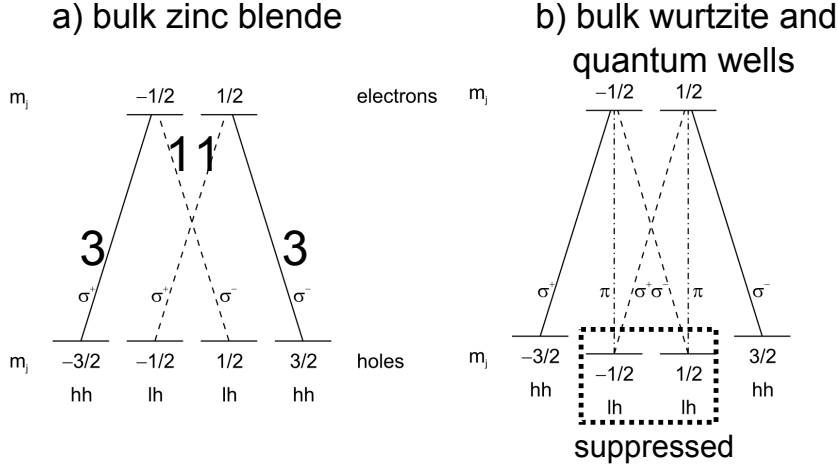


Figure 2.6: Optical selection rules in direct band gap a) zinc blende bulk semiconductors and b) bulk wurtzite and QW structures. The e-HH transition ( $m_j = \pm 3/2$ ) probability is three times larger than the e-LH transition ( $m_j = \pm 1/2$ ). In the QW, e-HH transitions dominate due to an energy splitting of LH/HH bands. Adapted from [54].

magnetic (TM) polarization) [55].

The probabilities for heavy hole and light hole transitions are different. The HH transition in the bulk material is three times larger than the corresponding LH transition.

Depending on the population of the states for spin up and spin down electrons, the degree of circular polarization is given by [45]:

$$\rho_{\text{circ}} = 0.5 \frac{n_{\uparrow} - n_{\downarrow}}{n_{\uparrow} + n_{\downarrow}} = 0.5p \quad \text{four fold degeneracy, bulk zincblende} \quad (2.8)$$

$$\rho_{\text{circ}} = \frac{n_{\uparrow} - n_{\downarrow}}{n_{\uparrow} + n_{\downarrow}} = p \quad \text{two fold degeneracy, wurtzite \& QW} \quad (2.9)$$

where  $p$  is the electron spin polarization.

Therefore, a measurement of  $\rho_{\text{circ}}$  of the emitted light is directly related to the spin polarization of electrons. A 100% spin polarization will give 50% circular polarized light in the four fold degeneracy case and 100% in the two-fold case due to the energetically unfavorable LH recombination.

## 2.3 State of the art

The spin dynamics in silicon and GaAs is well understood. In both materials room temperature spin injection has been demonstrated successfully [14] [15]. In the following, an overview of the most important works on spin transport in GaN is given.

One of the first optical spin relaxation experiments was performed by Beschoten *et al.* [7]. They used time-resolved Faraday rotation to measure electron spin coherence in n-type GaN epilayers grown by MOCVD. At low temperatures, spin lifetimes up to 20 ns at 5 K have been measured, Figure 2.7 a). Buß *et al.* used a similar technique to measure the spin dephasing over a wider temperature range from 80-295 K [56], Figure 2.7 b). The temperature dependence revealed that the *D'yakonov-Perel* (DP) mechanism is the dominant spin relaxation mechanism in GaN (more about the DP mechanism can be found in chapter 4). At room temperature, spin lifetimes of 75 ps (undoped) and 50 ps ( $n=2 \cdot 10^{17} \text{cm}^{-3}$ ) have been measured by the authors.

In the one and only all electrical spin injection experiment in GaN by Jahangir *et al.*, a ferromagnetic MnAs layer has been used as injector [16]. In a 3-terminal geometry, spin lifetimes of 45 ps were obtained for a doping of  $n=2 \cdot 10^{17} \text{cm}^{-3}$  at 300K.

GaN based spin LEDs have been investigated, too. Buyanova *et al.* examined Mn doped GaN, (Ga,Mn)N, spin LEDs [57]. The authors did not find any spin related signal in the room temperature electro luminescence (EL). The authors state that due to a freeze-out of carriers, a low temperature EL measurement was not possible.

In 2006 Ham *et al.* presented EL measurements of (Ga,Mn)N spin LEDs with a measured optical circular polarization of 1.5% at 8 Tesla. Unfortunately, the authors did not show data of a non magnetic test sample. As mentioned by the authors, a Zeeman splitting in the quantum well can lead to a polarization as well (see section 4.2). Therefore, it is not clear if the measured polarization can be attributed to (Ga,Mn)N alone. Banerjee *et al.* used Cr doped GaN as a spin injector in an LED [13]. They measured polarization values of 2.5% at 200 K. In their LED, the injected spin polarized carriers had to travel over  $1 \mu\text{m}$  from the GaN:Cr injection contact to the QW region. Despite the problem of a freeze-out of carriers at low temperatures, a polarization of 6% at 5 K has been obtained by the authors. This could be achieved by a complicated LED structure which emits enough light for the measurement even at low temperatures.

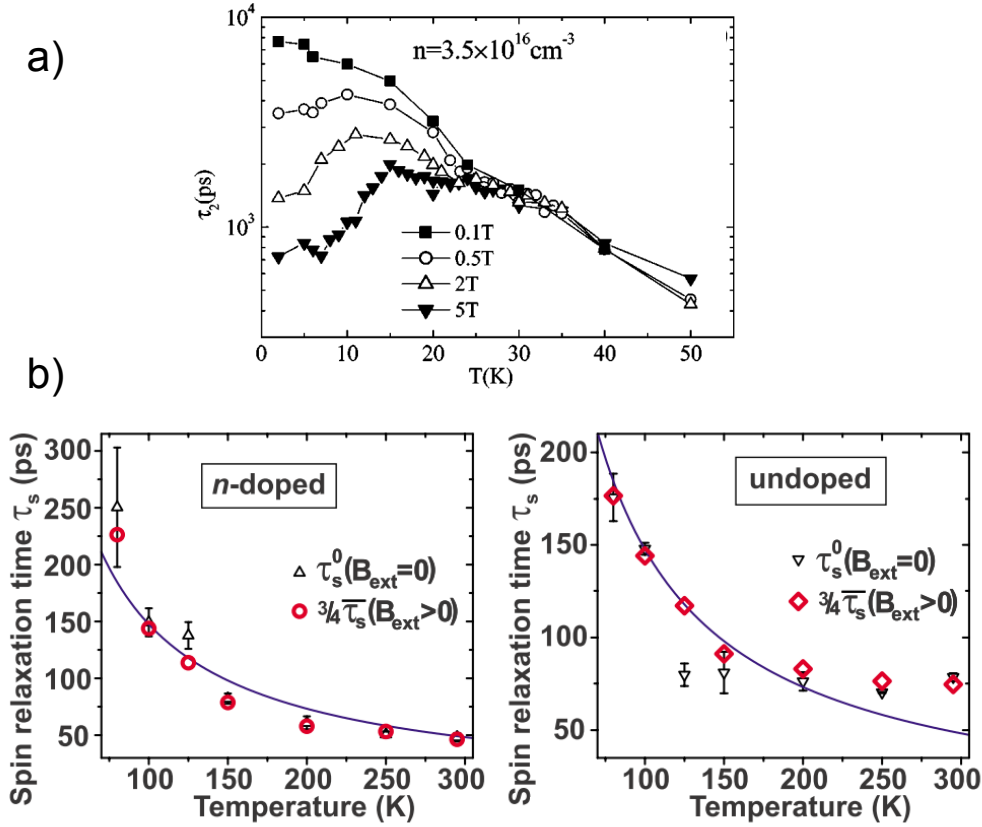


Figure 2.7: Overview of measured spin relaxation times with optically generated spins in GaN. Figure a) shows the dependence of the spin scattering time  $\tau_2$  on temperature for different magnetic fields measured by Beschoten *et al.* for a sample with a low doping of  $n=3.5 \cdot 10^{16} \text{ cm}^{-3}$ . Reprinted figure with permission from [7] Copyright (2001) by the American Physical Society. In b) the data of Buß *et al.* is shown. The temperature dependence over a wide temperature range agrees well with a spin relaxation according to the DP mechanism (solid lines). The red data points denote measurements where the averaged value  $\bar{\tau}_s$  for different magnetic fields have been used. Reprinted figure with permission from [56]. Copyright (2010) by the American Physical Society.

## 2.4 MnGa as a possible spin injector for GaN

The binary alloy  $\text{Mn}_x\text{Ga}_{1-x}$  with  $x=0.5-0.55$  has been used successfully in a (Al,Ga)As based spin LED by Adelman *et al.* [58]. With  $\text{Mn}_x\text{Ga}_{1-x}$  a spin polarization of 6% at 2 K has been achieved by the authors. The  $\text{Mn}_x\text{Ga}_{1-x}$  layers were grown in the (001) direction on (Al,Ga)As(001). Due to the hard axis of the  $\text{Mn}_x\text{Ga}_{1-x}$  layers in the growth direction, a transverse magnetic field could be applied without a change of the magnetization. With this transverse field a Hanle effect could be measured. The data is depicted in Figure 2.8. The width of the Hanle curve changes with the bias voltage. The authors attribute this behavior to a decrease in the recombination time with increasing voltage. Therefore, the recombination and spin lifetimes are directly affected by the bias of the diode.

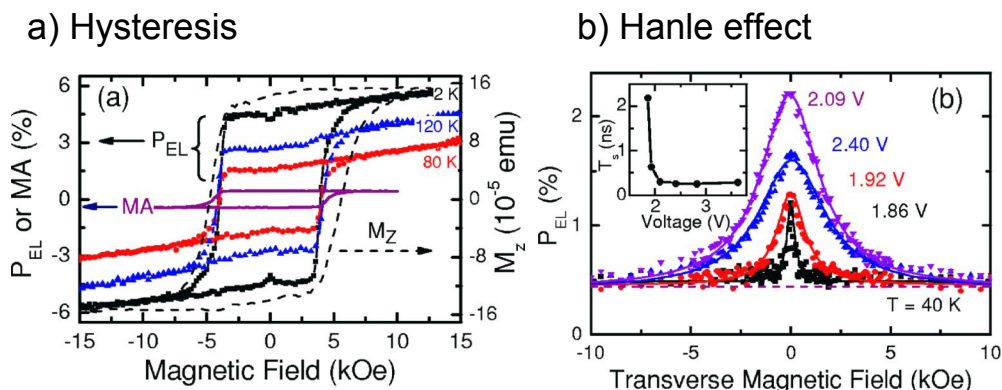


Figure 2.8: The result for a  $\text{Mn}_x\text{Ga}_{1-x}$  / GaAs spin LED. a) shows the magnetic field dependence of  $\rho_{\text{circ}}=P_{\text{EL}}$  at different temperatures, the magneto-absorption (MA) of the 7.5 nm thick film and the out of plane magnetization ( $M_Z$ ) of the  $\text{Mn}_x\text{Ga}_{1-x}$  film. In b) the Hanle effect is demonstrated by an applied small magnetic field perpendicular to the magnetization axis of the film. Reprinted with permission from [58]. Copyright (2006), AIP Publishing LLC.

An application of  $\text{Mn}_x\text{Ga}_{1-x}$  in the nitride system as a spin injector seems promising. Lu *et al.* performed RHEED experiments and grew  $\text{Mn}_x\text{Ga}_{1-x}$  on GaN(0001) epitaxially by MBE [59]. The hexagonal MnGa(111) plane grows with a  $30^\circ$  rotation with respect to the underlying GaN(0001) surface. According to the authors, the abrupt metal/semiconductor interface and good epitaxial match on GaN(0001) make  $\text{Mn}_x\text{Ga}_{1-x}$  a promising ferromagnet for spin injection in GaN.

Experiments in our group addressed the structural, magnetic and transport

properties of  $\text{Mn}_x\text{Ga}_{1-x}$  / GaN heterostructures with  $x=0.49-0.67$  [60]. The work revealed that an epitaxial growth on GaN(0001) is possible over a wide range of alloy composition and that the magnetic and structural properties are tunable by varying the alloy composition. A TEM picture of the interface showed an interface of high crystal quality with an abrupt change from GaN to  $\text{Mn}_x\text{Ga}_{1-x}$  planes.

These results show that  $\text{Mn}_x\text{Ga}_{1-x}$  is a prospective candidate for spintronic applications in GaN based devices.



# Chapter 3

## MnGa/ GaN heterostructures

### 3.1 MnGa bulk properties

#### 3.1.1 Structure

The binary alloy  $\text{Mn}_x\text{Ga}_{1-x}$  can be grown epitaxially on a variety of different substrates. The most common ones are GaAs [61] [62], MgO [63] [64],  $\text{Al}_2\text{O}_3$  [64] [65] and GaN [59]. The phase diagram of the  $\text{Mn}_x\text{Ga}_{1-x}$  alloy is shown in Figure 3.1.

$\text{Mn}_x\text{Ga}_{1-x}$  crystallizes depending on the ratio of manganese to gallium and temperature in different phases. Especially when samples are grown at the boundary of one phase, segregation into other phases can occur. This segregation is usually not seen in RHEED experiments, but a XRD scan in the  $\theta - 2\theta$  geometry reveals other structures as well. Therefore, it is useful to check the composition and structure of the layers with XRD in addition to RHEED.

The phases grown in this thesis are mostly the  $L1_0$ -*AuCu* phase. It is worth mentioning that in some publications this phase is called  $\delta$ -MnGa or  $\text{Mn}_{3-\delta}\text{Ga}$ , too. In the following, for simplicity, only the expression  $\text{Mn}_x\text{Ga}_{1-x}$  will be used for all alloys in the  $L1_0$  structure.

The *AuCu* crystal structure is stable from  $x=0.49 \dots 0.67$ . For concentrations above 67% Mn, the unit cell doubles along the  $c$  axis [67]. For these high concentrations different names have been established. The  $\text{Mn}_x\text{Ga}_{1-x}$  alloys are called  $\text{D0}_{19}$ - $\text{Mn}_2\text{Ga}$  ( $\text{Mn}_x\text{Ga}_{1-x}$  with  $x=0.67$ ) or  $\text{D0}_{22}$ - $\text{Mn}_3\text{Ga}$  ( $\text{Mn}_x\text{Ga}_{1-x}$  with  $x=0.75$ ). The  $\text{D0}_{22}$  phase has been studied extensively due to its possible half-metallicity, high Curie temperature and large magnetic anisotropy [68]

### 3.1. MnGa bulk properties

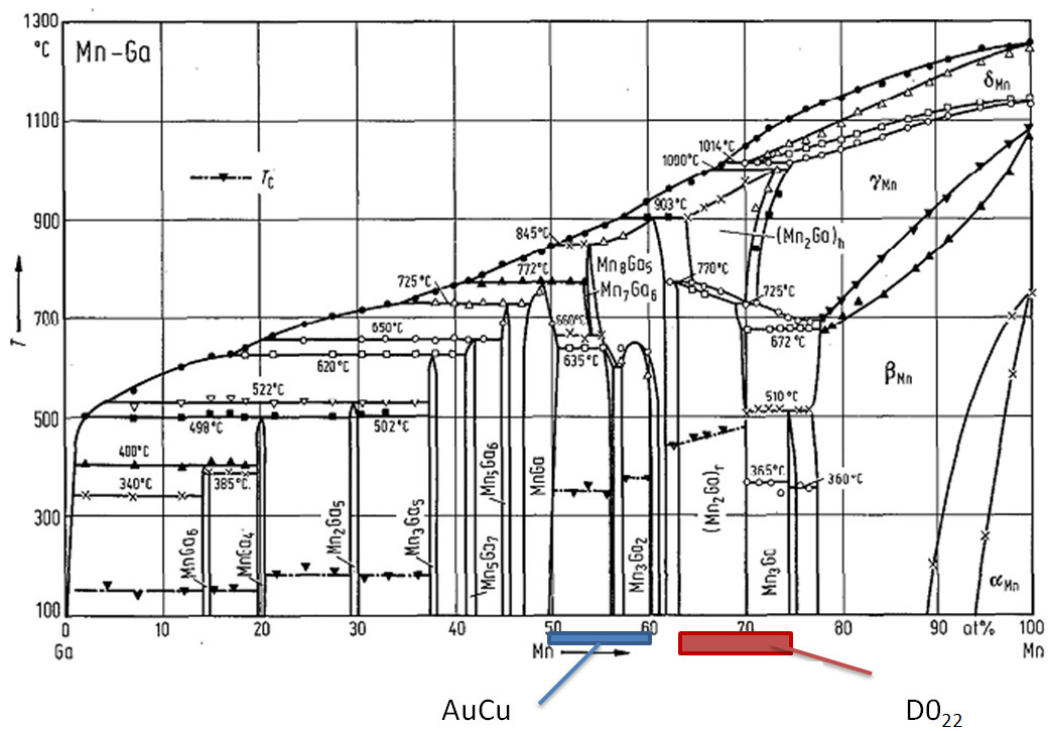


Figure 3.1: Phase diagram of the binary alloy  $Mn_xGa_{1-x}$ . The relevant phases AuCu and  $DO_{22}$  are marked. Adapted from [66].



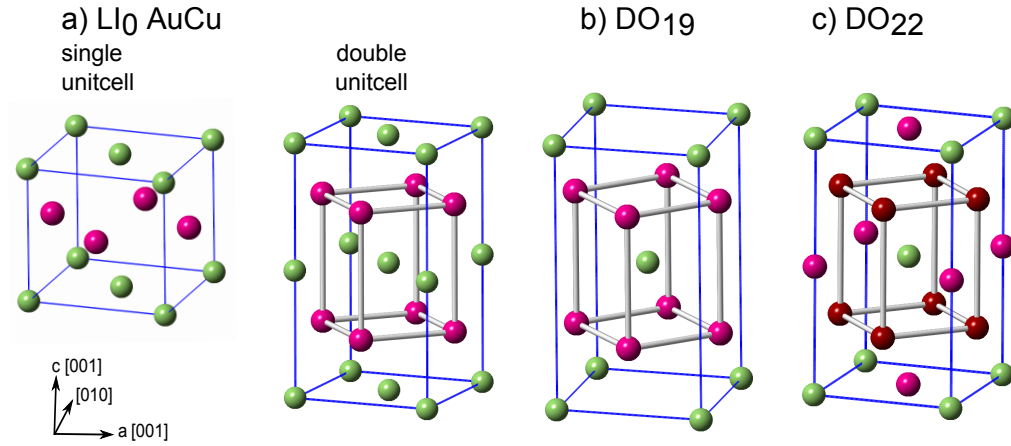


Figure 3.2: Unit cells of  $Mn_xGa_{1-x}$  for different Mn:Ga ratios. Ga atoms are in green colors and Mn atoms in purple. a)  $Mn_xGa_{1-x}$  with  $x=0.5$ . The crystal structure is  $L1_0$  type, which is often called *AuCu* because Gold and Copper alloys crystallize in this structure. It is a face-centered cubic structure with Pearson symbol  $tP4$ . The space group is  $P4/mmm$ . For higher concentrations, the symmetry changes to b)  $DO_{19}$  ( $x=0.67$ ) and c)  $DO_{22}$  ( $x=0.75$ ) (2 different spin states for Mn in this case (purple and red)).

[69] [70] [71]. The crystal structure of all mentioned alloys is sketched in Figure 3.2.

XRD scans of approx. 250 nm thick  $Mn_xGa_{1-x}$  layers grown on GaN(0001) templates with different Mn concentrations are shown in Figure 3.3 (from our paper Bedoya *et al.* [60]). The  $\theta$ - $2\theta$  scan shows that *AuCu-type*  $Mn_xGa_{1-x}$  grows in the [111] direction oriented parallel to the sapphire(0001)/ GaN(0001) axis over a wide range of alloy composition from  $x=0.49 \dots 0.67$ .

Table 3.1 summarizes the lattice parameters and full width at half maximum values (FWHM) of the  $Mn_xGa_{1-x}$  layers deduced from the XRD measurements. The measurement of the lattice constants  $a$  and  $c$  revealed that with increasing manganese concentration the  $c$  lattice constant increases while the  $a$  lattice constant does not change. The crystal quality has been addressed in the paper, too: "Regarding the crystal quality of the layers, there is a clear trend of larger FWHM values toward higher Mn concentrations. From the width of both  $2\theta$  and  $\omega$  reflections, [...] the structural coherence length and the crystal quality decrease as the Mn:Ga ratio deviates from stoichiometry. While the AuCu- $L_{10}$  structural phase seems to be stable up to  $x = 0.67$ , the arrangement of the excess Mn-atoms in the structure is not known, [...]", from Bedoya *et al.* [60].

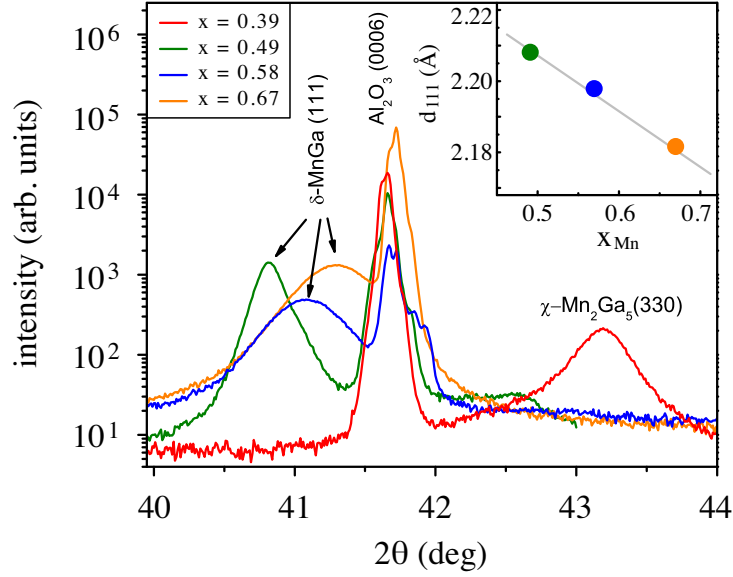


Figure 3.3: XRD scans of  $\text{Mn}_x\text{Ga}_{1-x}$  grown on  $\text{GaN}(0001)$  with  $x=0.39 \dots 0.67$ . For a manganese concentrations of  $x=0.39$  a different phase grows. The inset shows the change of the lattice constant  $d_{111}$  with manganese concentration. From [60].

The  $\text{Mn}_x\text{Ga}_{1-x}$  layers investigated in the paper differ from the grown layers in this thesis in two important points. First, the substrate temperature for  $\text{MnGa}$  growth in the paper is  $250^\circ\text{C}$  and the growth rate is approx.  $2\text{-}3\text{nm}/\text{min}$ . As mentioned in the MBE chapter, the growth rate could not be increased over  $0.5\text{-}0.8\text{nm}/\text{min}$  due to the new setup of the Mn effusion cell. XRD scans of  $\text{Mn}_x\text{Ga}_{1-x}$  layers grown under the new conditions show the same trend in terms of lattice parameter and strain.

Table 3.1: Lattice parameters and FWHM values of the  $\text{Mn}_x\text{Ga}_{1-x}$  epitaxial layers [60].

$x$	$d_{111}$ ( $\text{\AA}$ )	$c$ ( $\text{\AA}$ )	$a$ ( $\text{\AA}$ )	$\Delta 2\theta_{111}$ ( $^\circ$ )	$\Delta 2\theta_{200}$ ( $^\circ$ )	$\Delta 2\theta_{002}$ ( $^\circ$ )	$\Delta\omega_{111}$ ( $^\circ$ )	$\Delta\omega_{200}$ ( $^\circ$ )	$\Delta\omega_{002}$ ( $^\circ$ )
0.49	2.208	3.742	3.883	0.21	0.31	0.45	0.48	1.08	0.58
0.58	2.198	3.699	3.886	0.34	0.61	1.08	0.89	1.92	-
0.67	2.186	3.659	3.886	0.47	0.64	1.45	0.87	2.19	2.21

### 3.1.2 Magnetic properties

The magnetic properties of the  $\text{Mn}_x\text{Ga}_{1-x}$  layers have been measured with *SQUID* (superconducting quantum interference device) and *VSM* (vibrating sample magnetometer). Layers thicker than approx. 10nm can be measured with VSM. The smallest magnetic moment VSM can resolve is  $10^{-6}$  emu ( $\cong 10^{-9} \text{Am}^2$ ), which is 100 times higher than the smallest moment SQUID can sense. The advantage of the VSM unit is the possibility to measure up to temperatures of 1000K. Therefore, it can be used to measure Curie temperatures for practically all ferromagnets.

From the SQUID measurements at 300 K two trends in the studied composition range can be observed: "While the saturation magnetization  $M_s$  is found to decrease with increasing Mn-content, the coercive field shows the opposite trend as depicted in Figure 3.4[...], these observations are in agreement with previous reports of bulk MnGa and of thin films of MnGa grown on GaAs or GaN [72], [73, 62, 74], [59].", from Bedoya *et al.* [60]. The incorporation of additional Mn-atoms ( $x \geq 0.5$ ) alters the strain state of the AuCu-L1<sub>0</sub> structure, as discussed in the previous XRD section. A clear distinction between alloy composition and strain is not possible because both are interdependent on each other. According to a theoretical study by Sakuma *et al.*, the excess Mn-atoms have an antiparallel alignment to the rest Mn atoms, leading to a decrease of the magnetic moment [75]. The strain dependence of stoichiometric  $\text{Mn}_{0.5}\text{Ga}_{0.5}$  has been calculated by Yang *et al.*. They found that a reduction of the  $c$  lattice parameter leads to a smaller magnetic moment [76]. Therefore, "the decrease of the magnetic moment with increasing Mn concentration and simultaneous decrease of the  $c$  lattice constant, is in qualitative agreement with the trends predicted by theory", which is one of the conclusions in the paper [60].

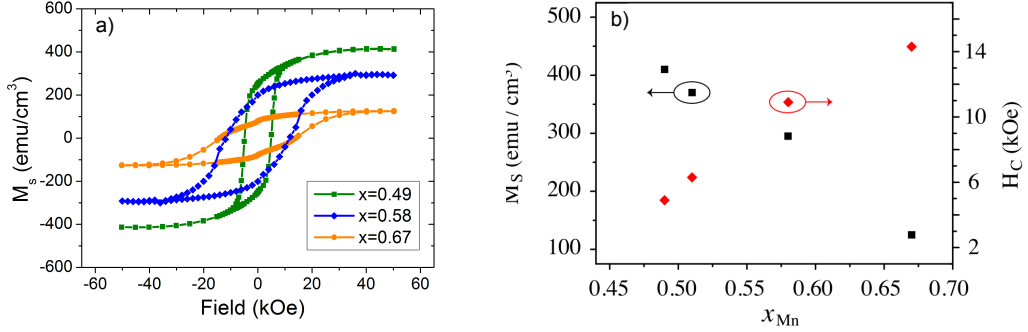


Figure 3.4: (a) Field-dependent magnetization of  $\text{Mn}_x\text{Ga}_{1-x}$  layers at 300K measured with SQUID. (b) Composition dependence of saturation magnetization and coercive field. Taken from [60].

## 3.2 MnGa/GaN Interface

### 3.2.1 RHEED

The detailed knowledge of the ferromagnet/semiconductor interface is one key parameter for achieving a successful spin injection from the ferromagnet into the semiconductor. With RHEED, a powerful in-situ diffraction technique is available, which can be used to monitor the epitaxial growth on the monolayer thickness scale.

For the system  $\text{Mn}_x\text{Ga}_{1-x}$  on GaN(0001) Lu *et al.* conducted RHEED experiments showing that  $\text{Mn}_x\text{Ga}_{1-x}$  grows epitaxially on GaN(0001) with an abrupt change from GaN to  $\text{Mn}_x\text{Ga}_{1-x}$  diffraction spots indicating a sharp interface between metal and semiconductor [59]. Furthermore, a  $30^\circ$  rotation of the  $\text{Mn}_x\text{Ga}_{1-x}$  (111) plane relative to the GaN(0001) surface was observed. To get a better understanding of the growth of  $\text{Mn}_x\text{Ga}_{1-x}$  on GaN(0001), a couple of experiments have been performed. This includes the investigation how different Mn:Ga concentrations and substrate temperatures influence the grown layer. The XRD data show that  $\text{Mn}_x\text{Ga}_{1-x}$  crystallizes in the [111] direction parallel to the GaN [0001] direction. The (111) plane of stoichiometric  $\text{Mn}_x\text{Ga}_{1-x}$  consists of alternating Mn and Ga rows that form a hexagonal lattice. A top view of MnGa(111) layers on GaN(0001) is shown in the last row of Figure 3.6. The in-plane lattice mismatch between GaN and MnGa is 0.5-2% depending on the exact arrangement of the MnGa(111) plane with respect to the underlying GaN(0001) surface.

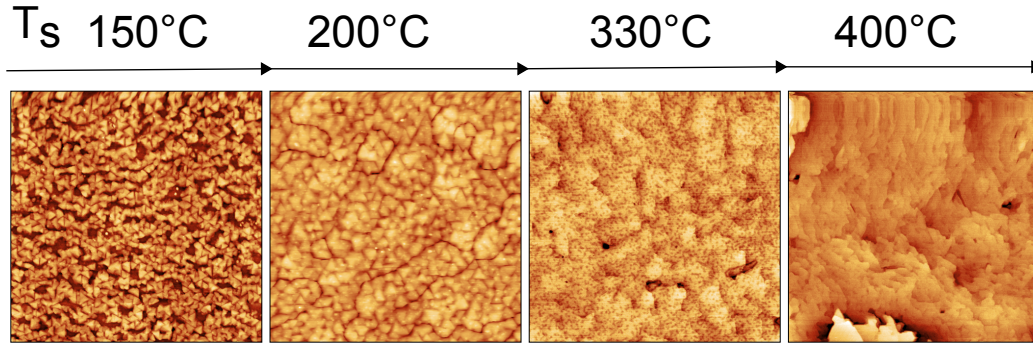


Figure 3.5: AFM morphology pictures of MnGa layers grown at different temperatures on GaN(0001). The scan size is  $5 \times 5 \mu\text{m}^2$  in all cases. The z-scale changes from left to right. At low substrate temperatures, triangular islands grow. An increase in the temperature leads to a coalescence of the islands until a dense layer grows at  $400^\circ\text{C}$ . Growth time 60min in all cases. (samples G1263, G1260, G1277, G1264)

At lower temperatures, the films exhibit cracks and are not closed, which can be seen in the AFM topography of  $\text{Mn}_x\text{Ga}_{1-x}$  films grown at different substrate temperatures, Figure 3.5.

Below a substrate temperature of  $200^\circ\text{C}$ , the films show island growth with triangular structures. Above  $200^\circ\text{C}$ , the film starts to close and a dense layer is obtained at around  $400^\circ\text{C}$ . This is in contrast to the work by Lu *et al.*, who observed a close layer even at a low temperature of  $250^\circ\text{C}$ .

The RHEED patterns along the  $[1\bar{1}00]$  view direction of GaN are shown in Figure 3.6 for two different temperatures. The growth rate is  $0.5 \text{ nm/min}$  in both cases. The influence of the growth rate on the epitaxial relationship has not been investigated because an increase of the growth rate was not possible (problems with the Mn effusion cell, section 1.2).

The RHEED analysis shows the following: For higher temperatures,  $T_s=400^\circ\text{C}$ , rotated  $\text{Mn}_x\text{Ga}_{1-x}$  (111) planes with respect to the GaN(0001) surface grow, Figure 3.6 b) (will be called 'rotated' in the following). Lu *et al.* conducted their experiments at a lower substrate temperature of  $250^\circ\text{C}$  and obtained rotated  $\text{Mn}_x\text{Ga}_{1-x}$  planes, too.

According to the RHEED analysis  $\text{Mn}_x\text{Ga}_{1-x}$  (111) planes are not rotated at a substrate temperature of  $330^\circ\text{C}$ , Figure 3.6 a). The epitaxial orientation of MnGa(111) maps directly the GaN(0001) surface underneath. According to the time evolution plot of the RHEED pattern, the change from GaN to MnGa RHEED diffraction spots is within 2 ML, which shows that both orientations, rotated and non-rotated, form an abrupt interface with GaN.

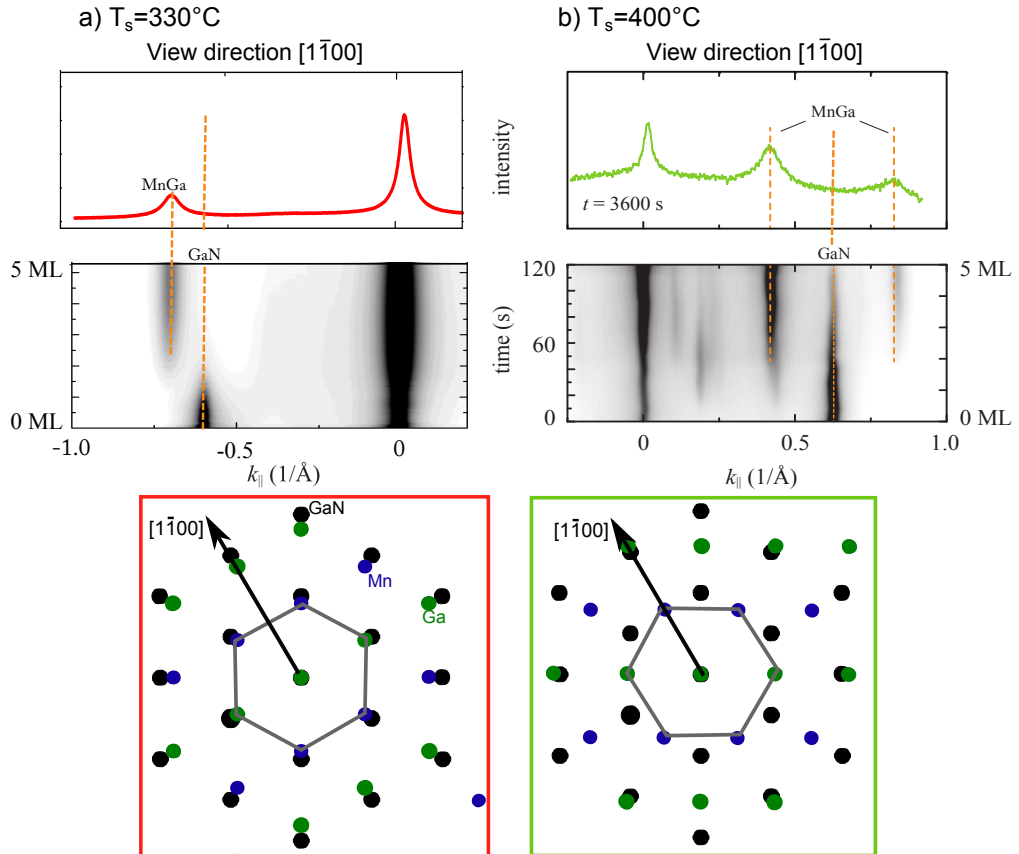


Figure 3.6: Possible orientations of MnGa(111) on GaN(0001) deduced by RHEED. Two epitaxial relationships are possible: a) non rotated planes and b) rotated planes. The first row shows the RHEED intensity profile at the end of the growth process. The evolution of the RHEED diffraction profile is shown in the middle row. After approx. 2 ML coverage, the RHEED pattern of MnGa appears and the GaN diffraction spots vanish. Surface reconstructions at the beginning of the growth process can be seen in the right time evolution plot. The third row shows a model of the Ga polar GaN matrix (in black) together with the surface Mn and Ga atoms.

Other trends have been observed as well. When the Ga bi-layer desorption after the growth of GaN discussed in chapter 1 is not visible in RHEED (due to Ga droplet formation, or a too rough surface), a mixture of rotated and non rotated planes grow.

Furthermore, in the case of a not desorbed Ga layer after the growth of GaN, it is not clear whether the Mn concentration decreases due to the higher Ga content at the very surface. Usually, when a mixture of rotated and non rotated planes grow or the Ga adlayer is not removed, it is difficult to wet etch the  $\text{Mn}_x\text{Ga}_{1-x}$  layer and some residues stay at the surface.

Therefore, it is recommended to get rid of the Ga adlayer on GaN by nitridation and to check the orientation of  $\text{Mn}_x\text{Ga}_{1-x}$  with RHEED at the beginning of the growth process.

### 3.2.2 Transmission electron microscopy (TEM)

According to the RHEED analysis, the MnGa/GaN interface is sharp with an abrupt change from GaN(0001) to MnGa(111) diffraction spots. With TEM another powerful diffraction technique is available that can image samples in cross-section. Two TEM analysis have been performed by other group members. The experiments have been conducted in a FEI ETEM. The high resolution TEM mode (HRTEM) with atomic resolution of the crystal structure has been used to map the very interface of MnGa/GaN. Furthermore, a chemical analysis with electron energy loss spectroscopy (EELS) of the interface has been conducted. EELS can reveal chemical compositions on the nanometer scale and possible contaminations.

First of all, the epitaxial relationship between MnGa and GaN deduced by RHEED matches with the obtained TEM diffraction pictures for both rotated and non rotated planes (not shown).

Secondly, a HRTEM picture shows an atomically sharp  $\text{Mn}_x\text{Ga}_{1-x}$ /GaN interface with an overall good crystal quality for a composition of  $x=0.5$ , Figure 3.7. There are twinning defects visible in the  $[\bar{1}01]$  zone axis of MnGa, but they do not affect the very interface. At the  $\text{Mn}_x\text{Ga}_{1-x}$  surface an oxide of 10nm thickness forms. This is the reason why the  $\text{Mn}_x\text{Ga}_{1-x}$  surface is capped with Al for samples grown for spin injection purposes.

In Figure 3.8 the HRTEM image together with the diffraction pattern is shown for another sample which is grown with a higher  $\text{Mn}_x\text{Ga}_{1-x}$  thickness and a higher Mn concentration of  $x=0.67$ . The higher Mn concentration does not influence the interface quality. The  $\text{Mn}_x\text{Ga}_{1-x}$ /GaN heterostructures with  $x=0.67$  form the same abrupt interface as with  $x=0.5$ .



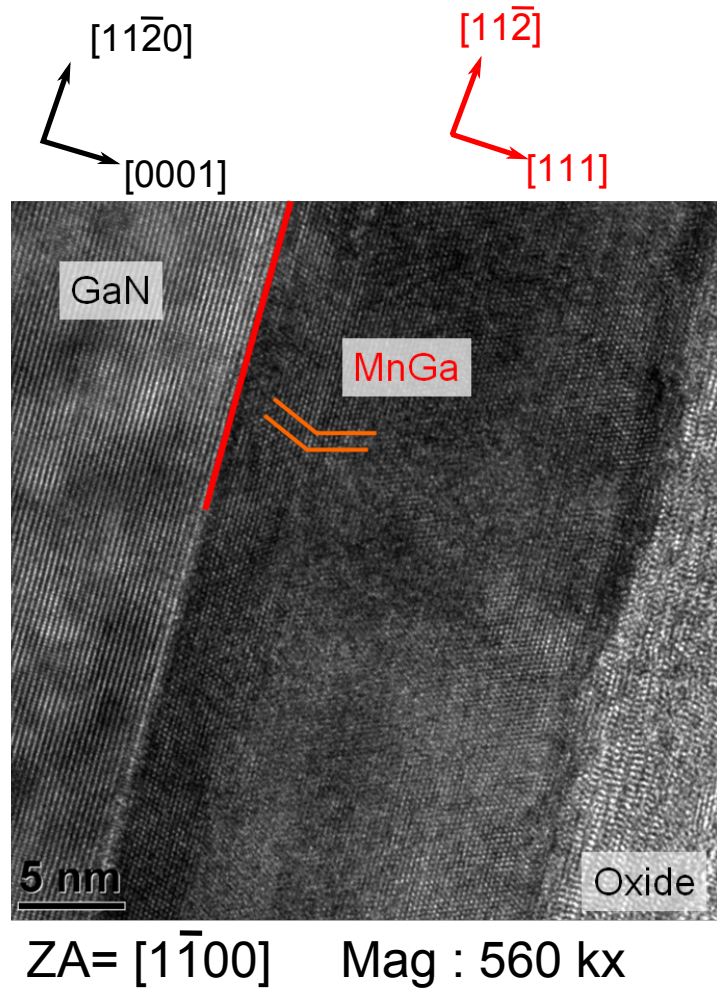


Figure 3.7: HRTEM picture of the  $\text{Mn}_x\text{Ga}_{1-x}/\text{GaN}$  interface with  $x=0.5$  in the  $[1\bar{1}00]$  zone axis of GaN. An atomically sharp interface between  $\text{Mn}_x\text{Ga}_{1-x}$  and GaN forms. At the  $\text{Mn}_x\text{Ga}_{1-x}$  surface an oxide of 10nm thickness can be seen. Twinning defects are indicated in orange. (Sample G1296)

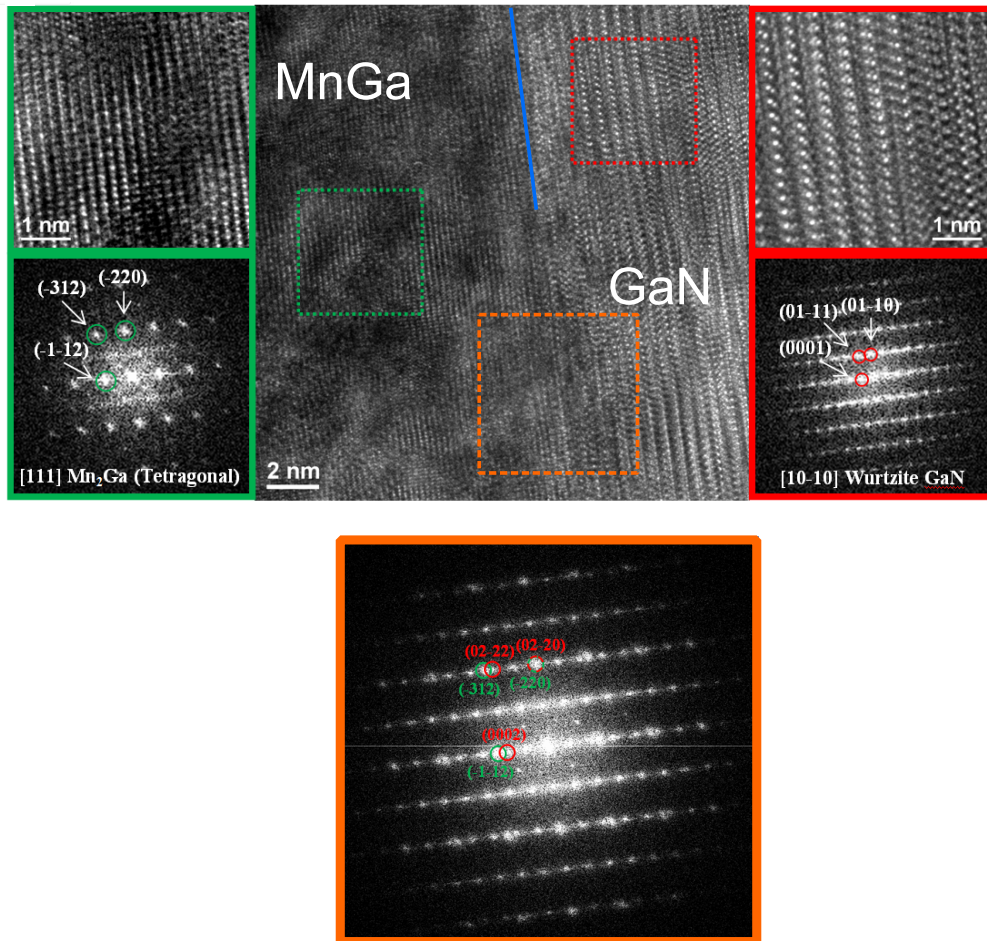


Figure 3.8: The  $\text{Mn}_x\text{Ga}_{1-x}$  / GaN interface with  $x=0.67$  in HRTEM. The subpictures to the left and right show the diffraction patterns of the indicated areas. The orange box shows the diffraction of the interface region. From the pattern, a lattice mismatch of 0.7% can be deduced. (sample G1629)

### Energy electron loss spectroscopy (EELS)

EELS measures the amount of electron energy loss of an incident electron beam by resolving the energy distribution of the scattered electrons. The disadvantage of EELS is the large error in the composition analysis but it wins over energy dispersive x-ray electron spectroscopy (EDX) in terms of spacial resolution. Furthermore, the fine structure of a peak can reveal the chemical bonding of elements [77].

The EELS line profile for the elements N, O, Mn and Ga is shown in Figure 3.9 a) over larger distances of the interface region for sample G1629. The signal of Mn rises after crossing the interface from GaN to MnGa as expected, whereas Ga and N drop simultaneously. The oxygen signal shows an unusual behavior as it seems to rise locally at the interface of GaN and MnGa before it reduces back to the GaN bulk value inside MnGa. There are a couple of possible explanations. First, during the long cool down time of 1.5h from the GaN growth temperature of  $T_s \approx 650^\circ\text{C}$  to the MnGa growth temperature of  $400^\circ\text{C}$   $\text{O}_2$  molecules inside the MBE chamber might chemisorb with the GaN surface. The origin of the residual O might stem from the residual gas from the GaN growth (background pressure during growth  $10^{-6}$ - $10^{-5}$  mbar). During cool down, the background pressure is of the order of  $10^{-7}$ - $10^{-9}$  mbar. A contamination with oxygen is probable during this time but according to other chemisorption experiments by other groups the saturation coverage of O is usually 0.4 ML even under higher oxygen fluxes [78]. Therefore, other sources of contamination have to be taken into account. One might be the manganese material itself. Mn oxidizes quite fast but every material is out gassed after installation at temperatures higher than under typical growth conditions. If oxygen is present inside manganese, the contamination level should be the same throughout the MnGa layer but this is not the case. The last option is an oxidized MnGa layer at the side of the TEM lamella. After preparation of the TEM lamella, the whole lamella is exposed to air and a small oxide might form on the side of MnGa. The electron beam used for the excitation then probes both oxide and MnGa. But also in this case the oxygen distribution should be the same throughout the MnGa layer. All mentioned assumptions could not be checked with other methods which means that the source for the higher O concentration at the boundary is not solved completely.

To check for a possible in diffusion of Mn into GaN as it is reported for higher substrate temperatures of  $500^\circ\text{C}$  by Hwang *et al.* [79], the interesting region is redrawn magnified in Figure 3.9 b) for the elements manganese and nitrogen. Both nitrogen and manganese signals do not show a sharp drop/rise at the

interface. This is expected as instrumental broadening of the electron beam increases the probe region. In order to distinguish a diffusion of manganese from a Gaussian beam profile the nitrogen distribution has been assumed atomically sharp (step function). This function is convoluted with a Gaussian. With this method the position of the interface and the experimental broadening can be fitted. The broadening accounts to  $\sigma=1.5$  nm which seems reasonable for the applied imaging conditions. Applying the same method to manganese, the fit gives a larger value for  $\sigma$ , which shows that the manganese distribution is different than the one of nitrogen. The best fitting result for manganese is obtained by keeping the  $\sigma$  value from the nitrogen fit fixed and assuming a linear grading of the manganese concentration around the interface. The validity of this rough model can be questioned. Without any doubt, the manganese signal behaves differently than the N signal, but a clear indicator for an intermixing is missing.

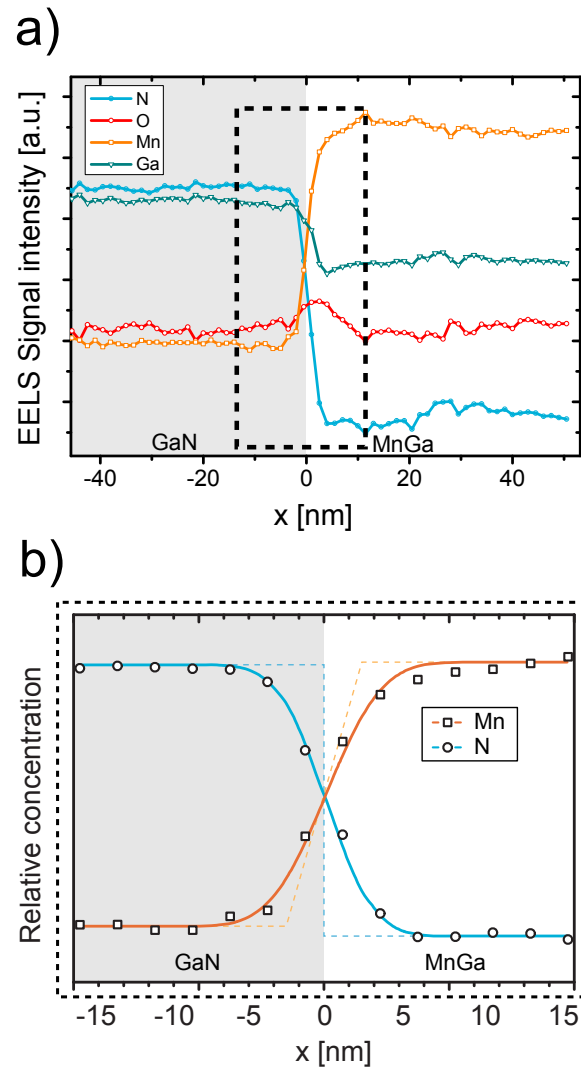


Figure 3.9: Results of the EELS measurement: a) EELS line profile data for the MnGa/ GaN interface over a large region for the elements N, O, Ga and Mn. b) closer view at the interface to estimate the Mn in diffusion into GaN. The relative concentration per element of Mn and N are fitted with a distribution function convoluted with a Gaussian (solid lines). The unconvoluted distribution functions are drawn as dashed lines (see text for details, sample G1629).

### 3.3 Electrical properties of the MnGa/ GaN interface

In order to find the best conditions for efficient spin injection, the MnGa/ GaN interface has been characterized electrically.

One of the challenges for a successful spin injection from a ferromagnetic metal in a bulk semiconductor like GaN is to overcome the conductivity mismatch between metal and semiconductor as stated in chapter 2. One solution are tunnel contacts between metal and semiconductor. Tunnel contacts provide a high interface resistance and therefore solve the conductivity mismatch problem. The tunneling region can be either the built-in schottky depletion region or a grown thin tunnel barrier. In this work the first approach, reversed biased Schottky diodes, has been pursued.

In the beginning of this section, basic concepts of metal semiconductor contacts will be presented. After this small introduction, the interface between metal and semiconductor will be examined in more detail. This includes a description of the role of metal induced gap states in tunneling transport phenomena. At the end, the measured transport properties through the contact will be presented.

#### 3.3.1 Schottky's standard model of metal/ semiconductor contacts

In the beginning 20th century vacuum tubes were used as devices with rectifying current-voltage characteristics. The introduction of semiconductor based diodes lead to an enormous reduction in size and cost. Furthermore, one of the first used semiconductor devices in history is the Schottky diode itself. It is quite impressive that the rectifying behavior of a metal/ semiconductor contact was already described in the 19th century by Ferdiand Braun [80]. He investigated what nowadays is called a metal/ semiconductor/ metal structure. He measured a non linear I-V characteristic. Later in 1939 Walter Schottky, working for *Siemens & Halske A.G.* in Berlin, developed a model for the metal/ semiconductor contact which describes the fundamental working principle of the diode reasonably [81].

A complete overview of the Schottky theory can be found e.g. in the books by S.M.Sze *Physics of semiconductor Devices* or H. Lüth *Solid surfaces, interfaces and thin films* [82] [83].



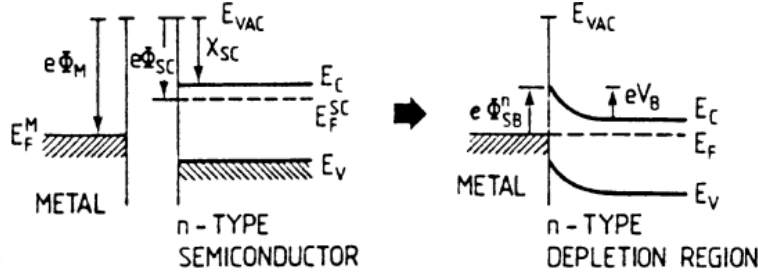


Figure 3.10: Schematic band diagram of the formation of the metal/semiconductor contact in the framework of Schottky. In the shown case, the metal has a high work function and the semiconductor is n-type as it is the case in the studied MnGa/GaN system. Taken from [83].

### 3.3.2 Schottky diode in thermal equilibrium

In equilibrium, the fermi levels of metal and semiconductor align. In this simple picture, this depends only on the work function of the metal  $\Phi_m$  and the electron affinity  $\chi_{SC}$  of the semiconductor, which differs from the work function of the semiconductor  $\Phi_{SC} = E_{vac} - E_f^{SC}$ .

When the two materials are brought in contact a charge transfer sets in automatically. For the case  $\Phi_m > \chi_{SC}$  (larger work function of the metal) and an n-type semiconductor this leads to a negative charge flow from the semiconductor to the metal, leaving positively charged donors  $N_D^+$  behind. Directly at the interface the schottky barrier of height

$$\Phi_{SB} = \Phi_m - \chi_{SC} \quad \text{Schottky-Mott model} \quad (3.1)$$

forms. Solving the poisson equation for this case leads to an electron depletion of width  $w$  inside the semiconductor which is shown in Figure 3.10.

The analytical solution of the band bending in the abrupt approximation (charge  $\rho = eN_D^+$  for  $x=0..w$ ; 0 otherwise;  $N_D^+$  = number of ionized donors) with a polynominal ansatz for the potential  $V(x)$  is:

$$V(x) = V_B - \frac{eN_D^+}{\epsilon_s} \left( wx - \frac{1}{2}x^2 \right) \quad (3.2)$$

with the depletion width

$$w = \left[ \frac{2\epsilon_s}{eN_D^+} \left( V_B - \frac{kT}{e} \right) \right]^{1/2} \quad (3.3)$$

$eV_B$  is the built-in potential energy, it is the difference between the top of the conduction band and the barrier height  $e\Phi_B$  (see Figure 3.10).  $\epsilon_s$  is the dielectric constant of the semiconductor.

The average electron density in metals is approx.  $10^{23} \text{ cm}^{-3}$ , which is orders of magnitudes larger than in semiconductors. For typical doping concentrations in semiconductors,  $n \approx 10^{17}\text{-}10^{18} \text{ cm}^{-3}$ , the depletion layer can be tens of nanometers in width.

### 3.3.3 Forward and reverse biased Schottky diode in the thermionic picture

The external applied bias  $V_{ext}$  raises or lowers the fermi level of the semiconductor relative to the fermi level of the metal, Figure 3.11 a). The formula for the depletion width  $w$  has to be modified to [54]:

$$w = \left[ \frac{2\epsilon_s}{eN_D^*} \left( V_B - V_{ext} - \frac{kT}{e} \right) \right]^{1/2} \quad (3.4)$$

In the *Schottky-Mott* model only transport above the barrier is taken into account, tunneling through the barrier is neglected.

Therefore, a lowering of the semiconductor's Fermi level (negative bias) does not change the current from the metal into the semiconductor  $j_{m \rightarrow s}$ , because the barrier stays nearly constant (a small lowering of the barrier height due to an image force effect at higher reverse biases is small compared to the barrier height).

The current is governed only by the thermionic emission over the barrier which is [82]:

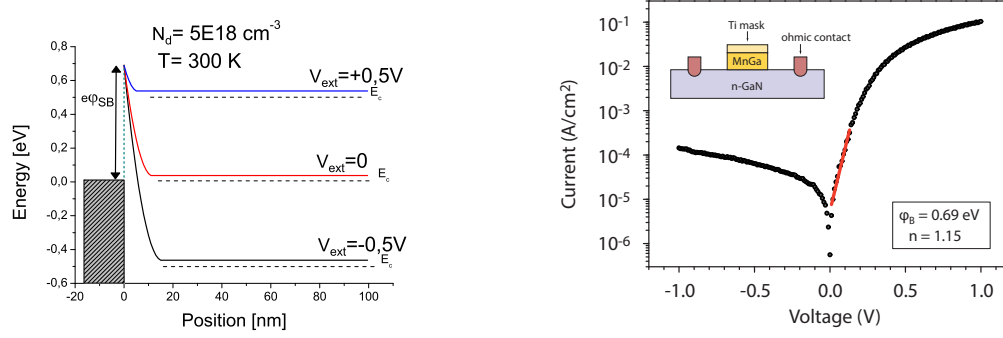
$$j_{m \rightarrow s} \equiv j_s = A^* T^2 \exp\left(\frac{e\Phi_{SB}}{kT}\right) \quad (3.5)$$

$$A^* = \frac{4\pi m^* k^2}{h^3} \quad (3.6)$$

This saturation current  $j_s$  depends only on the barrier height  $\Phi_{SB}$ , the temperature  $T$  and the effective *Richardson* constant  $A^*$  which takes into account the effective mass  $m^*$  of electrons. If the Fermi level of the semiconductor is raised (forward bias), 'hot' electrons from the conduction band can easily overcome the potential barrier and the current from the semiconductor into the metal  $j_{s \rightarrow m}$  increases. The I-V characteristics in the forward direction is [82]:

$$j_{s \rightarrow m} = A^* T^2 \exp\left(\frac{e\Phi_{SB}}{kT}\right) \exp\left(\frac{eV}{kT}\right) = j_s \exp\left(\frac{eV}{kT}\right) \quad (3.7)$$





(a) Conduction band profile for different applied biases neglecting image force lowering. A positive bias voltage is called *forward*, a negative *reverse*. The dashed lines are the fermi levels for each bias voltage.

(b) Measured I-V characteristics for a MnGa-diode with a doping of  $4 \cdot 10^{17} \text{ cm}^{-3}$ . Data are from [84]

Figure 3.11: Overview of the MnGa/GaN diodes in the Schottky-Mott model.

Therefore, the total current  $j_{tot} = j_{s \rightarrow m} - j_{m \rightarrow s}$  is

$$j_{tot} = j_s \left( \exp\left(\frac{eV}{kT}\right) - 1 \right) \quad \text{Thermionic emission} \quad (3.8)$$

A measured I-V characteristic of a MnGa/GaN Schottky diode is shown in Figure 3.11 b). The inset shows a side view of the diode. An outer ring acts as an ohmic contact and the middle pad is the actual diode. In the forward direction, the barrier height can be extracted according to Equation 3.7. The barrier height  $\Phi_{SB}$  of various MnGa/GaN diodes with different contact areas is on average  $\Phi_{SB} \approx 0.69 \text{ eV}$  [84].

In most cases, the I-V curve differs slightly from Equation 3.8. To take other effects, e.g. image force lowering, into account, an *ideality factor*  $n$  is introduced. The forward current is then modified to:

$$j_{s \rightarrow m} = j_s \exp\left(\frac{eV}{nkT}\right) \quad (3.9)$$

$$n = 1 + \frac{\delta\Phi_{SB}}{\delta V} \quad (3.10)$$

Values for  $n$  are usually close to unity. For the measured diodes,  $n=1.15$  which shows that there is a deviation between the ideal model and our experimental Schottky diode. Reasons for the higher values of the ideality factor can

---

be inhomogeneities in the barrier height, which might arise from not ideal surfaces, or an increased tunneling current, which has been ignored so far.

### 3.3.4 Surface and interface states

Most of the studied metal/ semiconductor systems do not follow the Schottky-Mott rule (Equation 3.1). The Schottky-Mott model originates from the Metal-Metal contact that by definition differs from a metal/ semiconductor contact.

For the Si(111) surface, experiments showed that the Schottky barrier height for different metals does not change so much as one would expect from the work function of the corresponding metals [85]. This means, that the properties of the semiconductor play a larger role in the formation of the Schottky contact than the metal itself.

#### Surface states

To address this problem, the concept of surface states has been developed by Bardeen in 1947 [86]. According to Bardeen, localized states may exist inside the forbidden gap between the valence and the conduction band at the surface of a semiconductor. Following the mathematical description of H. Lüth, two solutions of the Hamiltonian in the nearly free electron model are possible [83]. In Figure 3.12 a), the solution for the bulk like states at the surface is shown. Inside the crystal the wavefunction forms standing Bloch waves that are matched to the exponential decaying part into the vacuum. This is not surprising, as the solution resembles the text book case of a wave hitting a potential barrier of magnitude  $V_0$  while the energy of the wave is smaller than the barrier,  $E < V_0$ .

An interesting new solution appears when also complex wave vectors are allowed. For a certain set of these wave vectors, the eigenvalues of  $E$  are real and a new type of solutions is possible. They are shown in Figure 3.12 b). The wavefunction is now localized at the surface of the crystal and decays into the vacuum *and* the crystal. The density of these surface states can be very high, in the order of  $10^{12}$ - $10^{13}$   $\text{cm}^{-2}$ . Therefore, for a complete description of the metal/ semiconductor contact they have to be taken into account explicitly.

The GaN(0001) surface has been studied extensively with photo emission experiments (X-ray photoelectron spectroscopy (XPS) and ultraviolet photoelectron spectroscopy (UPS)). With this technique, the local density of

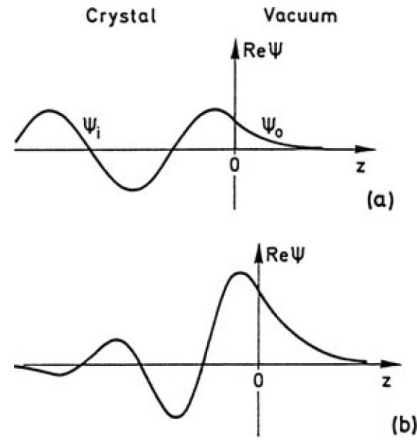


Figure 3.12: Real part of the one electron wave function for a) standing Bloch wave and b) surface state localized at the surface. Taken from [83].

states of the surface can be revealed.

Eller *et al.* present in a review paper the current research status concerning GaN and AlGaN surface states including a description of current leakage mechanisms in GaN/AlGaN based transistors [87].

A surface of a crystal has fewer bonds compared to the bulk. The chemical bonds have to be broken in order to form the surface. This formation costs energy, therefore the topmost atoms are rearranged. This reconstruction can be observed in RHEED experiments and depends strongly on the preparation of the surface, e.g. whether it is cleaved in UHV, annealed in a gaseous environment or plasma treated. In the following, the focus will be the Ga terminated GaN(0001) surface. This is the surface one obtains after MBE growth in the Ga rich regime on a GaN/Al<sub>2</sub>O<sub>3</sub> template.

Dhesi *et al.* performed angle resolved XPS on this surface [88]. A signal close the valence band maximum has been measured by the authors. The feature showed no strong dispersion in k-space, which according to their work is due to dangling bonds of sp<sub>z</sub> character at the surface.

Theoretical calculations on the character and position of surface states have been conducted by van der Walle *et al.* for (2x2) surface reconstructions [89]. Here, a state close to the middle of the band gap, around 1.5 eV above the valence band minimum can be found.

Himmerlich *et al.* characterized the (2x2) surface with different surface treatments by XPS experimentally and theoretically [90]. According to Himmerlich *et al.*, independent of the surface treatment, the Fermi level was *pinned* at 2.9-3.0 eV above the valence band maximum.

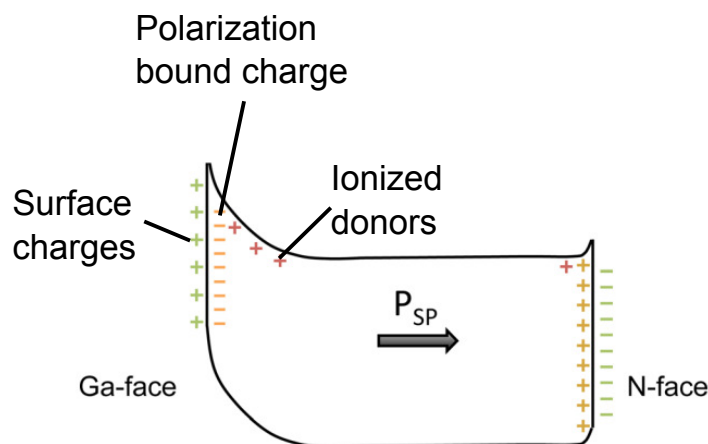


Figure 3.13: Experimental findings of the band bending in c-plane GaN due to surface states and spontaneous polarization. The barrier height for the Ga-polar surface is 1.1eV and 0.2 eV for the N-polar surface. Reprinted with permission from [87]. Copyright (2013), American Vacuum Society.

The obtained data do not agree very well. This shows, that a *real* GaN(0001) surface differs from an ideal surface. The growth process might be different or there are probably surface adatoms, oxides and vacancies present at the surface which have not been taken into account in the calculations explicitly. The picture is even more complicated: Polarization charges are present at the surface. GaN is a polar crystal and has a strong polarization field in the (0001) direction along the crystal. For the GaN(0001) surface, the polarization vector  $\vec{P}_{SP}$  points into the bulk, leaving negatively bound polarization charges at the surface behind. These charges are compensated by ionized donors and the surface states. Experimental data of the height of the band bending, including both surface states and polarization fields, report values of around 1-1.5 eV and 0.2 eV for Ga-face GaN(0001) and N-face GaN(000 $\bar{1}$ ), respectively [91](measured by surface potential electric force microscopy) [92] (measured by UPS). This band bending depletes the GaN layer depending on the doping by 50-100nm. This surface layer is therefore electrically inactive in transport measurements.

The complete picture of the surface band bending is shown in Figure 3.13 for Ga polar and N polar surfaces. Even without a metal, a barrier, similar to a Schottky barrier, is formed both on Ga-polar and N-polar faces.

### Metal induced gap states (MIGS)

The connection between surface states and interface states is straightforward. Surface states and/or interface states might pin the Fermi level due to the high density of states at the surface of the semiconductor. Bardeen did not know anything about interface states and he attributed the Fermi level pinning entirely to intrinsic surface states. Heine in 1965 came up with the model of metal induced gap states (MIGS) [93]. Heine saw the origin of these interface states is the overlap of the wavefunctions of metal and semiconductor. The wavefunctions of the metal extend into the semiconductor and form new states inside the band gap.

Heine calculated the energy of these states with respect to the metal deposited on top. He concluded that in most cases the position of these states is independent of the metal.

There is experimental proof for this assumption for a variety of metal/ semiconductor systems. Mattern-Klosson *et al.* deposited Sn on GaAs in a UHV environment and measured the band bending and therefore the Schottky barrier height with UPS [94]. They used the GaAs(110) surface which is a so called *flat* surface (no surface states present) and showed that 0.5 ML of metal coverage is enough to form the Schottky barrier. It is worth to mention that already after a coverage of 0.2 ML of metal the Schottky barrier height is almost at 75% of the final value.

To get a better understanding of the MnGa/ GaN system in terms of MIGS, P. Blöchl performed first principles calculations to explore the details of the atomic structure at the interface. MIGS play an essential role in spintronic devices because they introduce a spin dependent tunneling resistance when the MIGS itself are spin polarized (e.g. Fe/ GaAs [95]).

The starting point is the experimental finding that the MnGa(111) plane grows with a 30° rotation with respect to the underlying GaN(0001) surface (see section 3.2). The calculated model of the atomic arrangement of  $\text{Mn}_x\text{Ga}_{1-x}$  on GaN(0001) is shown in Figure 3.14 a).

It is found that the Ga atoms of  $\text{Mn}_x\text{Ga}_{1-x}$  favor the Ga-top positions of GaN, while the Mn-atoms favor having the Ga atoms in a bridge position. The energy landscape exhibits valleys separated by ridges of height 0.4 eV. The Ga-N distance at the interface is expanded by 10-15% compared to the bulk, which can be attributed to a charge transfer into the layer. According to the calculations, the MnGa/ GaN interface never shows an unrotated epitaxial relationship due to the large strain energy of 0.6 eV per unit cell for MnGa, which is too large to be sustained. This is in stark contrast to the experiment which indeed does show non rotated planes. This shows that

the computational model has to be improved to include all possible surface configurations.

In Figure 3.14 b), a sketch of a possible orbital picture of the interface is shown. The Ga s-like wavefunctions of GaN overlap with Mn d-orbitals. In the picture, the overlap is only between Ga and Mn d-orbitals of one spin type. Further calculations have to clarify what the exact picture of the interfacial band structure really is.

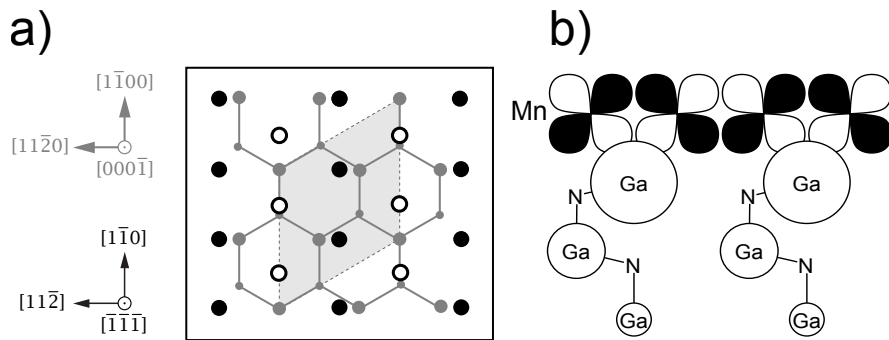


Figure 3.14: Model of the MnGa/ GaN interface according to the calculations performed by P. Blöchl. a) Two-dimensional unit cell (shaded area) of the atomic arrangement with minimal energy. The GaN layer at the interface is shown in grey with Ga atoms represented as large spheres and the subsurface N atoms represented as small spheres. Ga and Mn atoms of MnGa are represented by filled and open black spheres, respectively. b) Orbital scheme of the MIGS states at the Fermi level. Ga-s orbitals of GaN overlapping with the d-orbitals of MnGa of one spin type.

### 3.4 Transport processes through the MnGa/ GaN interface

In order to find the best conditions for spin injection, the MnGa/ GaN Schottky diodes have been characterized by means of electrical transport measurements. Unfortunately, the true picture is not as easy as the standard Schottky model. Figure 3.15 gives an overview of possible processes happening in *real* reversed biased Schottky diodes.

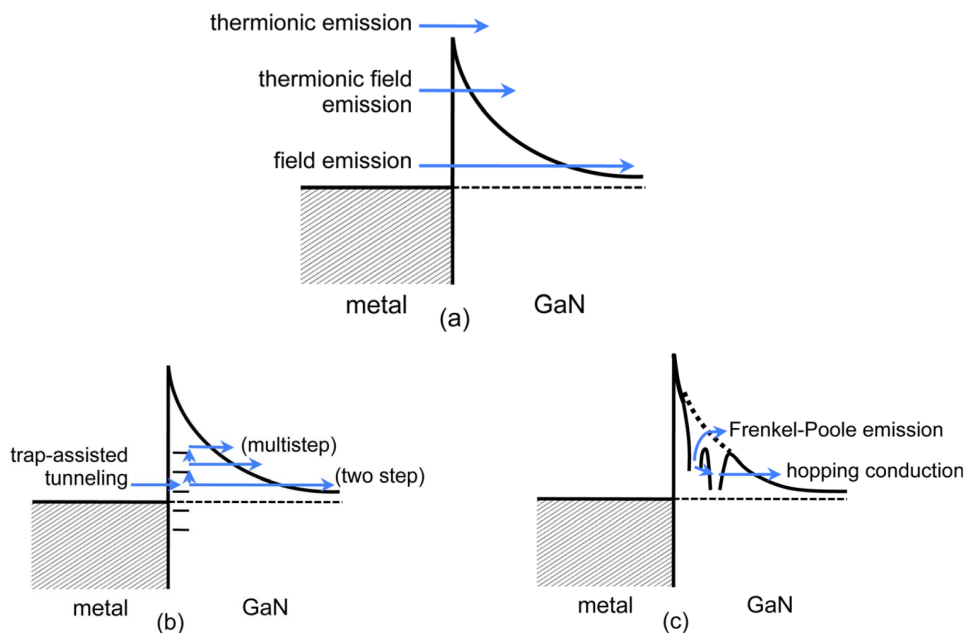


Figure 3.15: Overview of possible transport processes from the metal into the semiconductor in Schottky diodes. a) Tunneling through the barrier, b) Tunneling via traps (defects), c) hopping conduction through localized states and Poole-Frenkel emission. Reprinted with permission from [87]. Copyright (2013), American Vacuum Society.

Figure 3.15 a) shows the ideal transport process in reversed biased Schottky diodes. Depending on the temperature, cold ( $E \approx E_F$ , single step tunneling), or hot ( $E \gg E_F$ ) electrons tunnel through the barrier quantum mechanically and enter the conduction band.

Case b) and c) depict schematically other possible processes. They are closely related to each other and are not easy to distinguish. On the one hand, case b), there is trap-assisted tunneling via defects or hopping through localized

---

states. On the other hand, case c), it is possible to excite an electron from a captured state (e.g. defect) into the conduction band without tunneling (Poole-Frenkel emission). Zhang *et al.* investigated the leakage current of Ni/GaN Schottky diodes grown by MBE [96]. The leakage current is basically the current flowing in reverse direction of a diode. In GaN based devices the leakage current is larger than one would expect from the thermionic model and the understanding of current leakage mechanisms is still extensively debated in the nitride community.

Zhang *et al.* analyzed the I-V characteristics and temperature dependence of the diodes and found two distinct regimes. At temperatures below 150K tunneling dominates the reverse current. At higher temperatures the leakage current flow is dominated by Frenkel-Poole emission. According to the authors, traps near the metal/semiconductor interface emit electrons into a continuum of states. The authors specify the continuum states as conductive dislocations going from the surface into the bulk.

In the following, for the description of the transport process in MnGa/GaN diodes, trap-assisted tunneling processes have been excluded. This can be justified by the fact that the doping of our structures is higher than in the work by Zhang *et al.* and therefore tunneling becomes more pronounced than trap-assisted tunneling, especially at low temperatures where spin injection experiments are conducted. For spin injection purposes, the role of cases b) and c) are not clear. Every capturing or emission of electrons most likely reduces the spin polarization. No experimental data of the role of trap assisted tunneling in GaN based spintronic devices has been found.

To gain inside into the governing transport process, an ideal diode of MnGa on GaN is modeled in the following section. After the discussion of the calculated data, the experimental results are presented and a conclusion about the best injection conditions is drawn.



## Model of tunnel conductance

As a first approximation of the temperature dependence of the tunneling current the following model will be discussed.

Two electron reservoirs  $X$  and  $Y$  are separated by a barrier of height  $\Phi_B$  with a thickness according to Schottky's depletion width formula. The left electrode obeys the electron energy spectrum of a metal, whereas the right electrode the one for a n-type semiconductor. The density of states  $g(E)$  of the metal is approximated as a constant due to the small dispersion around  $E_F$  of the metal. The activation of shallow donors is taken into account but at the studied doping levels GaN is close to degeneracy or even degenerate. The Fermi level  $E_F$  is set to 0 eV for the metal and for the semiconductor according to the charge neutrality condition. This situation is sketched in Figure 3.16 without an applied bias at a finite temperature.

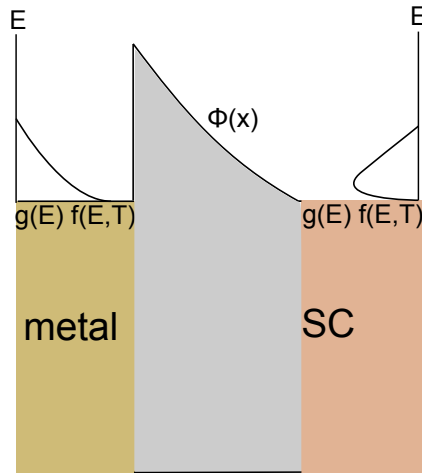


Figure 3.16: Sketch of the model system used in the simulation. Two reservoirs, metal and semiconductor are separated by a potential  $\Phi(x)$ . The tunnel current between the reservoirs can be expressed by *Fermi's Golden Rule* with the tunneling probability  $T$ , which is in our case the WKB approximation for the Schottky potential.

According to *Fermi's Golden Rule* the tunnel current in a non interacting system is given by:

$$j \propto \int dE n_{final} \cdot |T|^2 \cdot n_{initial} \quad (3.11)$$

where  $n_{initial} = g_X(E) \cdot f_X(E)$  is the number of occupied states of reservoir  $X$  at a given energy  $E$  in an interval  $[E, E+dE]$  and  $n_{final} = g_Y(E) \cdot (1 - f_Y(E))$  gives

---

the number of unoccupied states in the final reservoir Y in the same interval.  $f_{X/Y}(E)$  is the Fermi distribution.

The matrix element  $T(E)$  is the tunneling probability at a given energy  $E$ . The difference of the current from the metal to the semiconductor,  $j_{m \rightarrow s}$ , and from the SC to metal,  $j_{s \rightarrow m}$ , yields the total current:

$$j = j_{m \rightarrow s} - j_{s \rightarrow m} \\ \propto \int dE g_m(E) g_s(E - eV) |T(E)|^2 (f_m(E, T) - f_s(E - eV, T)) \quad (3.12)$$

The tunneling probability  $T$  can be approximated using the Wentzel-Kramers-Brillouin (WKB) approximation [97]:

$$T(E) = \exp \left( -2 \frac{\sqrt{2m^*}}{\hbar} \int_0^w dx \sqrt{V(x) - E} \right) \quad (3.13)$$

with the potential and barrier width from subsection 3.3.1

$$V(x) = V_B - \frac{eN_D^+}{\epsilon_s} \left( wx - \frac{1}{2}x^2 \right) \quad (3.14)$$

$$w = \left[ \frac{2\epsilon_s}{eN_D^+} \left( V_B - V_{ext} - \frac{kT}{e} \right) \right]^{1/2} \quad (3.15)$$

which is valid for  $E < \Phi_{SB}$ . For  $E > \Phi_{SB}$ , the transmission probability is 1. For the total current, Equation 3.12 has to be evaluated. In detail the following steps have been performed:

1. Calculation of the potential  $V(V_{ext}, N_d, x)$
2. Calculation of the transition probability  $|T(E)|^2$ .
3. Integration of Equation 3.12 for energies ranging from  $E_C$  up to  $e\Phi_{SB}$ .

A sample code can be found in the master thesis of David Disterheft [98]. The transition probability  $|T(E)|^2$  for zero bias and two different dopings is shown in Figure 3.17 a). In Figure 3.17 b), the product  $|T(E)|^2 [f_m(E, T) - f_s(E - eV, T)]$  is evaluated. This expression is basically the energy tunnel conductance spectrum. It shows the energy dependent tunnel probability for an electron with an energy  $E$  through the barrier. For spin injection purposes, a single step tunneling process is preferred. In contrast to other second order tunneling phenomena like thermionic field emission, the electrons do not have to relax to the conduction band edge. The probability

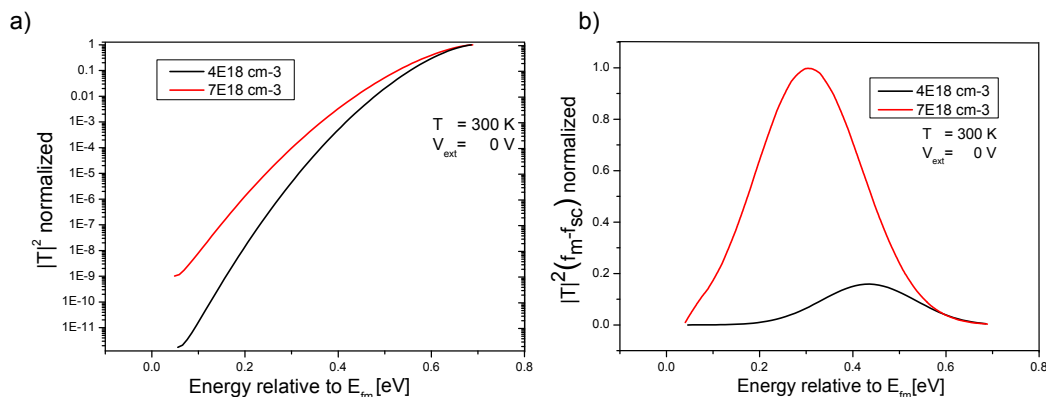


Figure 3.17: Calculations of the model system for tunneling transport in the WKB approximation. In a) the transition probability for two different dopings is shown. b) shows the product  $|T(E)|^2 f_L(E, T) - f_R(E - eV, T)$  normalized to the maximum transmission: It is the energy tunnel conductance spectrum. It evaluates what electron energies will contribute most to the total tunneling current.

that the spin property of the electron is conserved is higher due to missing possible scattering centers. The role of a spin filter effect due to a complex band structure in the material is neglected in this context.

From the calculations it can be concluded that a higher doping is needed to shift the transmission probability to lower energies and therefore increase single step tunneling processes. To avoid scattering with phonons the temperature in the experiment is usually lowered below 50K. This means that the transmission probability is reduced automatically because *hot* carriers, who can tunnel more easily, are abundant. In the experiment one has to decide between high *direct* tunneling current (high doping and therefore increased scattering at donors) and low tunneling current (high resistance, good for solving the conductivity mismatch), but less scattering.

The inverse of the integrated transmission probability for different dopings in dependence of the temperature is shown in Figure 3.18. This value can be accessed easily in the experiment by measuring the contact resistance which is inversely proportional to the transmission through the contact. Therefore, the temperature dependence of the contact resistance can be used as a measure for the governing transport process.

For lower dopings, electrons need to be excited thermally (thermionic field emission) in order to tunnel through the barrier or overcome the barrier (thermionic emission). This gives an exponentially increasing resistance with falling temperature. For higher dopings ( $n > 10^{19}\text{ cm}^{-3}$ ) single step tunneling

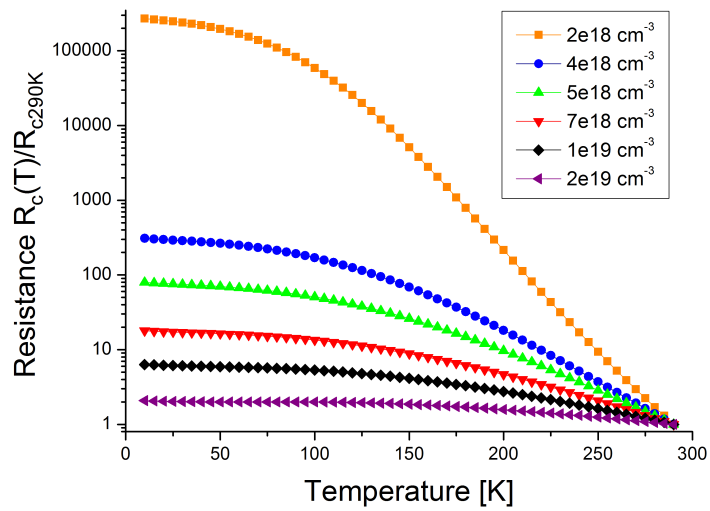


Figure 3.18: Simulated temperature dependence of the contact resistance  $R_C$  normalized to the room temperature value in the WKB approximation for different doping concentrations. At higher doping levels,  $n > 1 \cdot 10^{19} \text{ cm}^{-3}$ , the resistance at low temperatures is similar to the room temperature value which is an indicator for single step tunneling.

occurs which can be seen by a small change in resistance when the temperature is lowered. This is one of the Rowell criteria for tunneling (insulator like temperature dependence of the resistance) [99].

## 3.5 Experimental results

In order to find the best doping concentration for tunneling, a set of MnGa/GaN samples with varying doping concentrations are grown on GaN (500nm GaN:Si on non intentionally doped GaN templates). The samples are processed with  $\text{Mn}_x\text{Ga}_{1-x}$  as electrodes and the two point and four point resistances are measured with a Keithley SourceMeter in the configuration depicted in Figure 3.19.

The MnGa/GaN/MnGa structure consists of two diodes connected in series. One is operating in reverse direction, the other in forward. Therefore, the main contribution to the resistance comes from the reversed biased diode.

A switchbox changes the connections going to the sample. It is possible to measure two and four point resistances at approximately the same time. The measurements have been performed in a continuous-flow helium cryostat. For the determination of the contact resistance  $R_C$ , the resistance of GaN has been subtracted from the two point measurements. The resistance of GaN has been measured with a four point probe, which eliminates the contact and lead resistance.

The resistance has been obtained by fitting the I-V curve around zero bias (*zero bias resistance*). The advantage of this method is that in addition to the temperature dependence the I-V curve is recorded which can give insight in the transport process, too.

### 3.5.1 Sample preparation

The sample preparation has been conducted in the cleanroom. From a 1cm x 1cm wafer four 4mm x 4mm pieces are diced with a wafer saw. These pieces are then processed into transmission line (TML) structures. The layer structure of the first set of samples consisted of 100 nm thick  $\text{Mn}_x\text{Ga}_{1-x}$  grown on a Si doped GaN layer without an Al cap. The contact resistance of these structures is in all cases of the order of 100 k $\Omega$ . By adding more bond wires to the  $\text{Mn}_x\text{Ga}_{1-x}$  pad the resistance decreased continuously. In TEM pictures presented in subsection 3.2.2 a thick amorphous oxide layer could be

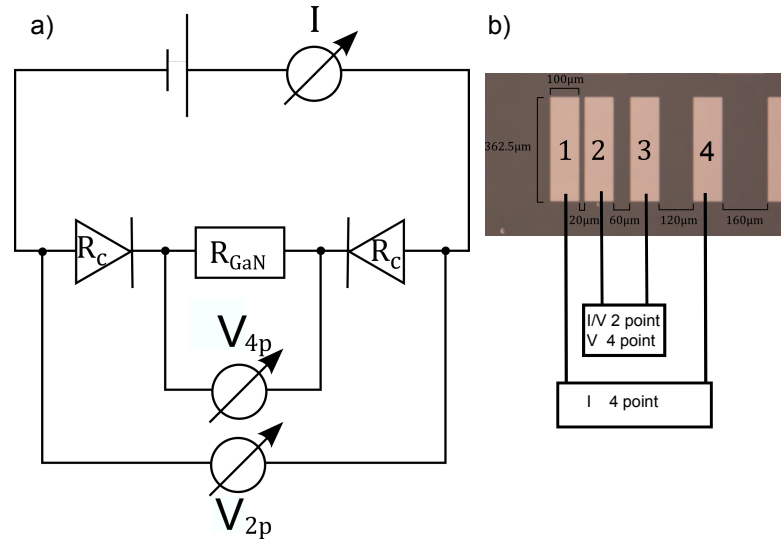


Figure 3.19: Setup for the measurement of the temperature dependence of the contact resistance. a) shows an equivalent circuit of the measurement and b) shows an optical microscope picture together with the wiring and the configuration used for the experiment (without mesa).

identified at the surface. Therefore, it is possible that the bonding process connected the metal layer underneath the oxide.

To circumvent this problem, a Al cap has been deposited on  $\text{Mn}_x\text{Ga}_{1-x}$  in the MBE chamber. With this Al cap, the contact resistance decreased depending on the doping to typical values of  $0.036\text{-}724\Omega\text{cm}^2 (\cong 0.1\text{-}20\text{k}\Omega$  in absolute values). A careful adjustment of the bonding parameters is needed. Otherwise it might happen that the film cracks and the Al wire connects directly the GaN surface. In this case, the current might flow directly from the Al wire into GaN.

Figure 3.20 sketches the preparation method. At the beginning, a positive photoresist (AR-P 3250 by ALLRESIST) has been used for the preparation of the pads. After exposing the spin coated wafer in a MJB4 Mask Aligner from SÜSS MicroTec to UV light, the development step in AR 300-26 developer removed the exposed parts of the resist and the Al capped  $\text{Mn}_x\text{Ga}_{1-x}$  surface reappeared for further treatment.

The wafer is then loaded in a vapor deposition machine (UNIVEX) from Leybold. First, the  $\text{AlO}_x$  on top and the Al has been removed in an Ar plasma. During this treatment step, a couple of nm of  $\text{Mn}_x\text{Ga}_{1-x}$  might be removed as well. After this cleaning step, a Au cap with a thickness of 10 nm is thermally evaporated on  $\text{Mn}_x\text{Ga}_{1-x}$ . The Au deposited on top reduces the

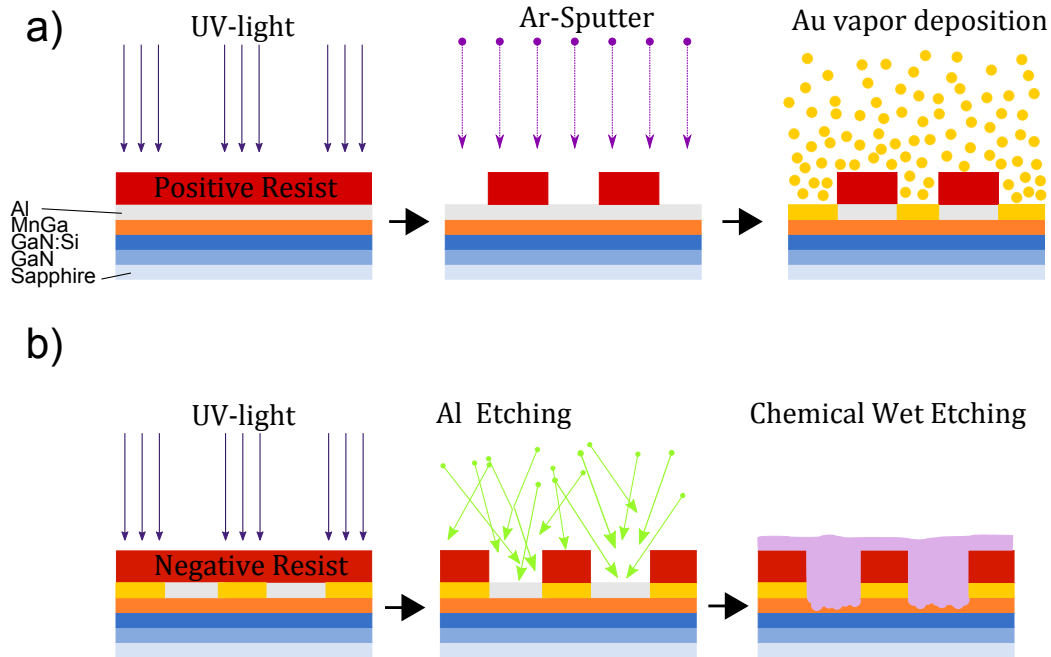


Figure 3.20: Processing steps for  $\text{Mn}_x\text{Ga}_{1-x}$  pad definition. See the text for details. From [98]

contact resistance of the top metal contact as oxidation of Au does not happen in contrast to Al. After the lift-off process in remover AR 300-70, the etch mask for  $\text{Mn}_x\text{Ga}_{1-x}$  wet etch has been structured with negative photoresist (AR-N 4340) as protection. The etch of  $\text{Mn}_x\text{Ga}_{1-x}$  is a two step process consisting of 1) Al removal by RIE or HCl wet etching and 2) wet etching of  $\text{Mn}_x\text{Ga}_{1-x}$  in a  $\text{H}_2\text{O}/\text{HCl}/\text{H}_2\text{O}_2$  solution. At the end, a mesa is defined with the wafer saw. The detailed parameters of all the processing steps can be found in the appendix.

### 3.5.2 Analysis

The measured I-V curves between two MnGa contacts for different dopings is shown in Figure 3.21 a). At a doping of roughly  $10^{19} \text{ cm}^{-3}$ , the I-V curve is linear, indicating an ohmic contact. This means that the tunnel barrier for electrons is very thin and single step tunneling is the dominant transport mechanism. A reduction of the doping leads to a typical *S-shaped* I-V curve. At small voltages, the resistance is high (current low) due to the fact, that electrons need to be excited thermally. At higher biases, the tunnel width decreases (subsection 3.3.1), therefore the tunnel probability increases, leading to a higher current.

In Figure 3.21 b), the normalized resistance to the room temperature value is shown. For higher dopings,  $n > 5 \cdot 10^{18} \text{ cm}^{-3}$ , the contact resistance increases only slowly with a reduction of the temperature .

The samples that were doped lower showed a strong increase in the contact

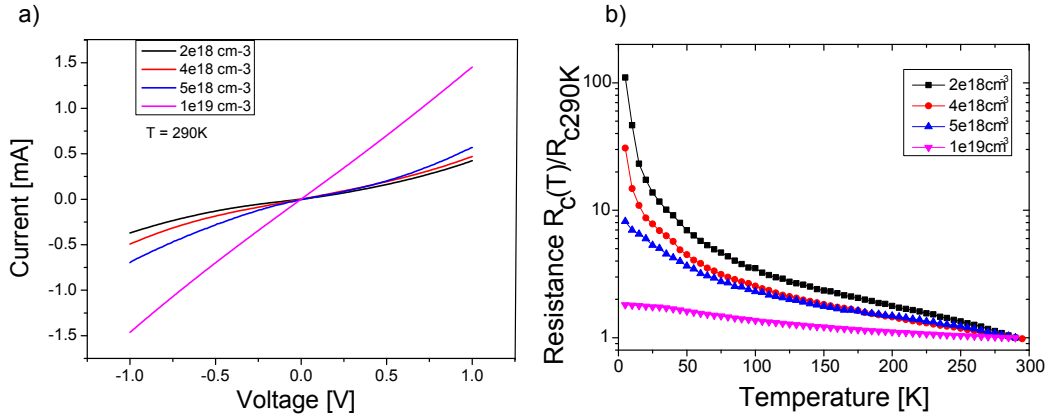


Figure 3.21: Measured a) IV-curves and b) temperature dependent contact resistances for different doping levels of GaN. An increase in the doping leads to a more linear shape of the I-V curve. The temperature dependence shows that for doping levels higher than  $5 \cdot 10^{18} \text{ cm}^{-3}$ , the increase in resistance with lowering temperature is small, which indicates single step tunneling.

resistance at temperatures below 50K. One explanation for this behavior is the already mentioned transition from single step tunneling to thermionic field emission. A second explanation might be the freeze-out of donors at low temperatures. At lower doping levels GaN is not degenerated and shows thermal activation of donors. Therefore, a lower number of ionized donors at low temperatures leads to an increase in the barrier width and a reduced tunnel current.



## Conclusion

In order to have a single step tunneling process, the doping should be higher than  $5 \cdot 10^{18} \text{ cm}^{-3}$ . To minimize possible spin scattering, a doping of  $7 \cdot 10^{18} \text{ cm}^{-3}$  in the spin injection experiments is chosen. This doping seems to be a good compromise between high direct tunneling current on the one side and structural quality and less scattering on the other.

In other material systems, where reversed biased Schottky diodes have been used for spin injection purposes, the doping profile is more complicated. In the Fe/GaAs system, Garlid *et al.* studied different doping profiles with respect to the electrical spin injection signal in the four terminal geometry [100]. The samples with the highest signal consisted of a transition region where the doping is changed from  $5 \cdot 10^{16} \text{ cm}^{-3}$  to  $5 \cdot 10^{18} \text{ cm}^{-3}$  within 15nm. Then, 15nm of  $5 \cdot 10^{18} \text{ cm}^{-3}$  doped GaAs is grown, followed by the ferromagnet.

In this case, the structures have been kept simple (no transition doping). If a spin related signal is observed, the doping profile can be optimized later on.



# Chapter 4

## Optical detection of spin injection

In this chapter, the detection mechanism based on optical selection rules is presented. A suitable approach is a vertical LED structure with a magnetic electrode which has been used quite frequently throughout the spintronics community (see chapter 2 for details). The distance between the electrode and the detection region, typically a quantum well, is of the order 50 nm. This shortens the way electrons have to travel and encounter scattering events. A second advantage is the easy sample preparation. There is no need for electron beam lithography and complicated etching and metallization steps. This saves time considerably. At the end, the complete sample preparation, including wiring was done in half a day.

Two different material systems have been studied. A well known  $\text{Co}_2\text{FeSi}/\text{GaAs}$  spin LED provided by the Paul Drude Institute (PDI) in Berlin and a set of  $\text{Mn}_x\text{Ga}_{1-x}/\text{GaN}$  based spin LEDs. The GaAs sample serves as a test for the complete setup. The known spin polarization is well above 10% at low temperatures and should be easily measurable with the setup.

### 4.1 Experimental setup

As shown in chapter 2, the optical proof of spin injection is a difference in left and right circular polarized emitted light. The detection scheme is rather simple. The emitted light passes through a  $\lambda/4$  plate and a linear polarizer. The  $\lambda/4$  plate changes the circular light to perpendicular linear polarized light which is then analyzed with a linear polarizer. After transmission of the the  $\lambda/4$  plate, Right handed circular polarized light is linear polarized  $+45^\circ$  and left handed circular polarized light is linear polarized  $-45^\circ$  with respect

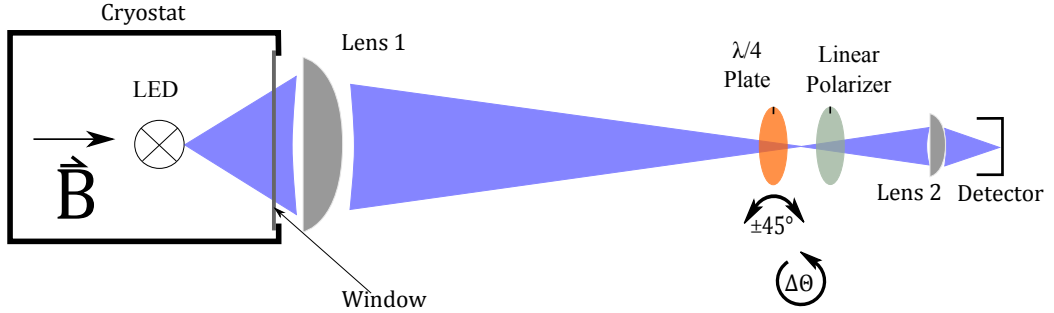


Figure 4.1: General setup for the measurement of spin injection. The optical components are placed close to an intermediate focus to gather all the light with the optics. In the experiment, the quarter wave plate is turned by  $\pm 45^\circ$ .

to the fast axis of the quarter wave plate. The following linear polarizer has to be placed with an angle of  $+45^\circ$  with respect to the fast axis in order to measure the intensity of right hand circular polarized light  $I(\sigma^+)$ . To measure the intensity of left handed circular polarized light  $I(\sigma^-)$ , the quarter wave plate has to be turned by  $90^\circ$  (or  $-45^\circ$  starting from the fast axis). The complete formalism can be found in Lars Watschke's master thesis [101]. Figure 4.1 shows the general setup. The optics have to be suitable for the wavelength emitted by the LED. Therefore, the quarter wave plate for the GaAs sample with a peak emission of  $\lambda \approx 800$  nm has to be changed to a plate with a retardation of  $0.25\lambda$  in the blue range (The used plate is specified for  $\lambda = 445$  nm). The peak wavelength of the spin LED with  $\text{Mn}_x\text{Ga}_{1-x}$  as an electrode is 430 nm. The error due to a chromatic quarter wave plate is approximately 1% [101]. The sample is glued into a chip carrier which is mounted on a sample holder with electrical connections. Two possible configurations are possible. First, the *Faraday* and second the *Quasi-Voigt* geometry. In the Faraday geometry, the light is collected in the direction of the external applied magnetic field (Top view). This means, that the light has to pass through the magnetic layer which can alter the light properties as well. In the *Quasi-Voigt* geometry, the light is collected to the side of the LED structure (Side view). Here, the magnetic field is applied parallel to the surface of the structure. The problems of both side and top view geometry will be discussed later on.

The used cryostat is a SM2000 system from the company Oxford. It consists of two separate systems. The magnetic system with a superconducting coil and a continuous flow cryostat where the sample is located. The magnetic field strength can be as high as 14 T at 2.2K. At liquid helium tempera-

tures, 12 T can be reached. In the following experiments, the maximum field strength was  $\leq 10$ T. The continuous flow cryostat allows to set the temperature between 4.2-300K. With pumping of the helium gas 2.2K can be reached. To get a more accurate temperature reading the current through the temperature sensor has been measured directly with a nanovoltmeter. To reduce the thermal load at low temperatures, the temperature sensing is automatically done in the four wire constant voltage mode: When the temperature is lowered, the resistance of the thermo sensor increases, the current is reduced automatically in order to get the same voltage drop.

The measurement itself is done with a lock-in measurement technique.

The light output of a LED is very sensitive to current changes. Therefore, it is important to sent a constant current through the LED. For the GaAs spin LED, the setup consists of a high precision function generator and a low noise AC current transformer (taken from the Hall Lab). The pulse signal of the function generator is transformed into an current by the current transformer. This works well up to supply voltages of 15 V. This is the limit of the AC current generator. The input of the lock-in is connected to a photodiode with a load resistor.

Unfortunately, the  $\text{Mn}_x\text{Ga}_{1-x}/\text{GaN}$  spin LEDs need higher supply voltages up to 100 V to get a good signal to noise ratio. The reason for this is the increase in resistance at lower temperatures of the GaN host material. Therefore, the supply for the  $\text{Mn}_x\text{Ga}_{1-x}/\text{GaN}$  LEDs is generated with a different method as depicted in Figure 4.2.

The current for the GaN LEDs comes from a high presision DC current supply (Keithley current source). This current is chopped electricly by an emitter circuit. Here, the function generator opens the gate of a transistor. The Emitter voltage of the transistor  $V_{\text{Out}}$  is connected to the LED. Voltages up to 150 V can be generated with this technique. The detector is a blue enhanced photo diode with a load resistor (0.1-1 M $\Omega$ ). The signal of the photodiode is again recorded with a lock-in amplifier. Grounding and noise in electrical circuits are serious issues. To avoid noise the instruments are connected to one common power line and the BNC cables are wrapped in aluminium foil. The common ground sets the reference voltage for all instruments ('single point ground'). This avoids ground loops between instruments due to different potentials. Different power plugs can have different grounds and depending on the instruments or machines connected to the line the noise level can be considerably high. The aluminium foil protects from electro magnetic interference and helps to keep down the noise level .

Furthermore, the instruments are positioned as far away from the magnetic coil as possible. At the end, the electronics for the generation of the pulse

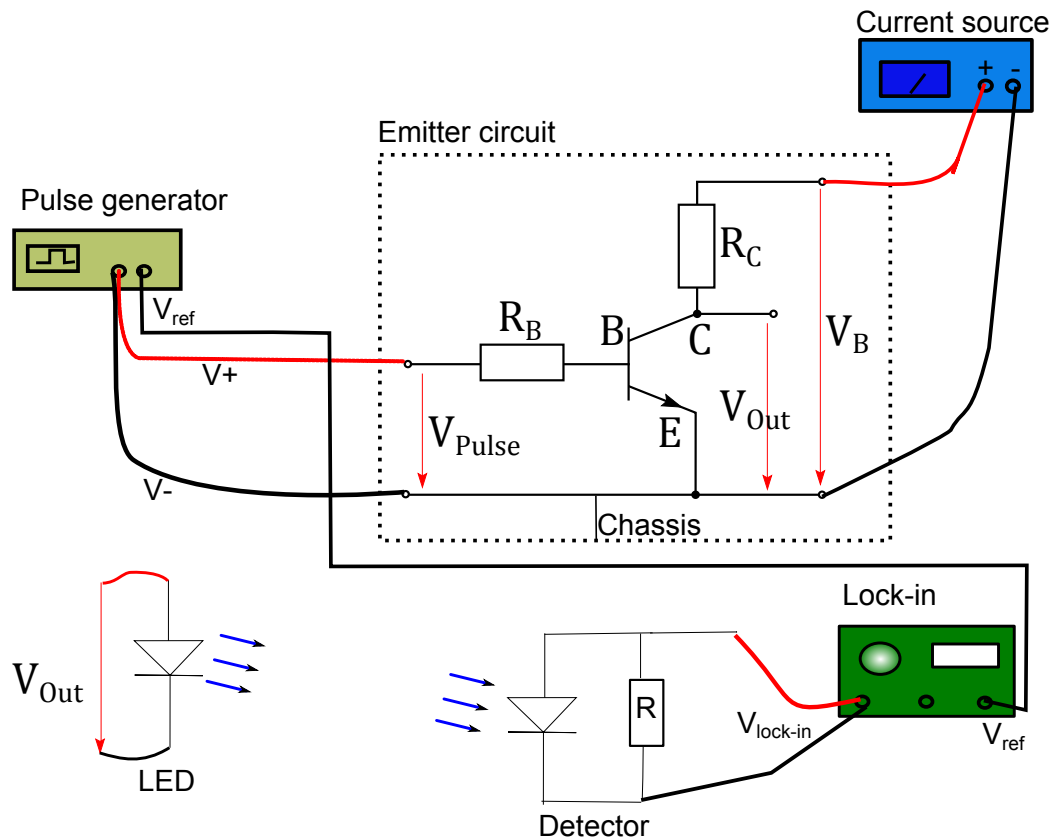


Figure 4.2: Wiring of the sample and the electronic components. The pulser opens the gate of a high power transistor. A current source provides the supply voltage. The detection circuit is spatially separated from the LED supply electronics. At higher magnetic fields, the electronics should be as far away from the magnet as possible.

(pulser, DC current source, emitter circuit) is spatially separated from the detection part (photo diode, lock-in).

An example of such a measurement is shown in Figure 4.3. After sufficient stabilization time for the temperature, the zero value of the intensity is recorded by covering the light path. (If the zero suppress knob of the lock-in has not be used, this step can be skipped.) First, the intensity for the quarter wave plate in  $+45^\circ$  position (relative to the linear polarizer) is recorded for approx. 45 seconds. Secondly, the quarter wave plate is turned by  $90^\circ$  to  $-45^\circ$  (The two positions were called *east* and *west* in the data files). To get more statistics the values for east and west are averaged over appropriate time intervals.

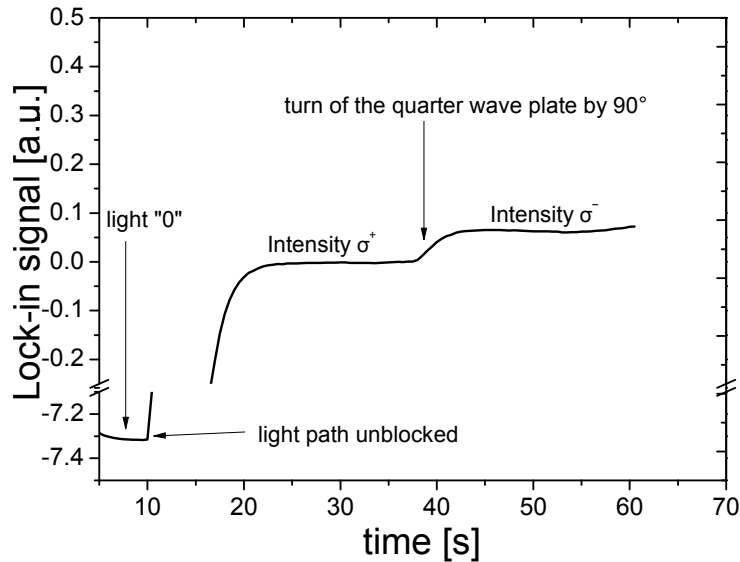


Figure 4.3: Sample measurement for the determination of the degree of circular polarization. The quarter wave plate is turned by  $90^\circ$  to change from right handed to left handed circular polarized light. Due to the large time constant of 1.25s, the change takes some time.

## 4.2 GaAs reference sample

The GaAs sample was provided by M. Ramsteiner from the PDI in Berlin and is similar to the one described by Ramsteiner *et al.* [46]. The structure of the LED is sketched in the inset of the recorded electro luminescence with a spectrometer in Figure 4.4. Starting from the bottom of the LED, the layer structure is the following : GaAs(001) substrate/ 400 nm p-GaAs ( $p=1\cdot 10^{17} \text{ cm}^{-3}$ )/ 200 nm p-Al<sub>0.1</sub>Ga<sub>0.9</sub>As ( $p=1\cdot 10^{16} \text{ cm}^{-3}$ )/ 50 nm of undoped material containing a 10 nm thick GaAs quantum well (QW) sandwiched between two 20 nm thick Al<sub>0.1</sub>Ga<sub>0.9</sub>As barriers/ 100 nm n-Al<sub>0.1</sub>Ga<sub>0.9</sub>As ( $n=1\cdot 10^{16} \text{ cm}^{-3}$ ) /15 nm n-Al<sub>0.1</sub>Ga<sub>0.9</sub>As linearly graded from  $n=1\cdot 10^{16}$ -  $1\cdot 10^{18} \text{ cm}^{-3}$  / 15-25 nm n-Al<sub>0.1</sub>Ga<sub>0.9</sub>As ( $n=5\cdot 10^{18} \text{ cm}^{-3}$ , tunnel barrier)/9 nm Co<sub>2</sub>FeSi (Ferromagnet).

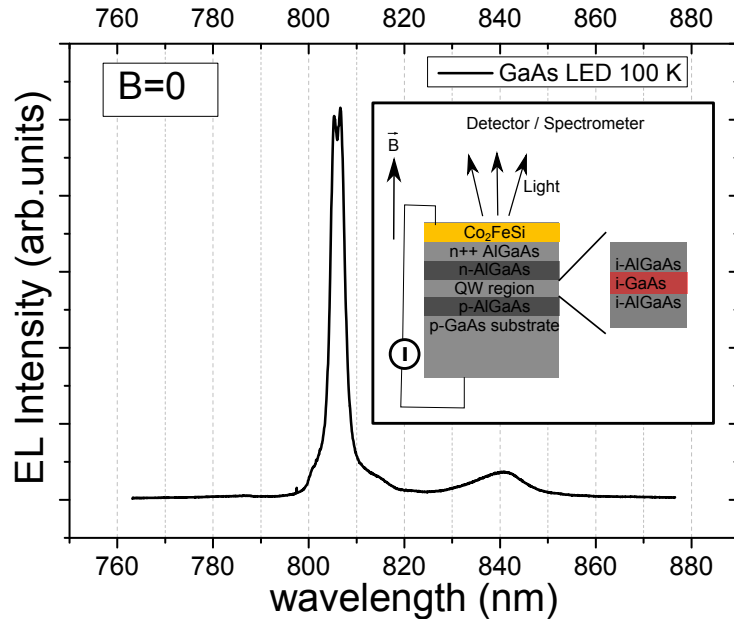


Figure 4.4: Electro-luminescence spectra of the GaAs test sample measured at 100 K. The inset shows the structure of the LED. The double peak is a signature of the lifted degeneracy of light and heavy hole transitions.

At a temperature of 12.5 K the degree of circular polarization  $\rho$  is measured in dependence of the applied magnetic field.

The result can be seen in Figure 4.5 a) and is the same as in the work by Ramsteiner *et al.* .

Two regions can be identified. At low fields up to 1.5 T,  $\rho$  follows the mag-



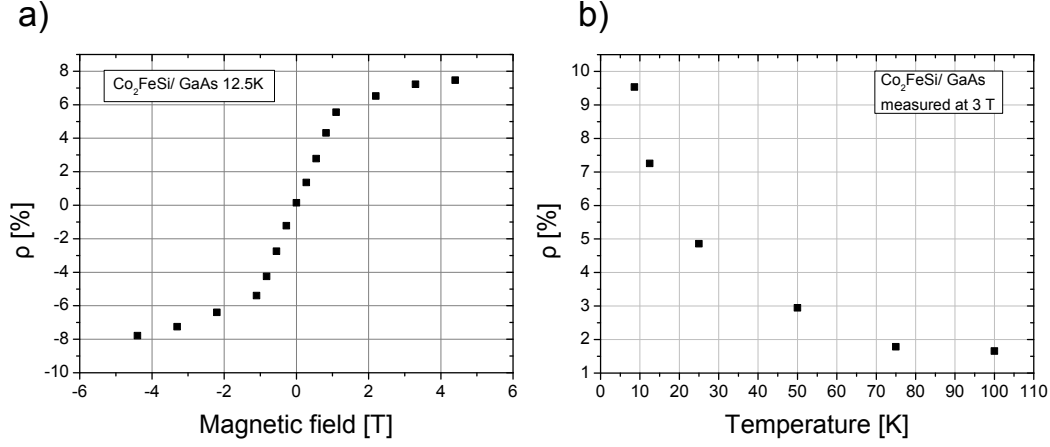


Figure 4.5: Results of the measurement on the GaAs LED test sample. a)  $\rho(B)$  for a temperature of 12.5 K. b) Temperature dependence of the saturation polarization with temperature.

netization of the ferromagnet, whereas at high fields, the magnet is saturated and  $\rho$  increases only slowly with increasing field. The maximum spin polarization is 8% at 4 T. According to different works on GaAs based spin LEDs, the sign of the small increase at higher fields depends on the active region used (InGaAs with different In concentrations) [15] [102]. In both mentioned publications, the slope is seen in non-magnetic test samples, too. According to the authors, it is due to a splitting of excitonic energy levels in magnetic fields (Zeeman effect). Ramsteiner *et al.* attributed different spin relaxation times and g-factors in the QW to different slopes of the Zeeman effect [102].

In Figure 4.6, the data of the mentioned publications is shown. The first spin-LED has In<sub>0.2</sub>Ga<sub>0.8</sub>As as the QW region and the second In<sub>0.1</sub>Ga<sub>0.9</sub>As, both have the same layer stacking (two 4nm InGaAs layers with a 10nm i-GaAs spacer sandwiched between 50nm i-GaAs layers). A first order approximation for the magnetic field dependence of the luminescence is the simple assumption that the energy levels show a Zeeman effect:

$$H_{\text{Zeeman}} = \frac{e}{m^*} \vec{L} \cdot \vec{B} = \vec{\mu} \cdot \vec{B} \quad \text{with} \quad \vec{\mu} = \frac{e}{m^*} \vec{L} \quad (4.1)$$

The validity of this model has been assumed by Snelling *et al.* for GaAs/ AlGaAs based QWs [103]. Following this treatment, the Zeeman energy for the exciton is:

$$E_{\text{Zeeman}} = g_{ex} \cdot \mu_B \cdot B \quad \text{with} \quad g_{ex} = g_e + g_{hh} \quad (4.2)$$

where  $g_{e/hh}$  denote the g-factor of electrons/heavy holes, respectively and  $\mu_B$  is the Bohr magnetron. Typical values for the Zeeman energy splitting for

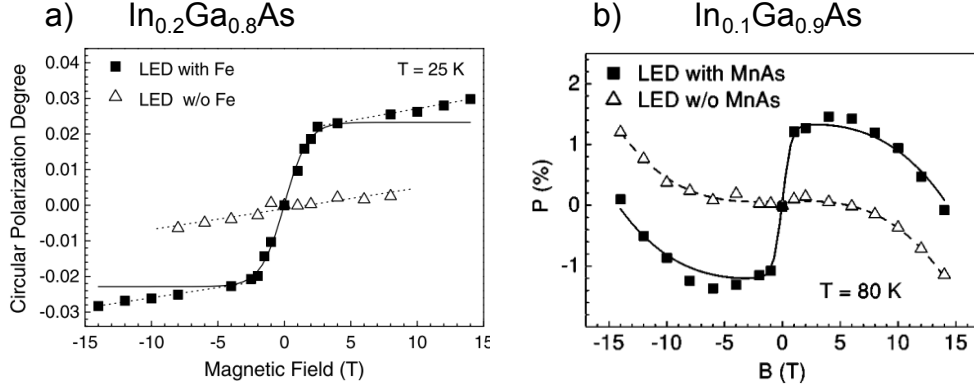


Figure 4.6: Degree of circular polarization for a) Fe/ GaAs with In<sub>0.2</sub>Ga<sub>0.8</sub>As and b) MnAs/ GaAs with In<sub>0.1</sub>Ga<sub>0.9</sub>As. The samples show different Zeeman effects depending on the alloy composition of the QW. Reprinted figures with permission from [15] and [102]. Copyright (2001, 2002) by the American Physical Society.

a magnetic field strength of 5 Tesla are of the order of  $E_Z = g_{ex} \cdot \mu_B \cdot B \approx 0.5\text{-}1$  meV. This is a very small value in comparison to the binding energy of the exciton of the order of 10 meV which shows that other effects might be responsible to explain the splitting of the  $\sigma^{+/-}$  transitions. One candidate is the Landau level splitting of the QW energy levels in a magnetic field. The energy scale in this case is:

$$E_{j,\text{Landau}} = \left(j + \frac{1}{2}\right)\hbar\omega_c \quad (4.3)$$

where  $\omega_c$  is the cyclotron frequency  $\omega_c = \frac{eB}{m^*}$  and  $j$  the Landau level number. With an effective mass  $m^*$  for the heavy hole exciton of  $0.045m_0$  (depending on the well width and In concentration) [104], the harmonic oscillator type energy is  $E_{0,\text{Landau}} \approx 6\text{meV}$  (at 5 Tesla) for the 1st Landau level. This seems on the right energy scale but the corresponding Hamiltonian:

$$H_{\text{Landau}} = \frac{p_x^2}{2m^*} + \frac{1}{2}m^*\omega_c^2 \left(x - \frac{\hbar k_y}{m^*\omega_c}\right)^2 \quad (4.4)$$

is not dependent on the angular momentum  $L$ . Thus, it acts only on the Landau level itself and not on different spin states of excitons. Therefore, only the Zeeman effect can explain the splitting of  $\sigma^{+/-}$  transitions.

Unfortunately, this simple model cannot explain the magnetic field dependence of the circular polarization in Figure 4.6 b), which shows an *S-shaped*

curve. In order to understand the magnetic field dependence in more detail, a closer look of excitons in QWs is needed. In the work of Viña *et al.*, GaAs/AlAs QWs in the absence of a magnetic field were examined [105], Figure 4.7. They conducted time resolved photoluminescence spectroscopy and found that for high exciton densities inside the QW a splitting of the  $\sigma^{+/-}$  emission only for HH excitons takes place. The splitting can be as large as 50% of the binding energy. The authors attribute this behaviour to an increased exciton-exciton interaction inside the QW at higher carrier densities.

Theoretical works by Yang *et al.* [106] and Bauer *et al.* [107] examined theoretically excitons in GaAs/AlGaAs quantum wells in magnetic fields. The intermixing of valance band states had been taken into account explicitly. In Figure 4.8 a) the calculated Zeeman spin splitting is shown for a GaAs/AlGaAs QW. It can be seen that the effect for heavy holes is indeed very small, of the order of 1meV. In Figure 4.8 b), the calculated exciton energy in dependence of the magnetic field is shown. The calculation reproduce the experimental data by Ossau *et al.* reasonably well [108]. This shows that the simple picture of non interacting excitons is only valid for low carrier densities. In magnetic fields the interaction between excitons depends strongly on the barrier width and the exciton's Bohr radius [109].

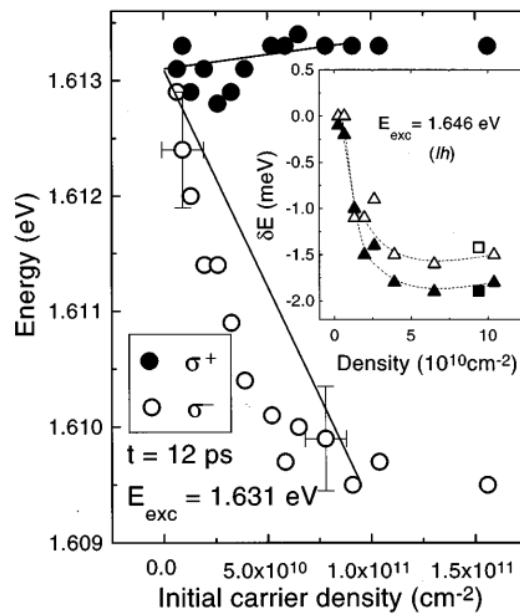


Figure 4.7: Exciton-Exciton interaction and spin splitting: Energies of the  $\sigma^{+/-}$  luminescence as a function of carrier density for HH excitons (for LH excitons in the inset). Reprinted figure with permission from [105]. Copyright (1996) by the American Physical Society.

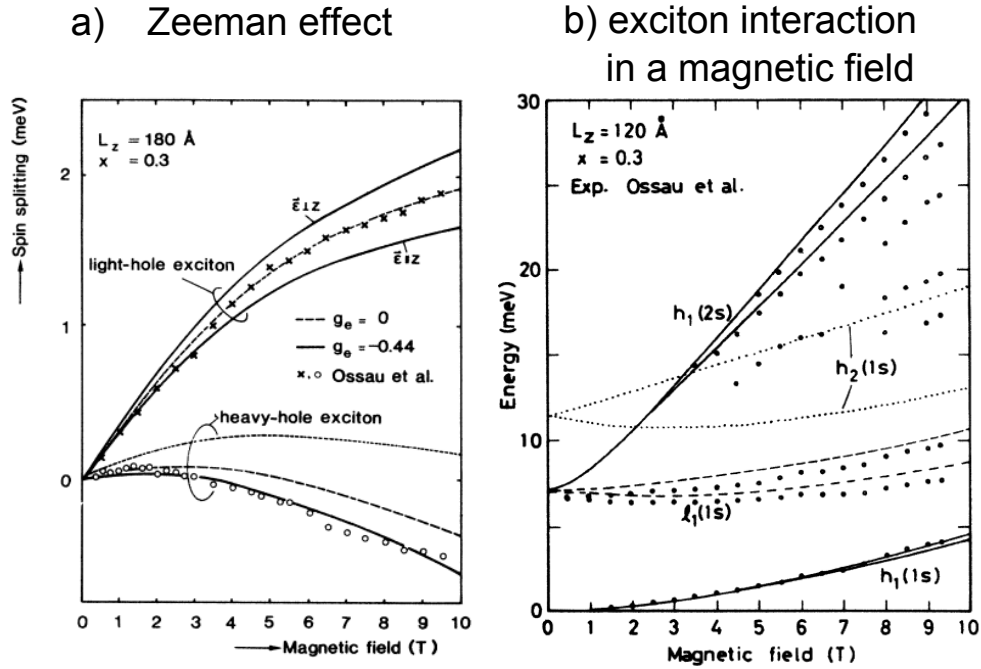


Figure 4.8: Explanation of optical polarization effects in magnetic fields: a) Spin splitting of heavy- and light-hole excitons of a GaAs/Ga<sub>0.7</sub>Al<sub>0.3</sub>As quantum well of 18nm. The dashed lines illustrate the effect of neglecting the electron g factor. Results for light-hole electrons are given for field polarization in the plane and normal to the plane of the well. b) Calculated magnetic field dependence of the spectral line exciton energies of a GaAs/Ga<sub>0.1</sub>Al<sub>0.3</sub>As quantum well of 12 nm width. Labels denote the predominant exciton character. (e.g.  $h_i(1s)$  is the 1s exciton derived from the  $i$ -th heavy hole subband). Dots represent experimental data in both cases by Ossau *et al.* [108]. Fig. a) and b) reprinted Figure with permission from [107]. Copyright (1988) by the American Physical Society.

## Spin relaxation in GaAs

In a second experiment, the temperature dependence of the spin polarization is measured. Here, the magnetic field is fixed at a saturated value of the ferromagnet and the polarization is recorded, Figure 4.5 b). The data shows that the polarization decreases quite rapidly with increasing temperature. Above 100 K,  $\rho$  drops below 1.5%. Therefore, a low temperature measurement is needed in order to observe the high spin polarization inside the GaAs QW.

In the GaAs system, the spin relaxation channels are well understood. In n-type material, two mechanisms dominate. The *D'yakonov-Perel*(DP) and the *Ellit-Yafet*(EY) mechanism [110] [52].

First of all, spin and momentum scattering have to be treated separately. In semiconductors, the spin lifetime can be larger than the corresponding average electron scattering time [52]. Therefore, during electron scattering events the spin can be conserved.

The DP mechanism can appear in semiconductors which do not have a center of inversion. The EY relaxation can occur in semiconductors with or without a center of inversion.

A theoretical work by Song *et al.* showed that the DP mechanism dominates the relaxation process in GaAs [110]. This is proven experimentally in n-type GaAs with dopings above  $2 \cdot 10^{16} \text{ cm}^{-3}$  (Metal-insulator transition)[111], Figure 4.9.

The DP mechanism is closely related to the *spin-orbit coupling* of conduction electrons with internal electric fields. An electron which travels through the host crystal feels the internal electric fields as induced magnetic fields. This intrinsic magnetic field  $\vec{B}_{\text{int}}(\vec{k})$  is dependent on the wave vector  $\vec{k}$  of the electron. Electrons with different  $\vec{k}$  vectors will therefore precess with different Larmor frequencies around  $\vec{B}_{\text{int}}(\vec{k})$ . This leads to a de-phasing of spins.

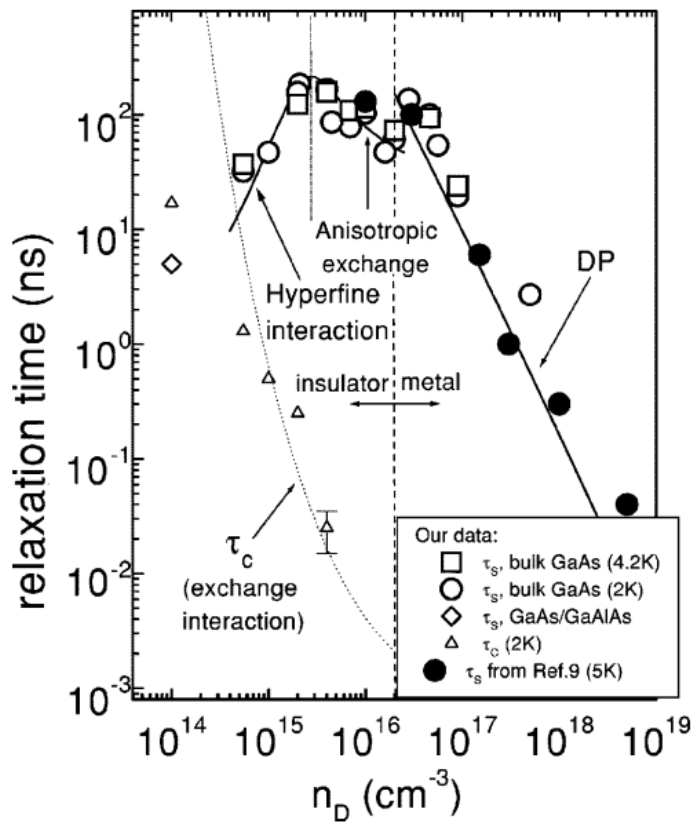


Figure 4.9: Spin relaxation time as a function of donor concentration. The longest spin lifetime is around the metal insulator transition. Reprinted figure with permission from [111]. Copyright (2002) by the American Physical Society.

### 4.3 MnGa/GaN LED structure and sample preparation

The LED structures used in the experiments are MOCVD grown by the group of Prof Dr. Mishra from the University of Santa Barbara (UCSB) because the GENII machine is not able to grow p-doped (with Mg) material at the moment.

The structure is kept rather simple, with a p-GaN layer at the bottom. The growth of Mg-doped GaN is still challenging and in a conventional LED p-GaN is grown at the end to minimize roughening of the layer.

The measured AFM roughness of the MOCVD grown LED is 1.6 nm for a scan area of  $5 \times 5 \mu\text{m}^2$ . The dislocation density is of the order of  $10^9 \text{ cm}^{-2}$ . The LED needed to have the n-doped layer at the top because spin polarized electrons should be injected. A growth of the LED structure on  $\text{Mn}_x\text{Ga}_{1-x}$  is not possible due to the low melting point of  $\text{Mn}_x\text{Ga}_{1-x}$  of approx.  $500^\circ\text{C}$ . In Göttingen, a Si-doped GaN tunnel barrier and  $\text{Mn}_x\text{Ga}_{1-x}$  capped with Al is grown in the MBE machine. An overview of the structures is given in Figure 4.10 together with an AFM picture of the LED before MBE growth.

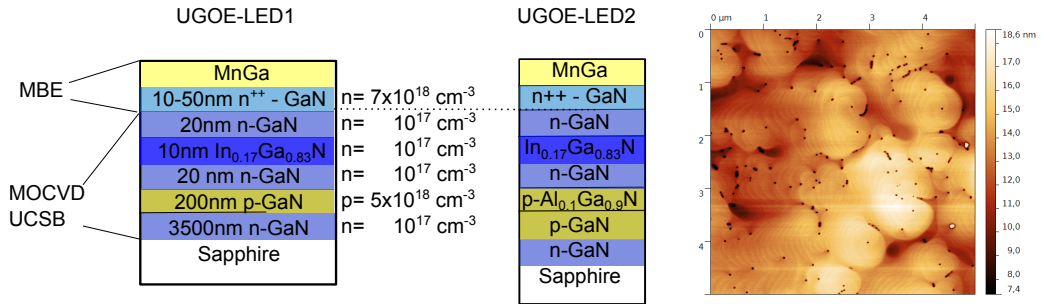


Figure 4.10: Overview of the LEDs grown by MOCVD (UCSB) and the added tunnel barrier and ferromagnet  $\text{Mn}_x\text{Ga}_{1-x}$  by MBE. The difference between UGOE-LED1 and UGOE-LED2 is the added electron blocking layer (20nm p- $\text{Al}_{0.1}\text{Ga}_{0.9}\text{N}$  with  $p=5 \cdot 10^{18} \text{ cm}^{-3}$ ) for better efficiency (drawing not to scale). The right picture shows an AFM scan of the MOCVD grown LED right before MBE growth.

For test purposes, the complete LED structure is etched down to the 200 nm p-GaN layer and the carrier concentration and mobility is measured in the van der Pauw geometry. The measured Hall constant is negative and an Arrhenius plot of the carrier concentration over temperature shows typical



activation energies for n-type impurities (not shown here). The negative Hall constant is expected in a two carrier model of electrons and holes due to the low mobility  $\mu_h$  of holes.

$$R_H = \frac{p\mu_h^2 - n\mu_e^2}{e(p\mu_h + n\mu_e)^2} \quad (4.5)$$

A p-type GaN layer has mobilities of the order of  $10 \text{ cm}^2/\text{Vs}$  [17] in contrast to an n-type layer with  $\mu_e=250\text{-}1000 \text{ cm}^2/\text{Vs}$ .

Therefore, the sign of the Hall constant can not be used in the determination of the majority carrier type. As seen by the mobility data depicted in Figure 4.11, the mobility values are typical for unintentionally doped GaN. This means, that all the current goes through the  $3.5\mu\text{m}$  thick unintentionally doped layer beneath p-GaN. This can be explained by the fact that the mobility and conductivity of p-GaN is orders of magnitude lower than in n-type GaN. Furthermore, the surface depletion, discussed in subsection 3.3.4, reduces the effective thickness of the p-GaN layer additionally.

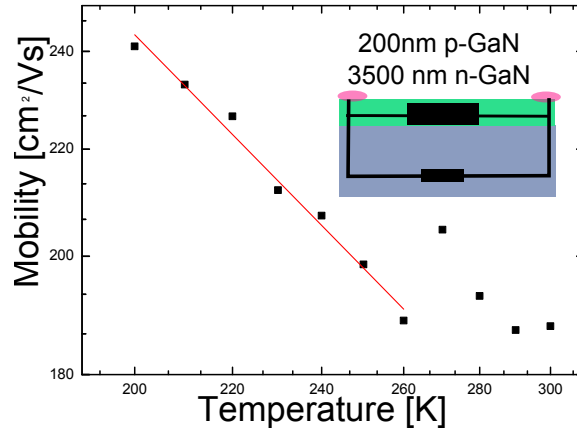


Figure 4.11: Mobility curve for 200nm p-GaN on  $3.5\mu\text{m}$  n-GaN. The data suggest that the current goes through the n-type layer as depicted in the schematic inset. The hall measurement shows n-type conductivity with typical activation energies for unintentionally doped GaN (not shown).

The preparation for the first side view LEDs is similar to the electrical measurements.

With optical lithography, a  $\text{Mn}_x\text{Ga}_{1-x}$  pad is structured. The Al cap of this pad is removed (Ar sputtering) and Au is evaporated. After removal of the photoresist, a dilute solution of  $\text{H}_2\text{O}_2:\text{HCl}$  is used to etch the  $\text{Mn}_x\text{Ga}_{1-x}$  except the Au capped pad.

The new process step is the etch down to the p-GaN layer and the contact formation on p-GaN with Au/ Ni (Ni first). No annealing step has been performed because this would destroy  $\text{Mn}_x\text{Ga}_{1-x}$  due to the high temperatures ( $\geq 600^\circ\text{C}$ ) during ohmic contact formation.

There is no data that says whether the etched surface is still p-type. Test measurements on other etched p-GaN layers were highly resistive. It could be that the surface changes to n-type conductivity or is compensated due to the removal of nitrogen which acts as a donor. It was tried to avoid this by using a low power RIE recipe with no argon gas. No other checks on the influence of the etching on the surface properties have been done. Maybe other metals work as well as ohmic contacts on etched GaN.

For the top view LEDs, the structuring is shortened by skipping the wet etch at the beginning. One part of the 4x4 mm piece is covered with a glass plate and etched in a chlorine based plasma down to the p-GaN. No Au cover is added to the  $\text{Mn}_x\text{Ga}_{1-x}$  layer (The Al cap does not need to be removed). On the etched p-GaN, Au/ Ni pads are evaporated through a shadow mask. Since there are no lithography steps, one sample is finished within two hours. The bonding is performed directly on the  $\text{Mn}_x\text{Ga}_{1-x}$  pad with Al bond wire. The details and process parameters can be found in the appendix. A sketch of the LED can be seen in Figure 4.12.

The electro luminescence spectra of the investigated diodes together with the I-V curves is shown in Figure 4.13. The peak wavelength is around 420-430 nm. Surprisingly, the LEDs with the EBL show a strong yellow luminescence. A yellow luminescence around 540-560 nm is usually attributed to defect related transitions [112].

The blue emission is not homogeneously distributed over the hole MnGa pad. Most of the light comes from the part that is closer to the p-contact. Therefore, it is not straightforward to normalize the current to a current density by the area of the active region. If one assumes an active area of  $2 \times 1 \text{ mm}^2$  (approx. half the  $\text{Mn}_x\text{Ga}_{1-x}$  pad) the current density  $J$  at 7.5 V is  $0.05 \text{ A/cm}^2$  and at 20 V is  $3 \text{ A/cm}^2$  which is very low compared to standard LEDs ( $J=10-50 \text{ A/cm}^2$ ).

Another import aspect is the luminosity. At room temperature, the LEDs are not very bright. A cooling down to 100 K increases the light output considerably which can be seen by the dependence of the luminosity on temperature in Figure 4.14.

A further reduction below 100 K does not increase the light output further. As a result of the high resistance at low temperatures, the applied voltage

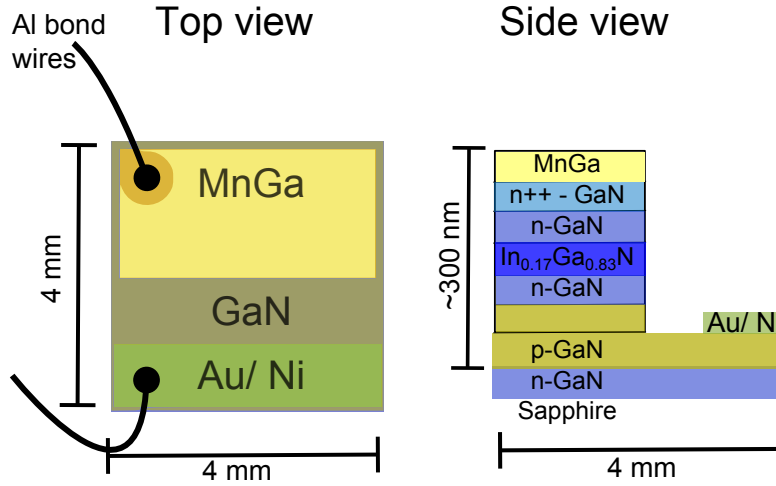


Figure 4.12: Sketch of the processed LED. One part of the wafer is covered with MnGa. On the etched p-GaN, Au/ Ni contacts are formed by a shadow mask.

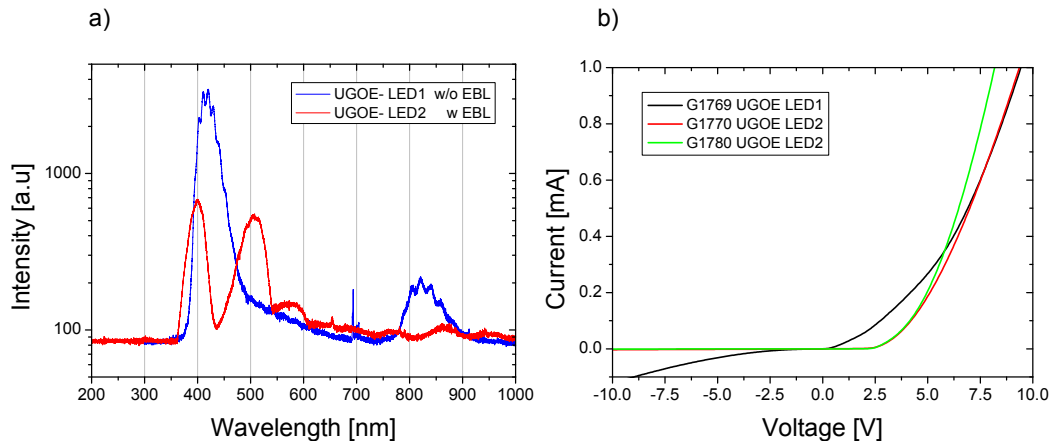


Figure 4.13: Electro optical characterization of the custom built spin LEDs. a) Electro luminescence at 150 K and b) I-V curves at room temperature. The oscillations in the blue spectra stem from interference effects with the GaN/Sapphire interface (Fabry-Perot effect).

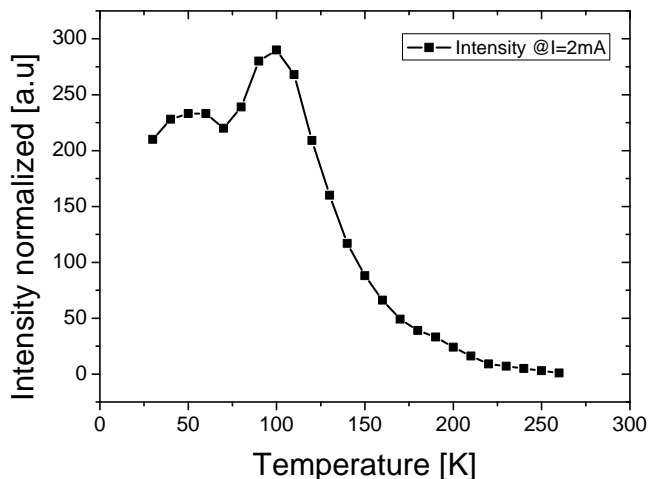


Figure 4.14: Temperature behaviour of the SpinLED UGOE-LED1 for a constant current normalized to the light output at 260 K. Starting from 260 K, reducing the temperature increases the intensity. Around 100 K, the maximum is reached.

for a constant current can be larger than 100 V. Because most of the voltage does not drop over the LED region but the lateral connection path on the wafer, a temperature increase of around 0.2 K can be observed when the power of the LED is turned on (heating). A couple of LEDs did not *survive* the low temperature operation. Therefore, as a protection, the maximum applied voltage was limited later to 40 V. With this limit, no degradation of the light intensity during one measurement cycle is observed.

## 4.4 Spin injection from MnGa into GaN

### 4.4.1 Side view

The first measurements are performed in side-view geometry with an approx. 30 nm  $\text{Mn}_x\text{Ga}_{1-x}$  pad. In this geometry, the LED light is slightly linear polarized due to waveguiding effects [113]. This means that the optics have to be corrected for the Faraday rotation every time the magnetic field is swept. Another problem is the poor light output of the LED in side view geometry, the maximum used sensitivity range of the lock-in was 100  $\mu\text{V}$ . The noise level

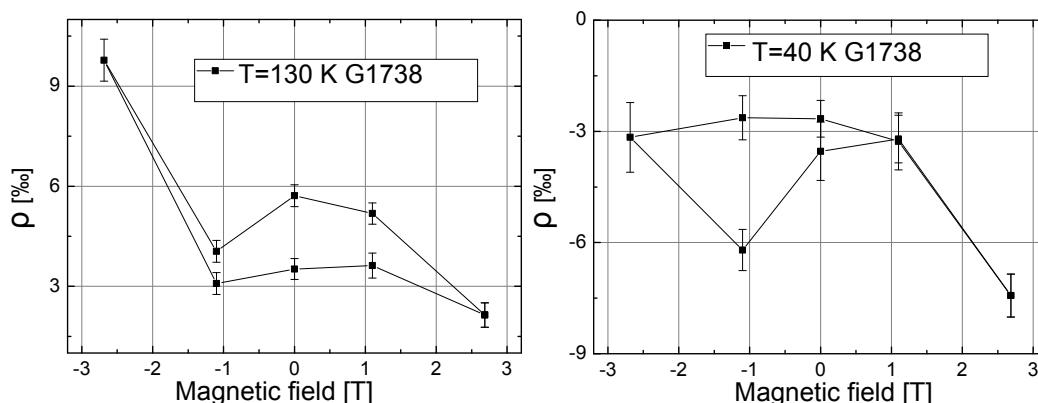


Figure 4.15: Results for sample G1738 in side view for two different temperatures. No clear spin injection signal can be seen.

is 200 nV (RMS) at an applied bias of 40 V. For comparison: the *Johnson-Nyquist* noise of a 100K $\Omega$  resistor (approx. resistance of the LED and the load resistor) at 100 K is 20nV (Bandwidth=0.8 Hz=1/Timeconstant). This means that the setup is not operating at the physical limit and there is room for improvement. But the setup is capable of measuring polarization values down to the promille range easily.

The temperature control was problematic at the beginning. The light output of the diode is very sensitive to temperature fluctuations. Before the measurement can begin, a 'cool in' time of 30-60 min is needed.

From the results shown in Figure 4.15 for sample G1738 (40 nm MnGa/25 nm  $n^{++}$ -GaN with  $n=7 \cdot 10^{18} \text{ cm}^{-3}$ / UGOE LED1) **no reliable spin injection signal can be observed**. The diode did not survive the operation at 40 K due to the excessive heating of the diode (applied bias  $\approx 100$  V). A non magnetic test diode (G1693) did not show any effect. In the data at 130K, an hysteresis of 0.3% at zero magnetic field can be seen. The origin is not clear. The data could not be reproduced at lower temperatures.

#### 4.4.2 Top view

The change from side to top view increased the light output by a factor of 30. In order to reduce absorption in the ferromagnetic layer, the thickness of  $\text{Mn}_x\text{Ga}_{1-x}$  was approx. 3 nm in contrast to the thickness in side view geometry of 30-40 nm.

Another benefit of the top view geometry was the missing linear polarization of the light. Therefore, no Faraday effect was observable and a readjustment

of the optics every time the magnetic field was changed was obsolete. As a result of the missing linear component of the emitted light, a magneto optical Kerr effect of the  $\text{Mn}_x\text{Ga}_{1-x}$  layer when the light passes through can be excluded.

To distinguish between magnetic and intrinsic contributions, a non magnetic test sample is investigated, too. The used metal is Al and is evaporated in the MBE machine instead of  $\text{Mn}_x\text{Ga}_{1-x}$ .

The data of this sample, G1780 (Al/ 25 nm  $n^{++}$ -GaN with  $n=7 \cdot 10^{18} \text{ cm}^{-3}$ / UGOE LED2), is shown in Figure 4.16. When a magnetic field is applied, a circular polarization can be observed without a magnetic layer at all. This is the same Zeeman effect similar to the GaAs spin LEDs in section 4.2. In a recent paper about magneto excitons in c-plane GaN QWs Bardyszewski *et al.* concluded that valence band mixing due to the quantum well confinement can explain different slopes and shapes of the magnetic field dependence of the  $\sigma^{+/-}$  transitions [114].

At 4T, the polarization is -0.6%, it increases linearly with the applied field and can be high as -1.5% at 10T. From the negative slope it can be concluded that the intensity of the  $\sigma^+$  emission reduces faster than the  $\sigma^-$  transition with increasing field. This can be explained by a higher excitonic transition energy with a correspondingly smaller occupation probability at increasing magnetic field for  $\sigma^+$  than for  $\sigma^-$  polarization. No energy related spectroscopy has been carried out in order to clarify the origin of the diamagnetic shift.

In the same figure the measured  $\rho(B)$  data for sample G1769 (3 nm  $\text{Mn}_x\text{Ga}_{1-x}$  with  $x=0.55$ / 25 nm  $n^{++}$ -GaN with  $n=7 \cdot 10^{18} \text{ cm}^{-3}$ / UGOE LED1) is plotted. The distance to the QW from the injection contact ist 45nm. A hysteresis loop of  $\text{Mn}_x\text{Ga}_{1-x}$  superimposed to the Zeeman contribution of (In)GaN can be seen.

At zero magnetic field, a splitting  $\Delta\rho$  of roughly 0.34 % (T=80 K) and 0.31% (T=155 K) can be seen. The hysteresis loops are not symmetric around  $\rho = 0$  which might be due to a not perfectly adjusted quarter wave plate and linear polarizer at the beginning of the measurement.

A second sample with an additional 25 nm thick unintentionally doped GaN layer before the  $n^{++}$  doped GaN is examined, too. This sample shows a lower splitting than the sample without this layer, indicating that the diffusion length of spin polarized carriers cannot be very long in our structures. The result of this sample, G1770 (3 nm  $\text{Mn}_x\text{Ga}_{1-x}$  with  $x=0.55$  /25 nm  $n^{++}$ -GaN with  $n=7 \cdot 10^{18} \text{ cm}^{-3}$ / 25 nm n-GaN/ UGOE LED2), is shown in Figure 4.17 (70nm to the QW). The splitting is only 0.18% in remanence.

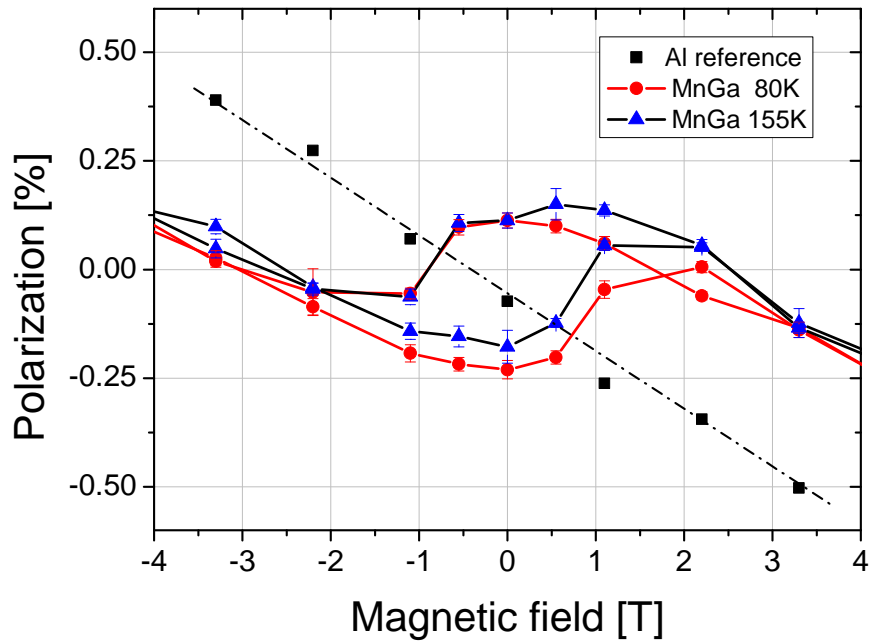


Figure 4.16: Circular polarization of the non magnetic Al reference sample and a MnGa based spin-LED. (Al sample G1780, MnGa sample G1769)

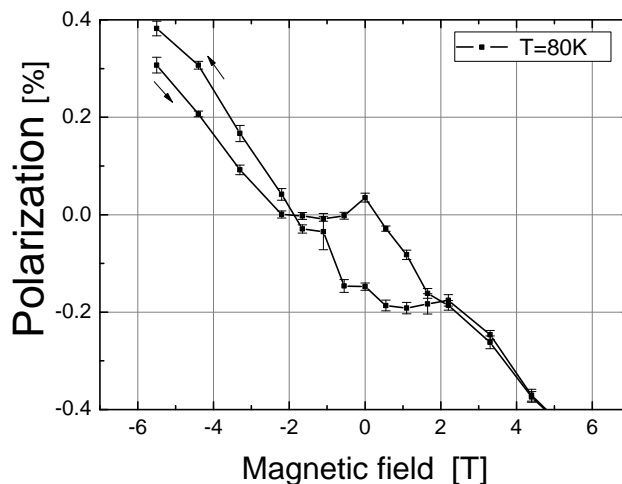


Figure 4.17: Results for sample G1770. The difference to G1669 is the added n-GaN layer (3 nm  $\text{Mn}_x\text{Ga}_{1-x}$  with  $x=0.55$  / 25 nm  $\text{n}^{++}\text{-GaN}$  with  $n=7 \cdot 10^{18} \text{ cm}^{-3}$  / 25 nm n-GaN / UGOE LED2) and the growth on UGOE LED2. The arrows indicate the magnetic field sweep directions.

With two data points, only a rough estimation about the spin diffusion length  $\lambda_{\text{SD}}$  can be done. The signal is almost reduced to the half value when the distance to the QW is changed from 45nm to 70nm. Assuming the same injection efficiency for both samples it means that the spin diffusion length is of the order of  $\approx 40$  nm (first order approximation: the doped Schottky layer is assumed to have the same spin scattering than the undoped layer) With the Einstein relation  $D=\mu kT/e$  the diffusion length is:

$$\lambda_{\text{SD}} = \sqrt{D\tau_{\text{SD}}} \quad (4.6)$$

Here,  $\tau_{\text{SD}}$  is the scattering time. Typical mobilities for n-type GaN at 80 K are  $200 \text{ cm}^2/\text{Vs}$  for non intentionally doped GaN with  $n=4 \cdot 10^{17} \text{ cm}^{-3}$  (measured with the van der Pauw method). This gives as a mean scattering time  $\tau_{\text{SD}}=12\text{ps}$  for a mobility of  $200 \text{ cm}^2/\text{Vs}$ . For comparison, Jahangir *et al.* report spin diffusion lengths at 80 K of 220nm ( $n=4.2 \cdot 10^{17} \text{ cm}^{-3}$ ) to 100nm ( $n=7.8 \cdot 10^{18} \text{ cm}^{-3}$ ) [16] which is larger than the estimated value for the MnGa spin-LED. This means that the spin scattering time in the grown layers in this thesis is shorter than in the work by Jahangir *et al.*



## 4.5 Magnetoabsorption effects in MnGa

One drawback of the top view geometry is the fact that the emitted light has to pass through the MnGa layer. Magnetic materials can absorb left and right circular polarized light differently (Magnetic circular dichroism, MCD) and therefore it can be possible that the measured optical polarization is entirely due to a MCD effect. In order to estimate the magnitude of a MCD effect of the ferromagnetic MnGa layer as mentioned by Adelman *et al.* in their MnGa/ GaAs based spin-LED [58], a 100 nm thick MnGa layer (grown on a template, no LED structure) has been probed in transmission at 300 K with a laser emitting at 442 nm which is close to the wavelength of 420 nm emitted by the LED. The setup is sketched in Figure 4.18. A linear polarized laser light from a He-Cd laser is chopped and directed on the back of a wafer including sapphire, GaN and MnGa. The intensity of the transmitted beam is measured with the same Quarter Wave Plate (QWP), analyzer (linear polarizer) and photodiode as in the spin-LED experiment.

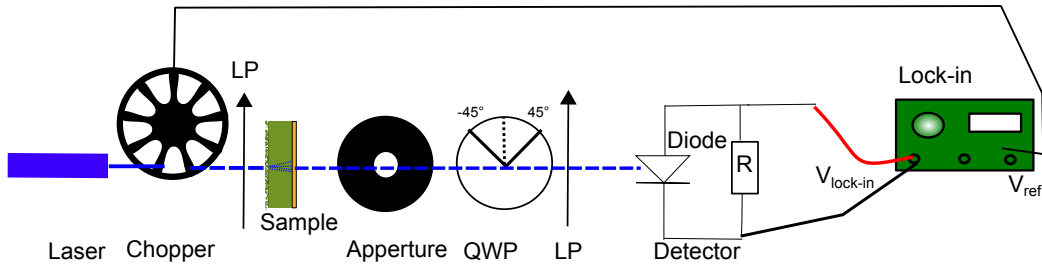


Figure 4.18: Setup for the study of the MCD effect in MnGa. A linear polarized laser light from a He-Cd laser is chopped and directed on the back of a wafer including sapphire, GaN and MnGa. The intensity of the transmitted beam is measured with the same QWP, analyzer and photodiode as in the spin-LED experiment. The sample is magnetized out of the plane before the measurement.

Linear polarized light consists of 50% left ( $\sigma^-$ ) and 50% right ( $\sigma^+$ ) circular polarized light, respectively. After transmission of the MnGa layer, the degree of optical circular polarization,  $\rho_{\text{Opt}}$ , has been measured in remanence for magnetic fields applied parallel to the (0001) direction of GaN, similar to the spin-LED measurements. In contrast to the spin-LED experiment, the sample has been magnetized only up to a field strength of 1 Tesla with the magnet in the Hall lab. To check for a MCD effect, the sample has been magnetized in the other field direction as well. This procedure has been repeated several times.

The magnetization in remanence with a field of 1T is not maximal. It is 80% of the total remanence magnetization, which has to be included in the estimation of the magnitude of the MCD effect.

In addition to the measurement of  $\rho_{\text{Opt}}$ , the angle  $\alpha$  of the QWP has been changed from  $-45^\circ$  to  $45^\circ$  in  $5^\circ$  steps and the intensity has been recorded. The transmission function of the system 'Linear Polarizer-QWP( $\alpha$ )-Analyzer' can be deduced with the help of the Müller matrix formalism, see Lars Watschke's thesis for details [101] or [115, Ch. 22] for a complete overview. The formula for the intensity in dependence of the angle of the QWP  $\alpha$  is:

$$I(\alpha) = I_0(\sigma^+) \cdot \cos^2(\alpha) \cos^2(\alpha - \beta) + I_0(\sigma^-) \cdot \sin^2(\alpha) \sin^2(\alpha - \beta) \quad (4.7)$$

$\beta$  denotes the angle between the first linear polarizer and the analyzer, its value is usually  $0^\circ$ . A Kerr effect in MnGa might turn the direction of the electric field vector of the transmitted linear polarized light.

Therefore, two different values for the optical circular polarization are ob-

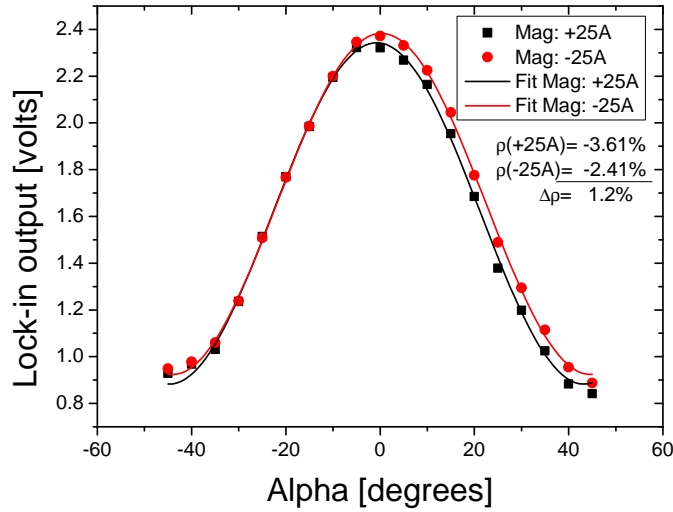


Figure 4.19: Measurement of the MCD effect .  $\alpha$  is the angle between the fast axis and the analyzer. The background of the template has been subtracted. The splitting in remanence  $\Delta\rho$  taking only the  $\pm 45^\circ$  values into account is roughly 0.6% whereas the fit according to Equation 4.7 gives 1.2%. (sample G1605)

tained. The known procedure from the spin-LED measurements,  $\rho_{\text{Opt}}$  with two measurements at  $\pm 45^\circ$ , and the value for  $\rho_{\text{Opt}}$  extracted from the fit parameters for  $I(\sigma^{\pm})$  according to Equation 4.7.

The result for the second analysis is plotted in Figure 4.19 for a 100 nm thick MnGa layer magnetized in both directions. From the data, the signal background of a template, without MnGa, has been subtracted. First of all, the polarization values for the two different field directions are not symmetric, they are -3.6% and -2.4%, respectively. Furthermore, the data points for both magnetizations at negative angles are very close to each other in contrast to positive angles.

The MCD effect of a 100 nm thick MnGa layer accounts to 1.2% in remanence after Equation 4.7 whereas the *simple*  $\rho_{\text{Opt}}$  measurement (only  $-45^\circ$  and  $+45^\circ$  position) gives 0.6%. Using the larger value and including the mentioned smaller remanence (only 80% of  $M(H=0T)$ ), the scale of the MCD effect down to the MnGa thickness used in the experiment,  $d=3.2$  nm, gives a contribution of roughly 0.5‰ to  $\rho_{\text{Opt}}$  which shows that the measured signal can mostly be attributed to spin injection.

### Additional considerations about the MCD measurements

The detection setup used in the experiment is the same as in the spin-LED which means that the basic working principle is not affected. The deduced polarization values in the first experiment (only  $\pm 45^\circ$  position of the QWP) were reproducible even after the 4th change of the magnetization. The only changes in the setup are: 1. Laser, 2. linear polarizer and 3. the sample in transmission geometry. To test the laser, the first experiment was carried out without a linear polarizer and the sample. The laser light had a degree of circular polarization of roughly -3% (measured in the conventional  $\pm 45^\circ$  positions). After installation of the linear polarizer, the value reduced to -0.5%. This shows, that not 100% linear polarized light is going through the sample, a small circular component is present in the light beam. For the explanation of the large values when the sample is installed, other effects have to be included as well. One effect could be a birefringence of the material. The laser beam is directed parallel to the c-axis of sapphire and GaN which means that no birefringence is present when the rays are parallel to this axis. A test with double side polished sapphire confirmed this: the measured circular polarization in transmission is the same as without sapphire. Unfortunately, the MnGa layers are grown on single side polished sapphire templates (epi-ready). The backside roughness of these wafers is of the order of  $1 \mu\text{m}$ . During transmission, the light is scattered at the back diffusely. It encounters different refractive indices while travelling through the sapphire at angles not parallel to the optical axis. There will be a random average

phase retardation that will affect the measured degree of circular polarization. In a work by Ko *et al.* the effect of a structured sapphire surface on the transmittance and reflectance of light is investigated [116]. One conclusion of the calculations is that if the dimensions of the scattering centers are larger than the wavelength of the light, interference effects are happening and the (near field) propagation direction is changed, Figure 4.20. Therefore, it is reasonable that the phase of the light changes after passing through the sapphire substrate because the birefringence in directions not parallel to the  $c$ -axis alter the polarization state.

For the *real* sapphire template, the effect of the surface is not as pronounced as in the model because the size, morphology and distance of scattering centers are not the same throughout the beam diameter; they are distributed around an average roughness of  $1\mu\text{m}$ , maybe with certain planes as facets. It is an open question if this is the reason for the large offset in the measurements.

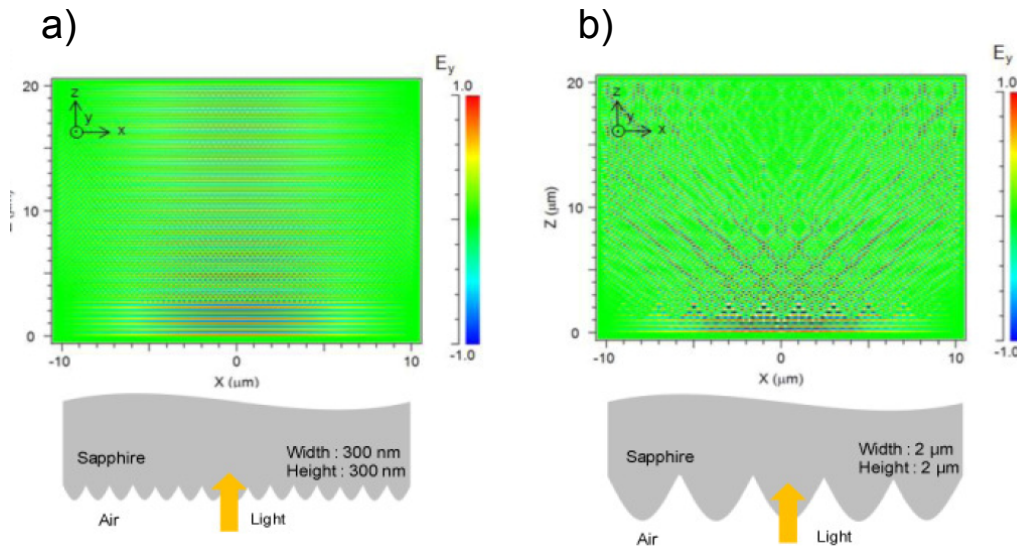


Figure 4.20: Calculations of the electric field distribution by Ko *et al.* for two different sapphire surface structures. The wavelength is  $\lambda=600\text{ nm}$ . Strong light interference patterns can be observed for both cases. If the size of the structures is larger than  $\lambda$ , the propagation direction can change. This can cause birefringence effects if the light is not transmitting parallel to the  $c$ -axis. Taken from [116]

# Chapter 5

## Electrical detection of spin injection

The electrical detection of spin injection is examined in 3-terminal and 4-terminal configuration. For the preparation of the 3-terminal setup no additional processing steps are required. The samples from section 3.5 can be used without any further processing.

The preparation of the 4-terminal setup is more time-consuming. The detection contact has to be close to the injection pad within the estimated spin diffusion length of GaN of roughly 100-1000 nm.

Therefore, due to the convenient preparation, the 3-terminal setup has been tried before the 4-terminal geometry. Furthermore, there is a successful report about electrical spin injection in the 3-terminal geometry in GaN with MnAs electrodes [16].

### 5.1 Detection setup

Two different measurement techniques and cryostats have been used to sense the spin signal. The first one is a continuous flow cryostat equipped with a water cooled magnetic coil in the Hall lab and the second is a physical properties measurement system (PPMS) with a superconducting coil. The advantage of the instruments in the Hall lab is that the operator can change nearly every parameter of the equipment. The PPMS machine is a closed system and custom made changes of the equipment are not easy to accomplish.

For the detection two measurement techniques are used:

1. A precision current source (or a battery) for the current generation plus a Keithley nanovoltmeter for the measurement of the voltage signal.
2. A lockin amplifier with a low noise AC current converter.

The best results in terms of a low background noise are obtained with the battery/nanovoltmeter and the lockin technique. Both techniques can be used quite easily in the *Hall lab*. Especially the battery solution convinced with a very stable current down to the nA range and no problems with ground loops.

To use the equipment at the PPMS, a BNC connector is available that goes directly to the connections of the internal sample holder. In total, two channels (2x current, 2x voltage) can be connected. A Lab view software is used to control both the PPMS and the nanovoltmeter.

If the battery is used as a current supply, the position of the battery has to be far away from the magnet, otherwise the magnetic field affects the electronics (or the battery's electrochemical system) in the battery box (in the box are some switches and transistors for the selection of the current range). This influences the output current, which can be seen in the voltage signal when the battery as the current source is connected, Figure 5.1 a). A hysteresis can be seen when the magnetic field is swept. When the battery is placed away from the magnet (1.5m are enough), no hysteresis is observed.

When the current is switched on, the Joule's heating of the sample generates a thermo voltage. Therefore, before the measurement can begin, a stabilization time of approx. 30min is needed. This behavior is shown in Figure 5.1 b). The noise level of the battery/nanovoltmeter solution is 300nV@100 $\mu$ A (RMS) in the 3-terminal geometry. A couple of process changes helped to achieve this value.

First, the reduction in the MnGa pad contact resistance by the added Al cap and the later exchange with Au and secondly, the Mesa definition with the wafer saw (possible only for 3-terminal geometry). Especially the Mesa definition helped to limit the current to the region between the pads and therefore unwanted current paths were avoided.

Another problem is the bonding process itself. Despite the added Au cover on MnGa, no Au bond wires stucked to the Au layer, only Al wires worked well. Therefore, it is possible that the bonding process itself damages the pad. Some bonds have a high resistance ( $\approx$ k $\Omega$ ) even when two bonds are placed on one pad and the resistance is measured between them. It might be that the thickness of the Au layer is not high enough and the bond process destroys both Au and MnGa layers. Maybe an additional 'hard' metal, Ti

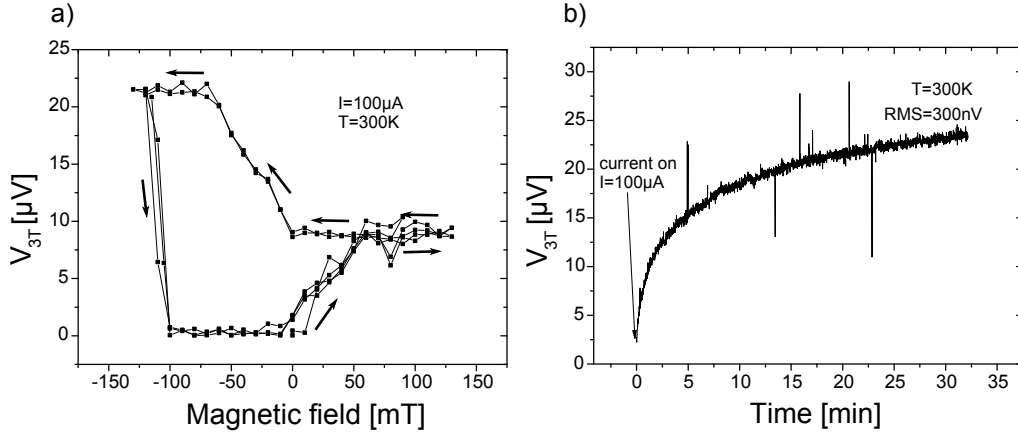


Figure 5.1: Problems of the measurement setup. a) When the battery is used and it is placed too close to the magnet, the generated current of the battery supply changes when the magnetic field is swept. This affects the voltage signal  $V_{3T}/V_{4T}$ . b) Generated thermo voltage due to the current going through the GaN layer. In both cases, the wiring is according to the 3-terminal setup in chapter 2. (sample G1682II)

or Cr before Au evaporation would have solved this problem.

As mentioned in chapter 2, the signals in 3-terminal geometry are large in comparison to 4-terminal devices, of the order of  $300\mu\text{V}$  [16]. Therefore, a signal related to spin injection should be easily measurable in 3-terminal geometry.

In the 4-terminal geometry the noise value is lower ( $\text{RMS}=150\text{nV}$ ), because the contribution of the current to the voltage signal is smaller. It is worth mentioning that it is not possible to rule out all parasitic contributions like a Hall effect or thermovoltages completely. A small background is always superimposed to the data. Furthermore, the detection pads are not exactly on one equipotential line, which means that a small current is flowing despite the non-local setup.

According to theory, a spinpolarization of 1% generates a signal of roughly  $5\mu\text{V}$  when the ferromagnet has an intrinsic polarization of  $\eta=0.42$  and the interface filter effect is  $\alpha=0.5$ . Therefore, the setup is capable of measuring polarization values down to roughly 0.1-0.5% easily (with the given values of the ferromagnet).



## 5.2 3-terminal measurements

For a set of Schottky barrier doping levels ranging from  $5 \cdot 10^{18} - 3 \cdot 10^{19} \text{ cm}^{-3}$  the  $\text{Mn}_x\text{Ga}_{1-x}/\text{GaN}$  samples are magnetized in-plane. An applied out of plane field should show a Hanle effect, chapter 2.

No Hanle signal is observed in all cases. Different temperatures and currents have been tried, too. The measurements are repeated in the PPMS, but also here no signal related to spin injection could be detected.

## 5.3 4-terminal measurements

### Sample Preparation

For the preparation of the 4-terminal geometry electron beam lithography (ebeam) and reactive ion etching (RIE) are used. The first step is the preparation of the MnGa pads by reactive ion etching, Figure 5.2 a). The separation of the contacts ranges from 150 nm to 1200 nm. It is possible to measure different distances simultaneously. The problem is that the RIE etch rate of the metal is low in comparison to the etch rate of the resist. A couple of recipes have been tried, but none is able to increase the etch rate above 10nm/min. It can happen that the resist is gone before the complete  $\text{Mn}_x\text{Ga}_{1-x}$  layer is etched. A wet chemical etch is not easy for sub  $\mu\text{m}$  structures because an undercut and therefore a removal of the ferromagnet has to be avoided.

Furthermore, the Si-doped region between the pads has to be removed to be sure that the current goes through the layer and not the highly doped surface region. The standard recipe ('Basic GaN' with a power of 200W, see appendix) for GaN reactive ion etching produces rough surfaces and therefore the recipe is changed to a 'low damage' recipe. To the standard gases Cl and  $\text{BCl}_3$ , Ar is added and the power is reduced. This results in a RMS value of 1 nm ( $5 \times 5 \mu\text{m}^2$  scan area) after etching. All process parameters can be found in the appendix.

The second step is the etch of the channel, Figure 5.2 b). The channel consists of a 500nm thick GaN:Si GaN layer ( $n = 1 \cdot 10^{18} \text{ cm}^{-3}$ ). This is close to the metal insulator transition where the spin diffusion length is believed to be the longest [7].

The 500 nm etch recipe is the same 'low damage' recipe as before. A smooth surface is needed for the third step, the deposition of 500 nm  $\text{SiO}_2$  on the



etched GaN for insulation purposes and height adjustment for the following contact metallization process. The metallization consists of 20 nm Au on 20 nm Ti. An optical micrograph picture of the complete device is shown in Figure 5.2 c).

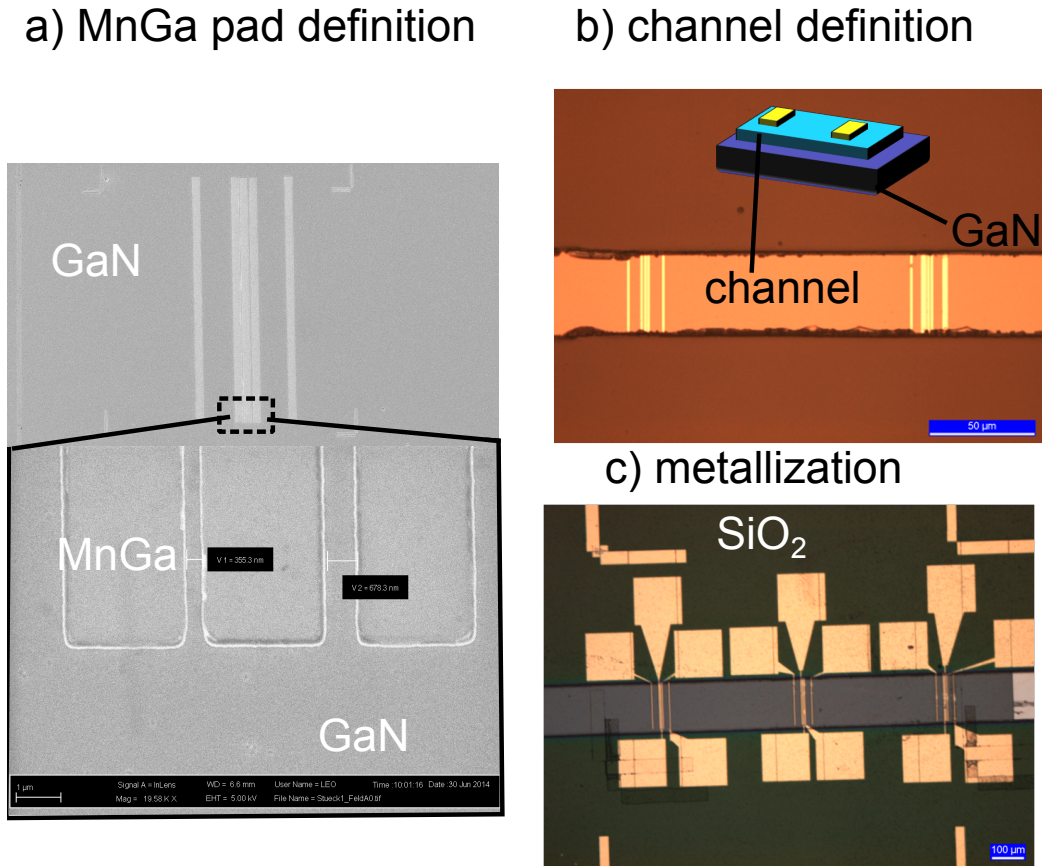


Figure 5.2: Overview of the processing steps for the 4-terminal measurements (design I). a) MnGa pad definition with ebeam and RIE. b) Channel definition by RIE and c) SiO<sub>2</sub> deposition and contact metallization for bonding purposes.

The ebeam lithography of the contacts and the lift-off of the evaporated metals made some difficulties. On the resist a thin metal film, 3nm, is evaporated everywhere to get rid of charging effects of the insulating layers (oxide). Otherwise, the exposed structures are shifted in the following exposure and are not at the exact positions.

Sometimes it is not possible to remove all the resist (and the metal on top of the resist), because the resist has only a thickness of 200-300nm, Figure 5.3.

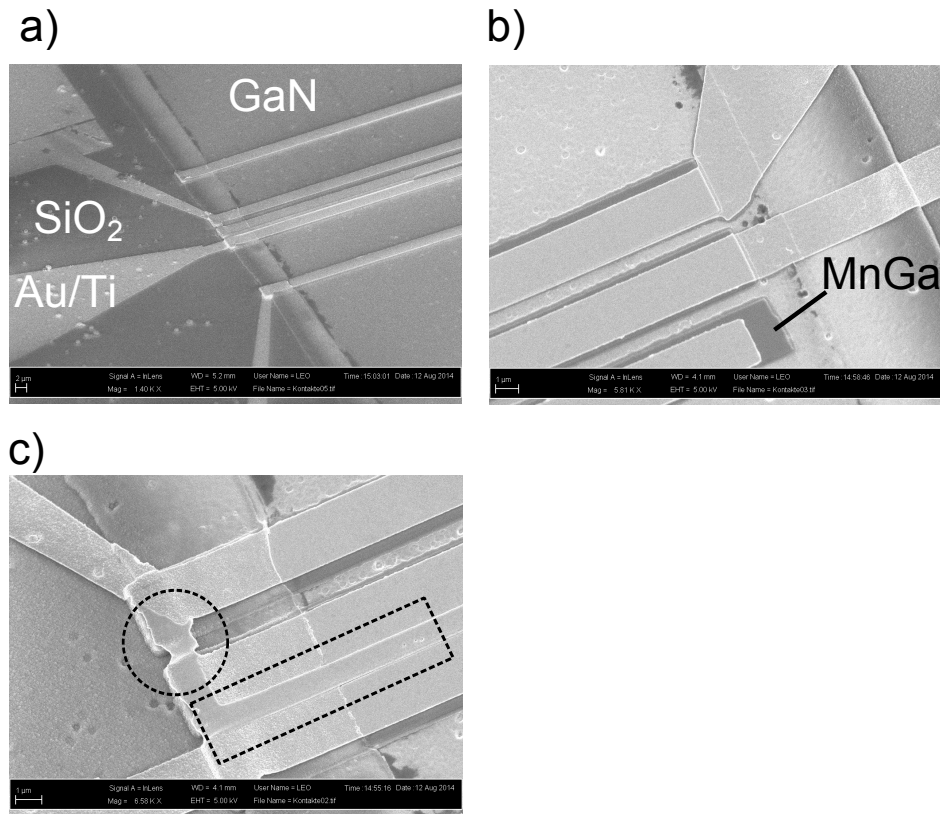


Figure 5.3: SEM pictures of the structured devices (design I). a) Overview of the MnGa pad and the Au/Ti connections. b) Close view of the MnGa pads with the metallization and a successful lift-off. b) Close view of an unsuccessful lift-off which creates a short cut.

This can cause problems when the metallization thickness is approximately as thick as the resist. This is the reason why the thickness of the Au/Ti contacts is kept thin. Furthermore, an ultrasonic bath at elevated temperatures, 60-80°C, can help in the lift-off process. A second design has been used later. The problem of the first design is that the current goes through the 4 $\mu$ m thick template left and right of the channel. The potential landscape is not well defined and a large voltage offset is measured at  $V_{4T}$ .

The mesa definition for the larger structures (TML) was done by a wafer saw. This is not possible in this case, because the width of the structures is only 100 $\mu$ m. The use of the saw would probably destroy the channel.

In the second design, the channel is etched completely down to the sapphire. It is not easy to etch 4 $\mu$ m thick GaN because the resist is etched faster or it cross links with the surface and is not possible to remove after RIE treatment. No chemical etchant for Ga-polar GaN is available, therefore RIE is the only



In this geometry only three different Schottky doping profiles could be measured:

1. 25nm GaN:Si with  $n=5 \cdot 10^{18} \text{ cm}^{-3}$
2. 25nm GaN:Si with  $n=7 \cdot 10^{18} \text{ cm}^{-3}$
3. 15nm GaN:Si, linearly graded from  $n=2 \cdot 10^{18} \text{ cm}^{-3}$  –  $8 \cdot 10^{18} \text{ cm}^{-3}$  / 15nm GaN:Si  $8 \cdot 10^{18} \text{ cm}^{-3}$ .

The third sample could only be measured with a pad distance between injector and detector of  $1\mu\text{m}$  because the other connection lines were broken. Within the limits of this setup, no spin injection from  $\text{Mn}_x\text{Ga}_{1-x}$  into GaN with the mentioned doping profiles and the growth parameters could be measured.

# Conclusion

## Discussion

A clear answer to the question whether MnGa is a suitable spin injector in GaN based devices is not easy to find. First of all, the gained insight into the structural and electronic properties of the MnGa/ GaN interface are promising, but both spin injection experiments, optical and electrical, showed only a weak or no signal related to spin injection. In order to give a clear statement, the experimental findings are discussed in the following. At the beginning the structural properties and the MBE growth of MnGa on GaN are addressed in more detail. Secondly, the spin injection experiments itself are reviewed and thirdly, other possible sources of errors, e.g. the measured in-diffusion of Mn into GaN by EELS are considered as well.

In contrast to the work by Lu *et al.* [59] who deduced a 30° rotation of the MnGa(111) plane with respect to the GaN(0001) surface, non rotated MnGa planes could be obtained, too. According to first principles calculations of P. Blöchl (not published), the formation energy of non rotated planes is too high to be sustained.

There are two possible explanations why the results differ from the experiments by Lu *et al.* and the theoretical calculations. One is the low growth rate of 0.5-0.8 nm/ min and the second is the high substrate temperature of 330-400°C used for the growth of the Mn<sub>x</sub>Ga<sub>1-x</sub> layers. A check how the growth rate affects the epitaxial relationship could not be performed because an increase of the growth rate was not possible due to the limitations of the Mn effusion cell. It is an open question if a higher growth rate would have shown closed layers at lower substrate temperatures similar to Lu *et al.* .

The second point, the influence of the substrate temperature on the orientation of MnGa planes on the GaN surface shows two distinct trends. At lower substrate temperatures between 150-250 °C, the layers grow in an is-

---

land growth mode. In contrast to the work of Lu *et al.* a closed layer at these low temperatures could not be obtained. Around 330 °C, non rotated MnGa planes grow, whereas at 400°C, rotated MnGa planes grow. From the TEM pictures one can conclude that the  $\text{Mn}_x\text{Ga}_{1-x}$  layers grown at higher temperatures have a high crystal quality and that the interface is monocrystalline. Between these two temperatures, a transition region exists where both orientations appear at the same time.

Other explanations are possible as well. A not completely desorbted Ga wetting layer from the GaN growth or Ga droplets on the GaN surface have an influence on the growth process. Sometimes no RHEED diffraction spots or a mixture of rotated and non rotated planes could be observed despite a high quality GaN layer underneath in these cases. Theoretical calculations of the electronic structure of rotated and non rotated MnGa/ GaN interfaces are needed to answer the question which atomic surface arrangement is more useful in terms of spin injection.

In most of the optical spin injection experiments in literature, a top view geometry is not used because the emitted light has to pass through the magnetic layer. This layer can change the light properties as well (Magnetic circular dichroism (MCD), Kerr effect (MOKE)).

Two spin-LEDs have been analyzed, one with a distance of 45 nm and the other of 70 nm to the InGaN quantum well. The two samples showed different polarization behavior. On both samples, the same  $\text{Mn}_x\text{Ga}_{1-x}$  layer with the same thickness had been grown. The only difference is the additional unintentionally doped GaN layer before the doped Schottky region. If the measured circular polarization would be entirely due to magneto optical effects, the samples should have shown the same behavior. An experimental check of the MCD effect was done with a laser in a transmission geometry. The laser light with a wavelength of  $\lambda=442\text{ nm}$  was sent through a 100 nm thick MnGa layer. A splitting of 1.2% could be measured in remanence in this geometry when the magnetization was reversed. No MCD effect of thin MnGa layers could be measured within the limits of the setup. A scale of the magnitude of the MCD effect down to the used MnGa thickness of  $d=3.2\text{ nm}$  in the LED experiment gave a value of 0.5 ‰. Therefore, the polarization can mostly be attributed to a polarization of carriers.

In the 3-and 4-terminal geometry, no spin signal could be measured. In the 4-terminal case, it could be that during processing the material is damaged. Maybe the RIE treatment increased spin scattering in the GaN channel. No (easy-to-use) wet chemical etchant for Ga-polar GaN is available [117] [118]. Therefore, the highly doped region at the surface can only be removed by RIE. A test of the influence of RIE on the electrical properties of GaN could



be a measurement of the electron mobility before and after RIE treatment. The closest distance in the 4-terminal measurements between spin injector and detector is approx. 150 nm. It is possible that the spin diffusion length is smaller than 150 nm in our device. A rough estimation of the spin-LED experiments gave 40 nm as spin diffusion length. This means that the corresponding spin signal can not be measured. A rough estimation of the spin scattering time gave a value of 12 ps. Jahangir *et al.* measured as a spin diffusion length 220 nm for a doping level of  $4.2 \cdot 10^{17} \text{ cm}^{-3}$ . Therefore, the quality of the grown GaN layers (e.g. high dislocation density) can be a limiting factor as well in addition to the MnGa/ GaN interface.

The absence of any spin related signal, even in the 3-terminal geometry, means that despite the high quality epitaxial interface, MnGa/ GaN heterostructures under the mentioned growth conditions (  $T_S=400^\circ\text{C}$ , growth rate 0.5-0.8nm/ min) are not suitable for spin injection.

It is not clear if a magnetically dead layer is present at the interface. These effect has been reported for a couple of material combinations [119] [120]. It is possible that the strain induced by the epitaxial growth suppresses the magnetism in  $\text{Mn}_x\text{Ga}_{1-x}$  at the interface. From other systems, e.g.  $\text{LuMnO}_3$ , it is known that the magnetic properties change from ferromagnetic to antiferromagnetic ordering when the material is grown on a foreign substrate [121]. According to the authors, the magnetic moment distribution of these strained films is peaked around the substrate interface region. For spin injection itself only the magnetism of the last couple of monolayer counts. It can happen that the magnetism of these last monolayers differs from the bulk values measured with SQUID or VSM.

Another possible reason for the low efficiency could be the  $\text{Mn}_x\text{Ga}_{1-x}$  growth process itself. The high substrate temperature could lead to a in-diffusion of Mn into GaN. Hwang *et al.* deposited Mn on a clean GaN(0001) surface and annealed the sample at  $500^\circ\text{C}$  for 6h (thermal diffusion)[79]. The authors performed in-situ XPS depth profile measurements and found Mn 7 nm under the surface, SQUID measurements showed primary paramagnetic behavior. Therefore, it is reasonable that Mn diffuses even at  $400^\circ\text{C}$  into the GaN matrix and depolarizes the injected carriers. According to the EELS analysis of the MnGa/ GaN interface region, the very interface consists of diluted (Mn,Ga)N. From the Fe/ GaAs system it is known that an intermixing between Fe and GaAs can happen [122] [123] [124] [125] . In the last reference by Schultz *et al.* , this issue is discussed in terms of spin injection from Fe in GaAs. They concluded that even small changes of the epitaxy process can change the composition of the  $\text{Fe}_x\text{Ga}_y\text{As}_z$  phase at the interface. Depending on the phase, ferromagnetic or antiferromagnetic ordering can occur.

---

The influence of annealing on the complex band structure of Fe/GaAs has been investigated by Hu *et al.*. They showed that small changes in the interfacial band structure drastically change sign and magnitude of the spin signal [126]. In this context another work by Stroud *et al.* should be mentioned [127]. They explored the dependence of spin polarization on interface defect density. A clear decrease of spin polarization with increasing interface defect density could be measured by the authors. All ideas could be explanations for the MnGa/GaN system as well.

After crossing the interface, carriers can encounter spin scattering events in the bulk semiconductor. The sample with the longer distance (70 nm) to the QW reveals that the spin diffusion length has to be very short. From optical experiments with excitons in GaN, which are not electrically injected carriers, it is known that the spin relaxation increases with increasing dislocation density (defect-assisted *Elliot-Yafet* mechanism) [128]. This can be another reason for the low degree of polarization as the dislocation density in the measured LEDs is very high (higher  $10^9$  cm<sup>-2</sup> region).

Another argument for the low polarization is the temperature dependence of the measured GaAs diode. A large polarization of 10% at low temperatures dropped to 1% above 100 K. Of course, the question is whether the spin polarization temperature dependence of GaAs can be applied to GaN, but the basic trend should be similar. The GaN-based spin LED showed a low spin polarization of 0.4% at 80K.

Maybe a lowering of the temperature would have increased the polarization as well. This assumption could not have been checked because of the high resistance of the diode at low temperatures. A failure of the LED due to the excessive heating can occur.

It can be concluded that MnGa on GaN grown under the mentioned conditions is not a good combination for spintronic applications. The growth conditions have to be optimized to make Mn<sub>x</sub>Ga<sub>1-x</sub> on GaN suitable for future applications.

First of all, the exact chemical composition at the MnGa/GaN interface is not known. It has to be investigated in dependence of the growth conditions (temperature, Mn:Ga ratio, growth rate). Due to the easy sample preparation, it is highly recommended to start future spin injection experiments with a LED structure or the 3-terminal setup.



## Summary

In this work, the ferromagnet MnGa has been investigated for its possible use as spin source in GaN based spintronic devices. First of all, the fast change from GaN to MnGa diffraction spots in RHEED experiments indicates an interface of high crystal quality. The abrupt interface and epitaxial relationship was confirmed by TEM experiments. Furthermore, it was shown that the Mn:Ga ratio in the layers can be used to alter the strain state of  $\text{Mn}_x\text{Ga}_{1-x}$  and therefore the magnetic properties of the ferromagnet.

The electrical measurement of MnGa/GaN Schottky diodes in reverse direction gave insight into the transport process. Different doping levels of GaN have been investigated in order to find the best conditions for spin injection. It was found that for doping concentrations higher than  $7 \cdot 10^{18} \text{ cm}^{-3}$  direct tunneling is the dominant transport mechanism in revised biased MnGa/GaN Schottky diodes. Therefore, in the following spin injection experiments, a doping of  $5 - 7 \cdot 10^{18} \text{ cm}^{-3}$  has been chosen as a compromise between high direct tunneling current and good structural quality (less scattering).

With a spin LED, a spin signal could be measured which follows the magnetization of the MnGa electrode. The spin polarization was 0.4% in remanence at 80 K for a sample with a distance of 45 nm from the ferromagnet to the QW region. A second spin-LED with a larger distance of 70 nm to the QW showed a smaller polarization of 0.2% at 80 K. The electrical spin injection experiments conducted in 3- and 4-terminal geometry showed no spin injection. Under the used conditions, the  $\text{Mn}_x\text{Ga}_{1-x}$ /GaN system is not a suitable combination for Spin FETs.

---

# Appendix A

## Process parameters

### A.1 Optical Lithography (for TML structures)

#### A.1.1 Positive Resist

- Spincoating of ARP 3250 (or ARP 3740) 8000RPM 60s (A lower speed works, too. Just the resist thickness to the corner of the sample increases which is important on small samples.)
- Bake out 90°C 90s on Hotplate. (For thicker resist repeat the coating and baking step.)
- Exposure for 1.5s at 30mW/cm<sup>2</sup> in the MJB4 Mask Aligner
- Development in a solution of AR300-26:H<sub>2</sub>O 2:1 (ARP3250) for 20-30s or 1:1 (ARP3740).
- Hardbake 110°C for 5min for better plasma stability.
- Removal with AR300-70 (Acetone works, too. But residues might stay at the surface.)

#### A.1.2 Negative Resist

- Spincoating of ARN 4340 6000RPM 60s.
- Exposure for 1.5s at 30mW/cm<sup>2</sup> in the MJB4 Mask Aligner.
- Baking 90s 95°C.

- Development AR300-47 10s.
- Hardbake 110°C for 5min for better plasma stability.
- Removal with AR300-70 (Acetone works, too. But residues might stay at the surface.)

## A.2 Electron beam lithography (4-terminal geometry)

### A.2.1 Negative resist (MnGa pad definition)

- Spincoating ARN 7520.18 4000RPM/60s.
- Baking 90s 85°C Hotplate.
- Exposure: for larger structures  $>1\mu\text{m}$  dose  $25\mu\text{C}/\text{cm}^2$ . Smaller structures  $10\mu\text{C}/\text{cm}^2$ .
- Baking 85°C 2min.
- Development AR300-47 4:1 H<sub>2</sub>O 40s. (A longer development time reduces the thickness and the size of the structures considerably)

### A.2.2 Positive resist (for metalization and lift off)

- Spincoating ARP 679.04 4000RPM 60s
- Hotplate 150°C 90s
- Exposure  $120\mu\text{C}/\text{cm}^2$
- Development in a solution of AR300-26:IPA 1:3 60-90s

## A.3 RIE, PECVD and wet chemical etching

### A.3.1 RIE of GaN

- clean chamber with O<sub>2</sub> plasma.

- Basic GaN recipe: 7°C chuck temperature, 2sccm BCl<sub>3</sub>/ 10 sccm Cl, 200W 20mtorr chamber pressure, etch rate 100-120nm/min (depends on doping)
- low damage recipe: 2sccm BCl<sub>3</sub>/ 2 sccm Cl/ 10sccm Ar, 10mtorr, 150W, etch rate 25-30nm/min.
- Ar sputter only: 20sccm Ar, 20mtorr, 400W, etch rate 20nm/min.

### A.3.2 RIE of metals

- Al etch: 20sccm Bcl<sub>3</sub>, 5sccm Cl, 20mtorr, 100W. etch rate >50nm/min.
- MnGa etch: 20sccm BCl<sub>3</sub>/ 5sccm Cl, 400W 20mtorr, 8nm/min (wet etch better)
- Ar only RIE is possible for MnGa, too. See RIE of GaN. Works for small thicknesses,too.

### A.3.3 PECVD of SiO<sub>2</sub> (for insulation)

- cleaning of the chamber with CHF<sub>3</sub>/Ar plasma (important)
- standard SiO<sub>2</sub> recipe at 120°C and not at 300°C:
  - pump and purge with N<sub>2</sub> 5min/710sccm, N<sub>2</sub>O plasma 1 min/ 130sccm/20W.
  - SiO<sub>2</sub> deposition 400 sccm 5% SiH<sub>4</sub>(Ar)/ 30sccm NH<sub>3</sub>/ 380 sccm N<sub>2</sub>, 20W. rate 70-80nm.

### A.3.4 Wet chemical etch for MnGa

- Al cap removal: dip in 37% HCl for a couple of seconds
- MnGa etch: solution of 20ml H<sub>2</sub>O/ 0.15ml 37% HCl / 0.15ml H<sub>2</sub>O<sub>2</sub>. etch rate 20nm/min. (If you use disposable pipettes (one time use), the 0.15ml are approx. 1cm fill level. )

## **A.4 Univex (metallization)**

- Sputtering: Ar sputtering with 450W, 5sccm, plasma strike at 40 sccm. MnGa etch rate: 2nm/min. For GaN the etch rate is 5nm/min.
- (ebeam evaporation of 20nm Ti.)
- Resistance heated evaporation of 40nm Au.

# Appendix B

## Hints, tips & tricks

### B.1 Cleanroom

#### B.1.1 Mask aligner

- If the resist is older than one year, don't waste your time and buy new one. Especially when it is opened. For test purposes old resists are ok, but the etch stability and development/removal quality is not comparable to new ones.
- For smaller pieces, 4mm x 4mm, the resist at the side of the sample is really thick. This can cause problems in the mask aligner. It is possible to remove the outer resist with a scalpel. When the sample is even smaller, the mask aligner cannot fix the sample with the vacuum holes of the chuck. You can use the blue adhesion foil and fix the sample on that foil before exposing or even before spincoating when the sample does not stick on the chuck of the coater.
- Try to use the resist as *fresh* as possible. Spincoating and doing nothing for two weeks is not good.

#### B.1.2 Univex

- The Ar sputtering works best at low Ar fluxes (High sputter rate). To ignite the plasma, a higher flux (40sccm) is needed. First use the *auto* button with 450W and 40sccm and start the plasma. Then reduce

the flux to 5sccm and simultaneously change the control parameter to *Present 3*. You see immediately that the plasma is more directed to the sample than with 40sccm.

- Don't put too much Al inside the crucible. It crawls over the crucible.
- Wait until the pressure is in the mid  $10^{-6}$  mbar range. I have the feeling that the contacts are better but I didn't check it systematically.
- The Au evaporation process consumes a lot of Au. If you have the time, try other metals as well.
- The quartz crystal of the thickness monitor needs to be replaced below 92% health. Even below 95% the error in thickness is of the order of 10-15%.

### B.1.3 Electron beam lithography

- It is possible to expose the resist the day after spincoating. One week later is definitely too much.
- There is a good step-by-step introduction how to use the eline by Carla Oppo. It can be found here [129].
- For the exposure on insulating substrates, charging becomes a serious issue. You can avoid this by deposition of a thin 2-4nm thick metal layer on the resist before exposure (needs to be removed before development).

### B.1.4 RIE/ PECVD

- Clean the chamber before processing
- When the plasma won't strike, set the strike pressure to a higher value (30-40mtorr) and set the ramp rate to 1.
- When the power or the etch time is too long, the photoresist cross-links with the surface. Then it is not possible to remove it even with O<sub>2</sub> plasma.



## B.2 Hall lab and PPMS

### B.2.1 Hall setup- Continuous flow cryostat

- The thin cables that go from the BNC connector of the sample holder to the chip carrier holder have a resistance of  $60\ \Omega$ . Keep that in mind when performing 2-point resistance measurements.
- Sample Labview code can be found in the share\_rizzi\Labview folder
- Connect the instruments to one common power line.
- The insulation vacuum had a leak, it was fixed but it is not completely closed.
- Don't operate the heater at the maximum power, otherwise the samples' temperature differs dramatically from the temperature reading.

### B.2.2 Probestation

- Don't press the needles with too much force on the sample. Otherwise the needle and the surface of the sample might get damaged.

### B.2.3 Wire bonder

- Typical problems with the wire bonder are:
  - Wrong height of the bond wedge (The angle of the wire is too steep)
  - The material of the wire doesn't fit to the material of the pad or the thickness of the material on the bond pad is not high enough.
  - Too much power destroys the surface. Try to optimize the bonding by adjusting time and force.
  - A heating to roughly  $70\text{-}80^\circ\text{C}$  improves the sticking of the bond to the pad (Don't burn your fingers...)
- For our GaN templates, glue an old piece (e.g. from the corner of a 2" wafer) under the sample inside the chipcarrier. This height adjustment makes the bonding much easier because the vertical difference from the bond pad of the chipcarrier to the sample is smaller.

### B.2.4 PPMS

- The puck for the use of our chipcarriers (DIP 14) with the PPMS are in the shelf next to the bonder.
- There are two BNC to PPMS adapters available, one belongs to the 1st institute and can be found in the PPMS II room. The second is ours and is next to the PPMS puck.
- Sometimes the sample doesn't fit into the holder of the VSM unit. You can place the sample into the transparent pills from SQUID and fix it.
- Read the manual of the option you want to use.

### B.3 MBE

- A growers cookbook for layers can be found in the thesis of Daniel Broxtermann [27].
- The spring ring of the sample holder loses its tension with time. Carefully bend it back to the old diameter.
- To get a good RHEED picture, the sample has to be at least on the same height as the front sample holder plate.
- Check the water flow of the cooling system from time to time.
- Try to avoid large droplets on the surface, you don't get rid of them by nitridation.
- When you change the temperature, wait 10min for stabilization.
- Don't rely on RHEED completely. Try different locations on the sample.



## **Additional notes & collaborations**

The LED structure of the Spin-LED is MOCVD grown by the group of Prof Dr. Mishra from the University of Santa Barbara (UCSB). I supervised a couple of master and bachelor thesis during my PhD. Two were closely related to my topic. The preparation and electrical characterization of the MnGa/ GaN heterostructures was partly embedded in the master thesis of David Disterheft [98], he contributed to the electrical measurements. The same is true for the setup and the measurement of the MnGa spin-LED which was part of the master thesis of Lars Watschke [101]. The TEM pictures were recorded by Arne Urban and Reza R. Zamani. Some of the XRD and SQUID measurements have been done by Amilcar Bedoya-Pinto.

## **Acknowledgments**

First of all I would like to thank Prof. Dr. Angela Rizzi and Dr. Jörg Malindretos for their great support throughout of my work in the past five, including my diploma time, 6.5 years. Thanks to Prof. Dr. Markus Münzenberg for finding the time co-refereeing my thesis.

I appreciate the support of Lars Hahn, born Watschke, and David Disterheft. Both helped a lot.

Greetings go out to the other former PhD students Arne Urban, Carla Ivana Oppo, Daniel Broxtermann and Amilcar Bedoya-Pinto for the good time in the lab and other members of Angela's group (including Thomas Lehmann).

Last but not least I want to thank Prof. R. G. Ulbrich for his help in the optic lab, fruitful discussions, the x-y chart recorder and his chocolate donations.

---

# Publications worth reading to get into the topic

This list should provide a guide for readers who are not familiar with MnGa/GaN based spintronic. These selected publications form the basis of the work and are often cited throughout the thesis. Therefore, it makes sense to read them for better understanding of the whole topic.

## **Spininjection: concepts and challenges**

Supriyo Datta and Biswajit Das. *Electronic analog of the electro-optic modulator*. Applied Physics Letters , 56(7):665-667, 1990.

David D. Awschalom and Michael Flatté. *Challenges for semiconductor spintronics*. Nat Phys 3 (3). 153-159, 2007.

G. Schmidt, D. Ferrand, L. Molenkamp, A. Filip, and B. van Wees. *Fundamental obstacle for electrical spin injection from a ferromagnetic metal into a diffusive semiconductor*. Physical Review B , 62(8):R4790- R4793, 2000.

## **Measurement techniques**

D. D. Awschalom, Y. Ohno, D. K. Young, B. Beschoten, F. Matsukura, and H. Ohno. *Electrical spin injection in a ferromagnetic semiconductor heterostructure* . Nature , 402(6763):790-792, 1999.

C. Adelman, X. Lou, J. Strand, C. Palmstrøm, and P. Crowell. *Spin injection and relaxation in ferromagnet-semiconductor heterostructures*. Physical Review B , 71(12), 2005.

B. Jonker, Y. Park, B. Bennett, H. Cheong, G. Kioseoglou, and A. Petrou. *Robust electrical spin injection into a semiconductor heterostructure*. Physical Review B , 62(12):8180-8183, 2000.

### MnGa and GaN spintronic

Erdong Lu, David Ingram, Arthur Smith, J. Knepper, and F. Yang. *Reconstruction Control of Magnetic Properties during Epitaxial Growth of Ferromagnetic  $Mn_{3-\delta}Ga$  on Wurtzite GaN(0001)*. Physical Review Letters , 97(14), 2006.

A. Bedoya-Pinto, C. Zube, J. Malindretos, A. Urban, and A. Rizzi. *Epitaxial  $Mn_xGa_{1-x}$  layers on GaN(0001): Structural, magnetic, and electrical transport properties*. Physical Review B , 84(10),2011.

C. Adelman, J. L. Hilton, B. D. Schultz, S. McKernan, C. J. Palmstrøm, X. Lou, H.-S. Chiang, and P. A. Crowell. *Spin injection from perpendicular magnetized ferromagnetic MnGa into (Al,Ga)As heterostructures*. Applied Physics Letters , 89(11):112511, 2006.

Shafat Jahangir, Fatih Doğan, Hyun Kum, Aurelien Manchon, and Pallab Bhattacharya. *Spin diffusion in bulk GaN measured with MnAs spin injector*. Physical Review B , 86(3), 2012.

# Bibliography

- [1] M. N. Baibich, J. M. Broto, A. Fert, Van Dau, F. Nguyen, F. Petroff, P. Etienne, G. Creuzet, A. Friederich, and J. Chazelas. Giant Magnetoresistance of Fe(001)/Cr(001) Magnetic Superlattices. *Phys. Rev. Lett.*, 61(21):2472–2475, 1988.
- [2] G. Binasch, P. Grünberg, F. Saurenbach, and W. Zinn. Enhanced magnetoresistance in layered magnetic structures with antiferromagnetic interlayer exchange. *Phys. Rev. B*, 39(7):4828–4830, 1989.
- [3] T. Miyazaki and N. Tezuka. Giant magnetic tunneling effect in Fe/Al<sub>2</sub>O<sub>3</sub>/Fe junction. *Journal of Magnetism and Magnetic Materials*, 139(3):L231–L234, 1995.
- [4] Supriyo Datta and Biswajit Das. Electronic analog of the electro–optic modulator. *Applied Physics Letters*, 56(7):665–667, 1990.
- [5] J. M. Kikkawa. Room-Temperature Spin Memory in Two-Dimensional Electron Gases. *Science*, 277(5330):1284–1287, 1997.
- [6] D. D. Awschalom, Y. Ohno, D. K. Young, B. Beschoten, F. Matsukura, and H. Ohno. Electrical spin injection in a ferromagnetic semiconductor heterostructure. *Nature*, 402(6763):790–792, 1999.
- [7] B. Beschoten, E. Johnston-Halperin, D. K. Young, M. Poggio, J. E. Grimaldi, S. Keller, S. P. DenBaars, U. K. Mishra, E. L. Hu, and D. D. Awschalom. Spin coherence and dephasing in GaN. *Physical Review B*, 63(12), 2001.
- [8] T. Dietl. Zener Model Description of Ferromagnetism in Zinc-Blende Magnetic Semiconductors. *Science*, 287(5455):1019–1022, 2000.
- [9] Amilcar Bedoya-Pinto. *Structural, magnetic and electrical transport properties of GaN-based magnetic semiconductors and hybrid structures*. PhD thesis, Georg-August Universität, Göttingen, 2010.

- 
- [10] Martin Röver. *GaN: Gd-Ein verdünnter magnetischer Halbleiter?* PhD thesis, Georg-August Universität, Göttingen, 2011.
- [11] A. F. Orlov, L. A. Balagurov, I. V. Kulemanov, N. S. Perov, E. A. Gan'shina, A. S. Semisalova, A. D. Rubacheva, V. I. Zinenko, Yu.A. Agafonov, and V. V. Saraikin. Magnetic and magneto-optical properties of ferromagnetic semiconductor GaN: Cr. *Physics of the Solid State*, 54(2):283–286, 2012.
- [12] J. B. Gosk, M. Boćkowski, I. Grzegory, J. Szczytko, and A. Twardowski. The nature of Cr center in GaN: Magnetic anisotropy of GaN:Cr single crystals. *Journal of Applied Physics*, 112(11):113914, 2012.
- [13] D. Banerjee, R. Adari, S. Sankaranarayan, A. Kumar, S. Ganguly, R. W. Aldhaheri, M. A. Hussain, A. S. Balamesh, and D. Saha. Electrical spin injection using GaCrN in a GaN based spin light emitting diode. *Applied Physics Letters*, 103(24):242408, 2013.
- [14] Saroj P. Dash, Sandeep Sharma, Ram S. Patel, de Jong, Michel P, and Ron Jansen. Electrical creation of spin polarization in silicon at room temperature. *Nature*, 462(7272):491–494, 2009.
- [15] H. Zhu, M. Ramsteiner, H. Kostial, M. Wassermeier, H.-P. Schönherr, and K. Ploog. Room-Temperature Spin Injection from Fe into GaAs. *Physical Review Letters*, 87(1), 2001.
- [16] Shafat Jahangir, Fatih Doğan, Hyun Kum, Aurelien Manchon, and Pallab Bhattacharya. Spin diffusion in bulk GaN measured with MnAs spin injector. *Physical Review B*, 86(3), 2012.
- [17] Hadis Morkoç. *Handbook of nitride semiconductors and devices*. Wiley-VCH, Weinheim, 2008. ISBN 978-3-527-40837-5.
- [18] A. Watanabe, T. Takeuchi, K. Hirosawa, H. Amano, K. Hiramatsu, and I. Akasaki. The growth of single crystalline GaN on a Si substrate using AlN as an intermediate layer. *Journal of Crystal Growth*, 128(1-4):391–396, 1993.
- [19] Eric Feltin, B. Beaumont, M. Laügt, P. de Mierry, P. Vennéguès, H. Lahrèche, M. Leroux, and P. Gibart. Stress control in GaN grown on silicon (111) by metalorganic vapor phase epitaxy. *Applied Physics Letters*, 79(20):3230, 2001.
- [20] Claudio R. Miskys, Michael K. Kelly, Oliver Ambacher, and Martin Stutzmann. Freestanding GaN-substrates and devices. *physica status solidi (c)*, 0(6):1627–1650, 2003.



- 
- [21] J. Karpiński and S. Porowski. High pressure thermodynamics of GaN. *Journal of Crystal Growth*, 66(1):11–20, 1984.
- [22] M. A. Moram and M. E. Vickers. X-ray diffraction of III-nitrides. *Reports on Progress in Physics*, 72(3):036502, 2009.
- [23] B. Heying, X. H. Wu, S. Keller, Y. Li, D. Kapolnek, B. P. Keller, S. P. DenBaars, and J. S. Speck. Role of threading dislocation structure on the x-ray diffraction peak widths in epitaxial GaN films. *Applied Physics Letters*, 68(5):643–645, 1996.
- [24] Subhashis Gangopadhyay, Thomas Schmidt, Carsten Kruse, Stephan Figge, Detlef Hommel, and Jens Falta. Surface oxidation of GaN(0001): Nitrogen plasma-assisted cleaning for ultrahigh vacuum applications. *Journal of Vacuum Science & Technology A: Vacuum, Surfaces, and Films*, 32(5):051401, 2014.
- [25] Tosja Zywietz, Jörg Neugebauer, and Matthias Scheffler. Adatom diffusion at GaN (0001) and (000 $\bar{1}$ ) surfaces. *Applied Physics Letters*, 73(4):487, 1998.
- [26] John Northrup, J. Neugebauer, R. Feenstra, and A. Smith. Structure of GaN(0001): The laterally contracted Ga bilayer model. *Physical Review B*, 61(15):9932–9935, 2000.
- [27] Daniel Broxtermann. *Towards high electron mobility in GaN(0001) based InGaN and AlGaIn heterostructures*. PhD thesis, Georg-August Universität, Göttingen, 2011.
- [28] Daniel Broxtermann, M. Sivilis, J. Malindretos, and A. Rizzi. MBE growth of high electron mobility 2DEGs in AlGaIn/GaN heterostructures controlled by RHEED. *AIP Advances*, 2(1):012108, 2012.
- [29] C. T. Foxon, R. P. Campion, V. A. Grant, S. V. Novikov, J. J. Harris, R. Thomson, C. Taylor, and D. Barlett. Use of band-gap thermometry to investigate the growth of GaN on sapphire and GaAs. *Journal of Crystal Growth*, 301-302:482–485, 2007.
- [30] G. Koblmüller, F. Reurings, F. Tuomisto, and J. S. Speck. Influence of Ga/N ratio on morphology, vacancies, and electrical transport in GaN grown by molecular beam epitaxy at high temperature. *Applied Physics Letters*, 97(19):191915, 2010.
- [31] G. Koblmüller, F. Wu, T. Mates, J. S. Speck, S. Fernández-Garrido, and E. Calleja. High electron mobility GaN grown under N-rich con-

- ditions by plasma-assisted molecular beam epitaxy. *Applied Physics Letters*, 91(22):221905, 2007.
- [32] M. Julliere. Tunneling between ferromagnetic films. *Physics Letters A*, 54(3):225–226, 1975.
- [33] Yu A Bychkov and E I Rashba. Oscillatory effects and the magnetic susceptibility of carriers in inversion layers. *Journal of Physics C: Solid State Physics*, 17(33):6039, 1984.
- [34] Hyun Cheol Koo, Jae Hyun Kwon, Jonghwa Eom, Joonyeon Chang, Suk Hee Han, and Mark Johnson. Control of spin precession in a spin-injected field effect transistor. *Science (New York, N.Y.)*, 325(5947):1515–1518, 2009.
- [35] Z. Yu and M. Flatté. Spin diffusion and injection in semiconductor structures: Electric field effects. *Physical Review B*, 66(23), 2002.
- [36] E. Y. Tsymlal and Igor Žutić. *Handbook of spin transport and magnetism*. CRC Press, Boca Raton, FL, 2012. ISBN 1439803781.
- [37] R. J. Soulen Jr. Measuring the Spin Polarization of a Metal with a Superconducting Point Contact. *Science*, 282(5386):85–88, 1998.
- [38] C. Adelman, X. Lou, J. Strand, C. Palmstrøm, and P. Crowell. Spin injection and relaxation in ferromagnet-semiconductor heterostructures. *Physical Review B*, 71(12), 2005.
- [39] G. Schmidt, D. Ferrand, L. Molenkamp, A. Filip, and B. van Wees. Fundamental obstacle for electrical spin injection from a ferromagnetic metal into a diffusive semiconductor. *Physical Review B*, 62(8):R4790–R4793, 2000.
- [40] Tomoyuki Sasaki, Tohru Oikawa, Toshio Suzuki, Masashi Shiraishi, Yoshishige Suzuki, and Katsumichi Tagami. Electrical Spin Injection into Silicon Using MgO Tunnel Barrier. *Applied Physics Express*, 2:053003, 2009.
- [41] V. F. Motsnyi, J. de Boeck, J. Das, W. van Roy, G. Borghs, E. Goovaerts, and V. I. Safarov. Electrical spin injection in a ferromagnet/tunnel barrier/semiconductor heterostructure. *Applied Physics Letters*, 81(2):265–267, 2002.
- [42] Xiaohua Lou, Christoph Adelman, Scott A. Crooker, Eric S. Garlid, Jianjie Zhang, K. S. Madhukar Reddy, Soren D. Flexner, Chris J. Palmstrøm, and Paul A. Crowell. Electrical detection of spin transport

- in lateral ferromagnet–semiconductor devices. *Nature Physics*, 3(3): 197–202, 2007.
- [43] O. M. J. van 't Erve, A. T. Hanbicki, M. Holub, C. H. Li, C. Awo-Affouda, P. E. Thompson, and B. T. Jonker. Electrical injection and detection of spin-polarized carriers in silicon in a lateral transport geometry. *Applied Physics Letters*, 91(21):212109, 2007.
- [44] André Dankert, Ravi S. Dulal, and Saroj P. Dash. Efficient Spin Injection into Silicon and the Role of the Schottky Barrier. *Scientific Reports*, 3, 2013.
- [45] B. Jonker, Y. Park, B. Bennett, H. Cheong, G. Kioseoglou, and A. Petrou. Robust electrical spin injection into a semiconductor heterostructure. *Physical Review B*, 62(12):8180–8183, 2000.
- [46] M. Ramsteiner, O. Brandt, T. Flissikowski, H. Grahn, M. Hashimoto, J. Herfort, and H. Kostial.  $\text{Co}_2\text{FeSi}/\text{GaAs}/(\text{Al,Ga})\text{As}$  spin light-emitting diodes: Competition between spin injection and ultrafast spin alignment. *Physical Review B*, 78(12), 2008.
- [47] Moon-Ho Ham, Sukho Yoon, Yongjo Park, Lifeng Bian, Manfred Ramsteiner, and Jae-Min Myoung. Electrical spin injection from room-temperature ferromagnetic (Ga, Mn)N in nitride-based spin-polarized light-emitting diodes. *Journal of Physics: Condensed Matter*, 18(32): 7703–7708, 2006.
- [48] Biqin Huang, Douwe J. Monsma, and Ian Appelbaum. Coherent Spin Transport through a 350 Micron Thick Silicon Wafer. *Physical Review Letters*, 99(17), 2007.
- [49] Oihana Txoperena, Marco Gobbi, Amilcar Bedoya-Pinto, Federico Golmar, Xiangnan Sun, Luis E. Hueso, and Fèlix Casanova. How reliable are Hanle measurements in metals in a three-terminal geometry? *Applied Physics Letters*, 102(19):192406, 2013.
- [50] Tetsuya Uemura, Kenji Kondo, Jun Fujisawa, Ken-ichi Matsuda, and Masafumi Yamamoto. Critical effect of spin-dependent transport in a tunnel barrier on enhanced Hanle-type signals observed in three-terminal geometry. *Applied Physics Letters*, 101(13):132411, 2012.
- [51] R. L. deZafra. Measurement of Atomic Lifetimes by the Hanle Effect. *American Journal of Physics*, 35(7):573, 1967.
- [52] Igor Žutić and S. Das Sarma. Spintronics: Fundamentals and applications. *Reviews of Modern Physics*, 76(2):323–410, 2004.

- 
- [53] Hartmut Haug and S. W. Koch. *Quantum theory of the optical and electronic properties of semiconductors*. World Scientific, Singapore, 3 edition, 1994. ISBN 981-02-2002-2.
- [54] Marius Grundmann. *The physics of semiconductors: An introduction including nanophysics and applications*. Graduate texts in physics. Springer, Berlin and Heidelberg, 2 edition, 2010. ISBN 978-3-642-13884-3.
- [55] Shun Lien. Chuang. *Physics of photonic devices*. Wiley series in pure and applied optics. John Wiley & Sons, Hoboken, N.J., 2nd ed. edition, 2009. ISBN 978-0-470-29319-5.
- [56] J. H. Buß, J. Rudolph, F. Natali, F. Semond, and D. Hägele. Temperature dependence of electron spin relaxation in bulk GaN. *Physical Review B*, 81(15), 2010.
- [57] I. A. Buyanova, M. Izadifard, W. M. Chen, J. Kim, F. Ren, G. Thaler, C. R. Abernathy, S. J. Pearton, C.-C. Pan, G.-T. Chen, J.-I. Chyi, and J. M. Zavada. On the origin of spin loss in GaMnN/InGaN light-emitting diodes. *Applied Physics Letters*, 84(14):2599–2601, 2004.
- [58] C. Adelman, J. L. Hilton, B. D. Schultz, S. McKernan, C. J. Palmstrøm, X. Lou, H.-S. Chiang, and P. A. Crowell. Spin injection from perpendicular magnetized ferromagnetic - MnGa into (Al,Ga)As heterostructures. *Applied Physics Letters*, 89(11):112511, 2006.
- [59] Erdong Lu, David Ingram, Arthur Smith, J. Knepper, and F. Yang. Reconstruction Control of Magnetic Properties during Epitaxial Growth of Ferromagnetic  $\text{Mn}_{3-\delta}\text{Ga}$  on Wurtzite GaN(0001). *Physical Review Letters*, 97(14), 2006.
- [60] A. Bedoya-Pinto, C. Zube, J. Malindretos, A. Urban, and A. Rizzi. Epitaxial-  $\text{Mn}_x\text{Ga}_{1-x}$  layers on GaN(0001): Structural, magnetic, and electrical transport properties. *Physical Review B*, 84(10), 2011.
- [61] W. van Roy, H. Akinaga, S. Miyanishi, K. Tanaka, and L. H. Kuo. Epitaxial MnGa/(Mn,Ga,As)/MnGa trilayers: Growth and magnetic properties. *Applied Physics Letters*, 69(5):711–713, 1996.
- [62] M. Tanaka, J. P. Harbison, T. Sands, B. Philips, T. L. Cheeks, J. De-Boeck, L. T. Florez, and V. G. Keramidas. Epitaxial ferromagnetic MnGa/NiGa multilayers on GaAs. *Journal of Magnetism and Magnetic Materials*, 126(1-3):313–315, 1993.

- 
- [63] Feng Wu, Shigemi Mizukami, Daisuke Watanabe, Hiroshi Naganuma, Mikihiro Oogane, Yasuo Ando, and Terunobu Miyazaki. Epitaxial  $\text{Mn}_{2.5}\text{Ga}$  thin films with giant perpendicular magnetic anisotropy for spintronic devices. *Applied Physics Letters*, 94(12):–, 2009.
- [64] Kangkang Wang, Erdong Lu, Jacob W. Knepper, Fengyuan Yang, and Arthur R. Smith. Structural controlled magnetic anisotropy in Heusler  $\text{L10-MnGa}$  epitaxial thin films. *Applied Physics Letters*, 98(16):–, 2011.
- [65] Wuwei Feng, Duong van Thiet, Dang Duc Dung, Yooleemi Shin, and Sunglae Cho. Substrate-modified ferrimagnetism in  $\text{MnGa}$  films. *Journal of Applied Physics*, 108(11):–, 2010.
- [66] H.P.J Wijn, editor. *Alloys and Compounds of d-Elements with Main Group Elements. Part 1*. Landolt-Börnstein - Group III Condensed Matter. Springer-Verlag, Berlin/Heidelberg, 1987. ISBN 3-540-17094-4.
- [67] Hiroshi Niida, Tomiei Hori, Hideya Onodera, Yasuo Yamaguchi, and Yasuaki Nakagawa. Magnetization and coercivity of  $\text{Mn}_{3-d}\text{Ga}$  alloys with a D022-type structure. *Journal of Applied Physics*, 79(8):5946–5948, 1996.
- [68] Jürgen Winterlik, Benjamin Balke, Gerhard H. Fecher, Claudia Felser, Alves, Maria C. M., Fabiano Bernardi, and Jonder Morais. Structural, electronic, and magnetic properties of tetragonal  $\text{Mn}_{3-x}\text{Ga}$ : Experiments and first-principles calculations. *Physical Review B*, 77(5), 2008.
- [69] Benjamin Balke, Gerhard H. Fecher, Jürgen Winterlik, and Claudia Felser.  $\text{Mn}_3\text{Ga}$ , a compensated ferrimagnet with high Curie temperature and low magnetic moment for spin torque transfer applications. *Applied Physics Letters*, 90(15):152504, 2007.
- [70] H. Kurt, K. Rode, M. Venkatesan, P. Stamenov, and Coey, J. M. D. High spin polarization in epitaxial films of ferrimagnetic  $\text{Mn}_3\text{Ga}$ . *Phys. Rev. B*, 83(2):020405, 2011.
- [71] Coey, J M D. New permanent magnets; manganese compounds. *Journal of physics. Condensed matter : an Institute of Physics journal*, 26(6):064211, 2014.
- [72] Tom A. Bither and William H. Cloud. Magnetic Tetragonal  $\delta$ -Phase in the  $\text{Mn}[\text{Single Bond}]\text{Ga}$  Binary. *Journal of Applied Physics*, 36(4):1501, 1965.

- 
- [73] Kannan M. Krishnan. Ferromagnetic  $\delta$ -Mn<sub>1-x</sub>Ga<sub>x</sub> thin films with perpendicular anisotropy. *Applied Physics Letters*, 61(19):2365, 1992.
- [74] W. van Roy, H. Akinaga, and S. Miyanishi. Interlayer coupling and magnetoresistance of MnGa-based trilayers with semiconducting, antiferromagnetic, and ferrimagnetic spacer layers. *Physical Review B*, 63(18), 2001.
- [75] Akimasa Sakuma. Electronic structures and magnetism of CuAu-type MnNi and MnGa. *Journal of Magnetism and Magnetic Materials*, 187(1):105–112, 1998.
- [76] Zongxian Yang, Jun Li, Ding-sheng Wang, Kaiming Zhang, and Xide Xie. Electronic structure and magnetic properties of  $\delta$ -MnGa. *Journal of Magnetism and Magnetic Materials*, 182(3):369–374, 1998.
- [77] Peter Schattschneider. *Fundamentals of inelastic electron scattering*. Springer-Verlag, Wien and New York, 1986. ISBN 3-211-81937-1.
- [78] V. M. Bermudez. Study of oxygen chemisorption on the GaN(0001)–(1×1) surface. *Journal of Applied Physics*, 80(2):1190–1200, 1996.
- [79] J. I. Hwang, Y. Osafune, M. Kobayashi, K. Ebata, Y. Ooki, Y. Ishida, A. Fujimori, Y. Takeda, T. Okane, Y. Saitoh, K. Kobayashi, and A. Tanaka. Depth profile high-energy spectroscopic study of Mn-doped GaN prepared by thermal diffusion. *Journal of Applied Physics*, 101(10):103709, 2007.
- [80] Ferdinand Braun. Ueber die Stromleitung durch Schwefelmetalle. *Annalen der Physik und Chemie*, 229(12):556–563, 1875.
- [81] W. Schottky. Zur Halbleiterttheorie der Sperrschicht- und Spitzengleichrichter. *Zeitschrift für Physik*, 113(5-6):367–414, 1939.
- [82] S.M. Sze. *Physics of semiconductor Devices*. John Wiley & Sons, 1981.
- [83] Hans Lüth. *Solid Surfaces, Interfaces and Thin Films*. Springer Berlin Heidelberg, Berlin and Heidelberg, 2010. ISBN 978-3-642-13591-0.
- [84] Christian Zube. MnGa/ GaN Heterostrukturen in Hinblick auf Spininjektion. Diploma thesis, 2010.
- [85] W. Mönch. *In Festkörperprobleme*. Vieweg, Braunschweig, vol. 26 edition, 1986.
- [86] John Bardeen. Surface States and Rectification at a Metal Semiconductor Contact. *Physical Review*, 71(10):717–727, 1947.



- 
- [87] Brianna S. Eller, Jialing Yang, and Robert J. Nemanich. Electronic surface and dielectric interface states on GaN and AlGaN. *Journal of Vacuum Science & Technology A: Vacuum, Surfaces, and Films*, 31(5):050807, 2013.
- [88] C.B Stagarescu K.E Smith D. Doppalapudi R. Singh S.S. Dhesi and T.D Moustakas. Surface and bulk electronic structure of thin-film wurtzite GaN. *Physical Review B*, 56(16), 1997.
- [89] Chris G. van de Walle and David Segev. Microscopic origins of surface states on nitride surfaces. *Journal of Applied Physics*, 101(8):081704, 2007.
- [90] M. Himmerlich, L. Lymperakis, R. Gutt, P. Lorenz, J. Neugebauer, and S. Krischok. GaN(0001) surface states: Experimental and theoretical fingerprints to identify surface reconstructions. *Physical Review B*, 88(12), 2013.
- [91] Sang-Jun Cho, Seydi Doğan, Shahriar Sabuktagin, Michael A. Reshchikov, Daniel K. Johnstone, and Hadis Morkoç. Surface band bending in as-grown and plasma-treated n-type GaN films using surface potential electric force microscopy. *Applied Physics Letters*, 84(16):3070, 2004.
- [92] Ho Won Jang, Jung-Hee Lee, and Jong-Lam Lee. Characterization of band bendings on Ga-face and N-face GaN films grown by metalorganic chemical-vapor deposition. *Applied Physics Letters*, 80(21):3955, 2002.
- [93] Volker Heine. Theory of Surface States. *Physical Review*, 138(6A):A1689–A1696, 1965.
- [94] Monika Mattern-Klosson and H. Lüth. The Schottky barrier of Sn on GaAs(110). *Surface Science*, 162(1-3):610–616, 1985.
- [95] D. O. Demchenko and Amy Y. Liu. Influence of interface structure on electronic properties and Schottky barriers in Fe/ GaAs magnetic junctions. *Physical Review B*, 73(11):115332, 2006.
- [96] H. Zhang, E. J. Miller, and E. T. Yu. Analysis of leakage current mechanisms in Schottky contacts to GaN and  $\text{Al}_{0.25}\text{Ga}_{0.75}\text{N}$  / GaN grown by molecular-beam epitaxy. *Journal of Applied Physics*, 99(2):023703, 2006.
- [97] Gregor Wentzel. Eine Verallgemeinerung der Quantenbedingungen für die Zwecke der Wellenmechanik. *Zeitschrift für Physik*, 38(6-7):518–529, 1926.

- 
- [98] David Disterheft. Experiments on spin injection in MnGa/GaN-heterostructures: Master thesis. Master thesis, July 2014.
- [99] J. M. Rowell. Tunneling Anomalies-Experiment. In Elias Burstein and Stig Lundqvist, editors, *Tunneling Phenomena in Solids*, pages 385–404. Springer US, Boston, MA, 1969. ISBN 978-1-4684-1754-8.
- [100] Eric Scott Garlid. *Electrical detection of the spin Hall effect in ferromagnet-semiconductor heterostructures*. PhD thesis, UNIVERSITY OF MINNESOTA, 2010.
- [101] Lars Watschke. Optische Experimente zur Spininjektion von Mangan-Gallium in Gallium-Nitrid. Diploma thesis, Februar 2015.
- [102] M. Ramsteiner, H. Hao, A. Kawaharazuka, H. Zhu, M. Kästner, R. Hey, L. Däweritz, H. Grahn, and K. Ploog. Electrical spin injection from ferromagnetic MnAs metal layers into GaAs. *Physical Review B*, 66(8), 2002.
- [103] M. J. Snelling, E. Blackwood, C. J. McDonagh, R. T. Harley, and Foxon, C. T. B. Exciton, heavy-hole, and electron g factors in type-i gaas/alxga1-x as quantum wells. *Physical Review B*, 45(7):3922–3925, 1992. doi: 10.1103/PhysRevB.45.3922.
- [104] Kyu-Seok Lee and El-Hang Lee. Optical determination of the heavy-hole effective mass of (in, ga) as/gaas quantum wells. *ETRI journal*, 17(4):13–24, 1996.
- [105] L. Viña, L. Muñoz, E. Pérez, J. Fernández-Rossier, C. Tejedor, and K. Ploog. Spin splitting in a polarized quasi-two-dimensional exciton gas. *Phys. Rev. B*, 54:R8317–R8320, Sep 1996.
- [106] Yang, S. -R. Eric and L. J. Sham. Theory of magnetoexcitons in quantum wells. *Physical Review Letters*, 58(24):2598–2601, 1987. doi: 10.1103/PhysRevLett.58.2598.
- [107] Bauer, Gerrit E. W. and Tsuneya Ando. Theory of magnetoexcitons in quantum wells. *Physical Review B*, 37(6):3130–3133, 1988. doi: 10.1103/PhysRevB.37.3130.
- [108] W. Ossau, B. JÄdkel, E. Bangert, G. Landwehr, and G. Weimann. Magneto-optical determination of the exciton binding energy in gaas quantum wells. *Surface Science*, 174(1):188 – 193, 1986. ISSN 0039-6028.
- [109] Yu. E. Lozovik, I. V. Ovchinnikov, S. Yu. Volkov, L. V. Butov, and



- D. S. Chemla. Quasi-two-dimensional excitons in finite magnetic fields. *Phys. Rev. B*, 65:235304, May 2002.
- [110] Pil Hun Song and K. W. Kim. Spin relaxation of conduction electrons in bulk III-V semiconductors. *Phys. Rev. B*, 66(3):035207, 2002.
- [111] R. I. Dzhioev, K. V. Kavokin, V. L. Korenev, M. V. Lazarev, B. Ya Meltser, M. N. Stepanova, B. P. Zakharchenya, D. Gammon, and D. S. Katzer. Low-temperature spin relaxation in n -type GaAs. *Physical Review B*, 66(24), 2002.
- [112] Jörg Neugebauer and Chris G. van de Walle. Gallium vacancies and the yellow luminescence in GaN. *Applied Physics Letters*, 69(4):503, 1996.
- [113] Hisashi Masui, Natalie N. Fellows, Shuji Nakamura, and Steven P. DenBaars. Optical polarization characteristics of light emission from sidewalls of primary-color light-emitting diodes. *Semiconductor Science and Technology*, 23(7):072001, 2008.
- [114] W. Bardyszewski and S. P. Łepkowski. Nonlinear zeeman splitting of magnetoexcitons in *c*-plane wurtzite gan-based quantum wells. *Phys. Rev. B*, 90:075302, Aug 2014.
- [115] Michael Bass. *Handbook of optics*. McGraw-Hill, New York, 2nd ed. edition, 1995-©2001. ISBN 0-07-047974-7.
- [116] Yeong Hwan Ko and Jae Su Yu. Highly transparent sapphire micro-grating structures with large diffuse light scattering. *Optics express*, 19(16):15574–15583, 2011.
- [117] D. Zhuang and J. H. Edgar. Wet etching of GaN, AlN, and SiC: a review. *Materials Science and Engineering: R: Reports*, 48(1):1–46, 2005.
- [118] Steve Pearton, W. Lim, Fan Ren, and David Norton. Wet Chemical Etching of Wide Bandgap Semiconductors- GaN, ZnO and SiC. In *211th ECS Meeting*, pages 501–512, May 6-May 10, 2007.
- [119] J. Li, Z. Y. Wang, A. Tan, P.-A. Glans, E. Arenholz, C. Hwang, J. Shi, and Z. Q. Qiu. Magnetic dead layer at the interface between a Co film and the topological insulator Bi<sub>2</sub> Se<sub>3</sub>. *Physical Review B*, 86(5), 2012.
- [120] J. F. Ankner, C. F. Majkrzak, and H. Homma. Magnetic dead layer in Fe/Si multilayer: Profile refinement of polarized neutron reflectivity data. *Journal of Applied Physics*, 73(10):6436, 1993.

- 
- [121] J. S. White, M. Bator, Y. Hu, H. Luetkens, J. Stahn, S. Capelli, S. Das, M. Döbeli, Th. Lippert, V. K. Malik, J. Martynczuk, A. Wokaun, M. Kenzelmann, Ch. Niedermayer, and C. W. Schneider. Strain-Induced Ferromagnetism in Antiferromagnetic LuMnO<sub>3</sub> Thin Films. *Phys. Rev. Lett.*, 111(3):037201, 2013.
- [122] S. A. Chambers, F. Xu, H. W. Chen, I. M. Vitomirov, S. B. Anderson, and J. H. Weaver. Simultaneous epitaxy and substrate out-diffusion at a metal-semiconductor interface: Fe/GaAs(001)-c (82). *Phys. Rev. B*, 34(10):6605–6611, 1986.
- [123] T. Ashraf, C. Gusenbauer, J. Stangl, G. Hesser, M. Wegscheider, and R. Koch. Stress and interdiffusion during molecular beam epitaxy of Fe on As-rich GaAs(001). *Journal of physics. Condensed matter : an Institute of Physics journal*, 23(4):042001, 2011.
- [124] B. D. Schultz, C. Adelman, X. Y. Dong, S. McKernan, and C. J. Palmström. Phase formation in the thin film Fe/GaAs system. *Applied Physics Letters*, 92(9):091914, 2008.
- [125] B. D. Schultz, N. Marom, D. Naveh, X. Lou, C. Adelman, J. Strand, P. A. Crowell, L. Kronik, and C. J. Palmstrøm. Spin injection across the Fe/GaAs interface: Role of interfacial ordering. *Phys. Rev. B*, 80:201309, Nov 2009.
- [126] Q. O. Hu, E. S. Garlid, P. A. Crowell, and C. J. Palmstrøm. Spin accumulation near Fe/GaAs (001) interfaces: The role of semiconductor band structure. *Physical Review B*, 84(8), 2011.
- [127] R. M. Stroud, A. T. Hanbicki, Y. D. Park, G. Kioseoglou, A. G. Petukhov, B. T. Jonker, G. Itskos, and A. Petrou. Reduction of Spin Injection Efficiency by Interface Defect Spin Scattering in ZnMnSe/AlGaAs–GaAs Spin-Polarized Light-Emitting Diodes. *Physical Review Letters*, 89(16), 2002.
- [128] Christelle Brimont, Mathieu Gallart, Olivier Crégut, Bernd Hönerlage, and Pierre Gilliot. Experimental investigation of excitonic spin relaxation dynamics in GaN. *Physical Review B*, 77(12), 2008.
- [129] Carla Ivana Oppo. Patterned mask for Selective Area Growth by EBL, <http://www.reinraum.physik.uni-goettingen.de/wikka/patterningmasksforsag>.

Christian Zube  
Ludwig-Mohr-Str. 6  
34119 Kassel  
christian.zube@gmx.net

# Curriculum Vitae

- **Personal data**

Date of birth: June 24th 1985  
Place of birth: Kassel, Germany  
Nationality: German

- **Promotion**

10.2010-11.2015 **PhD student** at the Georg-August University of Göttingen,  
IV. Physikalisches Institut/ semiconductor institute,  
Dissertation: 'Spin injection in MnGa/ GaN heterostructures'

- **Diploma**

10.2005-09.2010 **Study of Physics** with a minor in computer science  
at the Georg-August University of Göttingen,  
Thesis: 'MnGa/ GaN heterostructures in terms of spin injection'

- **Education**

1996 - 2005 Albert-Schweitzer Schule Kassel,  
graduation: higher education entrance qualification  
(allgemeine Hochschulreife)  
1992-1996 Königstorschule Kassel, primary school

